The nonlinear elasticity of cellular bodies under large deformations

Khulud Abdulghaffar Aziz Alayyash

A thesis presented for the degree of
Doctor of Philosophy

Applied and Computational Mathematics Group
Cardiff School of Mathematics
Cardiff University
Wales, UK

2017

The nonlinear elasticity of cellular bodies under large deformations

Khulud Abdulghaffar Aziz Alayyash

Submitted for the degree of Doctor of Philosophy
2017

Abstract

Many natural and man-made cellular bodies are light-weight, shock-absorbing, multi-functional materials, capable of undertaking large elastic deformations. These properties are due to a complex system of local deformations which can lead to changes in the material properties as the deformation progresses, but their study is non-trivial since the corresponding stresses are non-trivial functions of volume fraction, micro-geometry, and material properties of the components. For cellular bodies of hyperelastic material, several main factors determine the magnitude of the stress level, including the cell geometry, the cell wall thickness, and the presence of cell inclusions. In this thesis, two nonlinear elastic parameters are identified, namely a *nonlinear elastic modulus* and a *nonlinear Poisson's ratio*, which are defined in terms of the large stresses and strains in the elastic cell walls, and their utility in estimating how different competing factors may contribute to the complex mechanical behaviour of cellular structures is investigated. For the numerical analysis, finite element simulations of periodic, honeycomb-like structures with a small number of square, diamond, or hexagonal cells made from a nonlinear hyperelastic material are presented. This study offers important insight into the fundamental behaviour of cellular structures of nonlinear elastic material under large strains, and contributes to illuminate key mechanical effects that are not visible under small strains.

Declaration

This work has not been submitted in substance for any other degree or award at this or any other university or place of learning, nor is being submitted concurrently in candidature for any degree or other award.

Signed ..... (candidate) Date .....

Statement 1

This thesis is being submitted in partial fulfilment of the requirements for the degree of PhD of Mathematics.

Signed ..... (candidate) Date .....

Statement 2

This thesis is the result of my own independent work/investigation, except where otherwise stated, and the thesis has not been edited by a third party beyond what is permitted by Cardiff University's Policy on the Use of Third Party Editors by Research Degree Students. Other sources are acknowledged by explicit references. The views expressed are my own.

Signed ..... (candidate) Date .....

Statement 3

I hereby give consent for my thesis, if accepted, to be available online in the University's Open Access repository and for inter-library loan, and for the title and summary to be made available to outside organisations.

Signed ..... (candidate) Date .....

Statement 4: Previously Approved Bar On Access

I hereby give consent for my thesis, if accepted, to be available online in the University's Open Access repository and for inter-library loans after expiry of a bar on access previously approved by the Academic Standards and Quality Committee.

Signed ..... (candidate) Date .....

Acknowledgements

It is a great pleasure to express my gratitude to those special people whose support I could count on receiving while I was preparing this thesis, especially to my family and to my supervisor, Dr Angela Mihai. My work for this thesis was generously funded by a scholarship from the Saudi Arabia Government.

Contents

List of Figures

List of Tables

Chapter 1

Introduction

1.1 Background and motivation

Solid cellular structures are two or three dimensional bodies divided into cells, the walls of which are made of a solid material capable of undertaking large deformations without plastic failure or fracture. Due to their exceptional mechanical efficiency, they are widespread in nature and industry, from marine sponges and plant stems, which have been around for million of years, to biomedical tissue scaffolds and synthetic foams, which are under continuous research and development [3, 7, 21, 49, 77, 115, 135] (figure 1.1.1). Galileo Galilei (1564-1642) first suggested that bones must contain voids to account for their high strength to weight ratio, and also observed that bones of a large animal need to be thicker in proportion to their size than those of smaller animals. Robert Hooke (1635-1703) introduced the word "cell" to describe the microscopic structure of cork, as well as the classical law *ut tensio sic vis* (as the extension, so the force) [58, 125].

In natural structures, the mechanical support system is usually formed through a combination of increase in the cell number or size and sustained sclerification of the cell walls. Dicotyledon stems (e.g.,

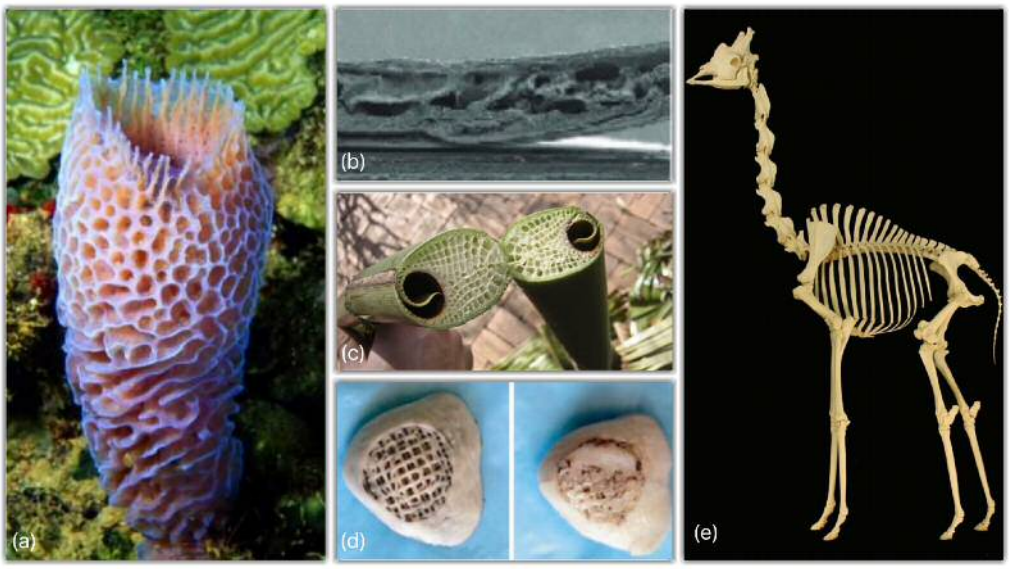

Figure 1.1.1: Examples of natural and man-made cellular structures: (a) marine sponge; (b) skull bone; (c) palm shoots; (d) stretchy scaffold for joints regrowth; (e) giraffe skeleton.

magnolia, maple, oak, rose, sycamore, willow) increase their diameter primarily by cell division which ultimately form the characteristic annual rings. Monocotyledon stems (e.g., bamboo, corn, lily, orchid, palm) prevent mechanical failure through a combination of initiation of growth with a stem that is sufficiently wide for future supply and support demands, and an increase in the stem diameter and strength by cell wall expansion and lignification, especially toward the stem periphery and base. Although some monocot plants attain tree stature comparable with arborescent dicotyledons and conifers (e.g., palm trees with maximum heights of 20-40 meters), their stems are relatively slender [109]. By contrast, tall dicot trees have bigger stem diameters relative to their height than small trees, even though the wood density representing the relative quantity of the cell wall in a given volume of wood tissue does not vary significantly among wood species [44]. Bone tissue is another example of natural cellular solids, and the bones of large animals are generally thicker in proportion to

their size than those of small scale animals, while neck vertebrae have lower density than limb bones. In [103], it was shown that apposition and resorption of bony material are controlled by the magnitude of the stresses, and that bones under stress become denser at the point of stress. This explains in part why, in the long neck of the giraffe (*Giraffa camelopardalis*) which contains the same number of vertabræas that of the buffalo (*Syncerus caffer*) for example, the cervical vertebrædecrease in mass with cranial distance, so that, one the one hand, the mass of the head and neck is supported mainly at the base, and on the other hand, the cranial extremity is lighter and easier to manoeuvre than in buffaloes [130]. In Sauropod dinosaurs, necks were found six times longer than in giraffes, and cervicals were estimated as consisting of 60% air due to an *air-sac system* similar to those found in extant birds, which made them both light and pneumatic [124]. In living structures, there are many physiological and ecological factors which influence their complex mechanical properties, which change over time [8, 26, 49, 58, 65, 95]. From the mechanical point of view, many natural and man-made cellular bodies are light-weight, shock-absorbing, multi-functional materials, capable of undertaking large elastic deformations. These properties are due to a complex system of local deformations which can lead to changes in the material properties as the deformation progresses, but their study is non-trivial since the corresponding stresses are non-trivial functions of volume fraction, micro-geometry, and material properties of the components (figure 1.1.2) [79, 80, 84, 85, 87–89].

For periodic cellular structures with uniform cell size, wall thickness, and shape, if the size of the cell is small compared to the size

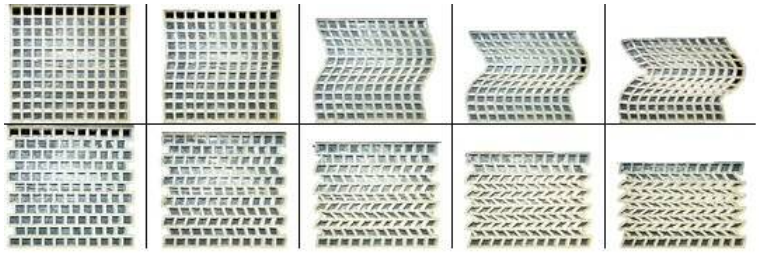

Figure 1.1.2: Geometry-dependent deformations of cellular structures with stacked (top) and staggered (bottom) cells of neo-Hookean material under vertical compression.

of a sample of the material, then effective theories can be derived from a microscopic description of the problem via a "homogenisation" or "averaging" technique. In this case, denoting by ϵ the ratio between the size of the cell and the size of the sample, an asymptotic analysis, as ϵ goes to zero, can be employed. Although the word "homogenisation" was first used by Babuška [4] who pioneered numerical approaches for homogenisation problems, the physical idea of averaging over a heterogeneous medium was known since Maxwell [75] and Poisson [105]. To date, many results, approximation formulas, and estimates have been obtained in this area. However, while the majority of the existing homogenisation results are concerned with linear elastic periodic media, for which a rigorous mathematical approach has been established [2,22,62,99], the study of nonlinear elastic composites presents considerable additional difficulties, both at the microscopic and macroscopic levels [47, 127]. There is an increasing interest in the nonlinear responses of periodic cellular structures capable of finite (large) strain deformation, where material nonlinearities are expected to play significant roles. For example, in [72], homogenisation techniques are used to determine the macroscopic behaviour of porous elastomers, as well as the associated evolution of their microstructure

and the possible development of instabilities when finite deformations occur; in [78], multiscale stability aspects of the superelastic behavior of hexagonal honeycombs under in-plane compression are analysed, and an in-depth parameter study is performed on the influence of different material laws on the finite strain deformation of honeycombs with perfect and imperfect geometries, while finite element simulations are shown to capture the behavior observed in the experiments; in [119], homogenisation estimates for the finite strain effective response of dielectric elastomer composites subject to electromechanical loading conditions are obtained from available estimates for the purely mechanical response combined with a partial decoupling approximation strategy. Homogenisation is not restricted to periodic structures, but there are many important remaining questions about the influence of the properties and local behaviour of the material components in cellular composite materials [31, 43, 109]. To answer some of these question, there has been an increasing effort in combining physical experiments and computer simulation [100–102,116,120,121,132]. While particular structures seen in experiments can be mimicked computationally by various finite element implementations, in many cellular structures, local deformations can lead to changes in the material properties as the deformation progresses. When the cell walls are made from a linear elastic material, it was noted that the mechanism which dominates the deformation of cellular structures is that of bending of the cell walls [13, 27, 28, 40, 49, 76]. In nonlinear elastic materials, finite strain deformations are responsible for new mechanical effects [10, 42, 69, 82, 83, 86, 107, 111].

1.2 Scope of this thesis

The goal of this thesis is to analyse and compute the deformation of cellular bodies within the framework of finite strain elasticity, which in principle can provide a complete description of elastic responses in the solid cell walls under loading, and provide new insight into the rich mechanical responses of these structures by showing some interesting behaviours which are not captured in the small strain regime. To accomplish this, we employ the following strategy:

- Identify suitable mechanical parameters based on the large stresses and strains in the hyperelastic cell walls;
- Develop an appropriate finite deformation analysis;
- Design and test adequate computer models;
- Estimate how the nonlinear parameters account for elastic behaviours in the model structures.

Specifically, we identify two nonlinear parameters, namely a *nonlinear elastic modulus* and a *nonlinear Poisson's ratio* defined in terms of the large stresses and strains in the elastic cell walls, and investigate their utility in estimating how different competing factors contribute to the complex mechanical behaviour of these structures. The formal derivation of key nonlinear elastic parameters in isotropic hyperelastic materials is reviewed in [86]. Analytically, we consider generic cell wall geometries under large strain deformations that can be maintained in every homogeneous, isotropic, incompressible, hyperelastic body by application of suitable tractions, such as a cuboid wall deformed by simple or generalised shear, or bent into a circular wedge, a circular

wedge straightened into a rectangular wall, and a circular cylinder or tube under torsion [9, 50, 51, 53, 57, 98, 128]. For the numerical investigation, finite element simulations of honeycomb-like structures with a small number of square, diamond, or hexagonal cells made from a nonlinear hyperelastic material are presented. In the computer simulations, the size of the cell and the size of the structure are comparable, and therefore the mechanical effects are visible at the cell level and at the structural level simultaneously. The model simulations were produced using the finite element procedure [11, 68, 96] available within the open-source software Finite Elements for Biomechanics (FEBio) environment [73].

In Chapter 2, we give a brief introduction to the mathematical theory of finite strain elasticity relevant for the study presented in this thesis. In Chapter 3, we define and analyse theoretically the nonlinear elastic modulus representing the ratio between the stress and the strain in an elastic body subject to finite deformations, such as stretching, bending, straightening, and twisting. In Chapter 4, we examine numerically a set of computational models representing periodic, honeycomb-like structures with a small number of cells, and show the behaviour of the nonlinear elastic modulus calculated as the ratio between the mean effective stress and the mean effective logarithmic strain in the elastic cell walls as the cell pressure, wall thickness, or number of cells changes. In Chapter 5, we define the nonlinear Poisson's ratio for the model structures subject to uniaxial extension as the negative quotient of the mean value of the logarithmic horizontal strain to that of the logarithmic vertical strain in the solid walls, and analyse its behaviour as the cell wall thickness or number of

cells changes. In Chapter 6, we summarise our results and formulate some further questions regarding the fundamental study of cellular structures of nonlinear elastic material and its relevance to modern applications. In the Appendix, we include some experimental evidence of nonlinear elastic responses in periodic cellular structures obtained from recent physical tests motivated and inspired by our theoretical and computational results. However, since the experimental work was carried out independently using materials with different constitutive parameters, no attempt has been made to compare quantitatively the experimental results with the numerical results reported in this thesis.

Chapter 2

Prerequisites and notation

Elasticity is the ability of a solid to return to its original shape after deformation due to loading. When the deformations under working loads are not detectable by the human eye, the solid's configuration can be considered as fixed, and any changes in the geometry can be neglected. This so-called "small strain" assumption is at the basis of the classical theory of linear elasticity, which is successfully used in structural mechanics and many other engineering applications. However, many modern applications (involving soft solids, inflatable structures, polymers and synthetic rubbers) and biological structures (such as plants and vital organs) involve large deformations. In the framework of large deformations, finite elasticity covers the simplest case where internal forces (stresses) only depend on the present deformation of the body and not on its history (i.e., it excludes plasticity, viscosity, and damage). Because of the large deformations involved, the mathematical models used in finite elasticity are always nonlinear, and the numerical solution of the resulting mathematical equations requires a careful approximation strategy and powerful algorithms [9, 11, 50, 51, 53, 57, 68, 96, 98, 128].

2.1 Large strain deformation

Denoting by $\mathbb{E}$ the three-dimensional (3D) Euclidean space, a continuous material body $\mathcal{B}$ occupies a compact domain $\bar{\Omega}$ of $\mathbb{E}$, and is made of particles whose positions at a time instant t define the configuration of the body. More precisely, a configuration is a smooth mapping of $\bar{\Omega}$ onto a region of $\mathbb{E}$. Among all configurations, we choose one which does not vary in time as the *reference configuration*. We then identify each particle of the body with its position $\mathbf{X}$ in the reference configuration. The interior of the body is identified as an open, bounded, connected subset $\Omega \subset \mathbb{E}$ with boundary $\Gamma = \partial\Omega = \bar{\Omega} \setminus \Omega$. We further assume that Γ is Lipschitz-continuous, and in particular, that a unit normal vector $\mathbf{n}$ exists almost everywhere along Γ.

Definition 2.1.1 The transformation which defines the deformation of the body from the reference (material) configuration $\mathcal{B}_0$ to the current (spatial) configuration $\mathcal{B}$, is a one-to-one, orientation-preserving mapping $\boldsymbol{\chi} : \Omega \to \mathbb{E}$ with $\det(\mathrm{Grad}\, \boldsymbol{\chi}) > 0$ on Ω, such that $\boldsymbol{\chi}$ is injective on Ω (figure 2.1.1). Since self-contact is allowed, this transformation need not be injective on $\bar{\Omega}$.

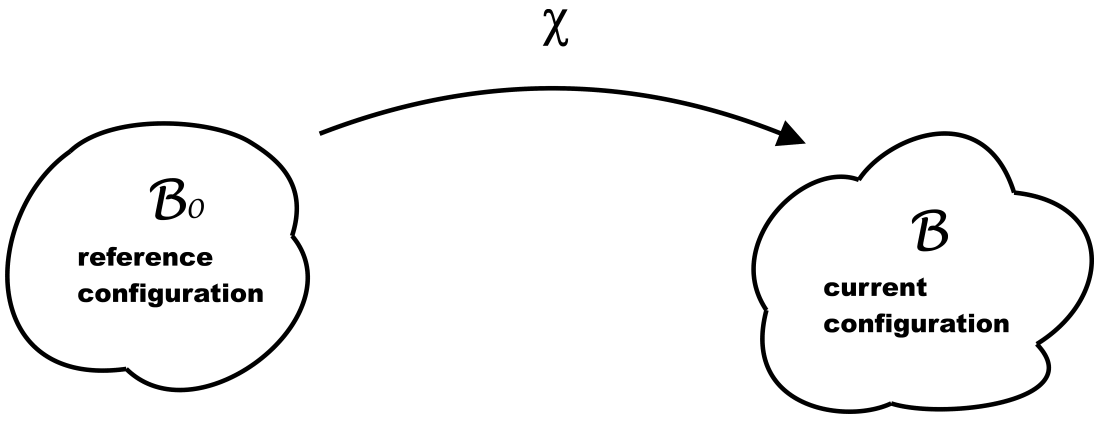

Figure 2.1.1: Schematic of elastic deformation.

Definition 2.1.2 The spatial point $\mathbf{x} = \boldsymbol{\chi}(\mathbf{X})$ corresponds to the place occupied by the particle $\mathbf{X}$ after the deformation χ. The displacement field is then defined, in the usual way, by $\mathbf{u}(\mathbf{X}) = \mathbf{x} - \mathbf{X}$.

Definition 2.1.3 (Lagrangian/material/reference representation) In this representation, one fixes a particle $\mathbf{X}$ (Lagrangian variable) in the reference configuration and observes its distortion $\boldsymbol{\chi}(\mathbf{X})$. This representation is typically used in solid mechanics.

Definition 2.1.4 (Eulerian/spatial/current representation) In this representation, one fixes a point $\mathbf{x}$ (Eulerian variable) in the current configuration and studies what happens at that point as the time progresses. This is generally used in fluid dynamics. It is not so easy to describe free boundaries using this representation.

Deformation of line, area, and volume. The deformation $\boldsymbol{\chi}$ is governed by the deformation gradient

$$\mathbf{F} = \operatorname{Grad} \chi = \begin{bmatrix} \partial\chi_1/\partial X_1 & \partial\chi_1/\partial X_2 & \partial\chi_1/\partial X_3 \\ \partial\chi_2/\partial X_1 & \partial\chi_2/\partial X_2 & \partial\chi_2/\partial X_3 \\ \partial\chi_3/\partial X_1 & \partial\chi_3/\partial X_2 & \partial\chi_3/\partial X_3 \end{bmatrix}.$$

Specifically, the deformation of line is given by the gradient matrix $\mathbf{F}$, the deformation of area by the cofactor matrix $\operatorname{Cof} \mathbf{F} = \det(\mathbf{F})\mathbf{F}^{-T}$, and the deformation of volume by the Jacobian $J = \det \mathbf{F}$, as shown below.

Nanson's formula. [98, p. 88] If $d\mathbf{l}$ is the length of a line element in the current configuration and $d\mathbf{L}$ is the element length in the reference configuration, then

$$d\mathbf{l} = \mathbf{F} d\mathbf{L}.$$

If $d\mathbf{a}$ is the element area in the deformed configuration and $\mathbf{n}$ is its outward unit normal vector, and $d\mathbf{A}$ is the element area in the reference configuration and $\mathbf{N}$ is its outward unit normal vector, then

$$d\mathbf{a} = da\mathbf{n}, \qquad d\mathbf{A} = dA\mathbf{N}.$$

Then the current and reference element volumes are, respectively

$$dv = d\mathbf{a} \cdot d\mathbf{l}, \qquad dV = d\mathbf{A} \cdot d\mathbf{L},$$

and a volume element dV is transformed, after deformation, into the volume element

$$dv = (\det\ \mathbf{F})\, dV = J dV.$$

Hence

$$d\mathbf{a} \cdot d\mathbf{l} = dv = JdV = Jd\mathbf{A} \cdot d\mathbf{L},$$

or equivalently,

$$d\mathbf{a} \cdot \mathbf{F} d\mathbf{L} = Jd\mathbf{A} \cdot d\mathbf{L}.$$

This implies Nanson's relation

$$\mathbf{n}da = J\mathbf{F}^{-T}\mathbf{N}dA = (\text{Cof}\ \mathbf{F})\mathbf{N}dA,$$

where $\mathbf{F}^{-T} = \left(\mathbf{F}^{-1}\right)^T = \left(\mathbf{F}^T\right)^{-1}$.

Piola's identity. If $\mathbf{F}$ is a deformation gradient, and $J = \det \mathbf{F}$, then the following identities hold

$$\text{Div}(J\mathbf{F}^{-T}) = \mathbf{0}, \qquad \text{div}(J^{-1}\mathbf{F}^T) = \mathbf{0},$$

where

$$\text{Div } \mathbf{T} = \begin{bmatrix} \partial T_{1i}/\partial X_i \\ \partial T_{2i}/\partial X_i \\ \partial T_{3i}/\partial X_i \end{bmatrix} \qquad \text{and} \qquad \text{div } \mathbf{T} = \begin{bmatrix} \partial T_{1i}/\partial x_i \\ \partial T_{2i}/\partial x_i \\ \partial T_{3i}/\partial x_i \end{bmatrix}$$

denote the divergence of a second-order tensor field $\mathbf{T} = (T_{ij})_{i,j=1,2,3}$ in the reference and in the current configuration, respectively.

Recalling Nanson's formula,

$$\mathbf{n}da = J\mathbf{F}^{-T}\mathbf{N}dA = (\text{Cof } \mathbf{F})\mathbf{N}dA,$$

we deduce that

$$\begin{aligned} 0 &= \int_B \text{div } \mathbf{I}dv \\ &= \int_{\partial B} \mathbf{n}da = \int_{\partial B_o} (\text{Cof } \mathbf{F})\mathbf{N}dA = \int_{\partial B_o} J\mathbf{F}^{-T}\mathbf{N}dA \\ &= \int_{B_o} \text{Div}(J\mathbf{F}^{-T})dV, \end{aligned}$$

which implies $\text{Div}(J\mathbf{F}^{-T}) = \mathbf{0}$. This is due to the fact that B can be chosen as an arbitrary measurable subset of the body, and therefore, if the integral is equal to zero, then the integrated function is equal to zero. Similarly,

$$\begin{aligned} 0 &= \int_{B_o} \text{Div } \mathbf{I}dV \\ &= \int_{\partial B_o} \mathbf{N}dA = \int_{\partial B} (\text{cof } \mathbf{F})^{-1}\mathbf{n}da = \int_{\partial B} J^{-1}\mathbf{F}^T\mathbf{n}da \\ &= \int_B \text{div}(J^{-1}\mathbf{F}^T)dv, \end{aligned}$$

hence $\text{div}(J^{-1}\mathbf{F}^T) = \mathbf{0}$.

Polar decomposition theorem. Any invertible linear transforma-

tion $\mathbf{F}$, with $\det \mathbf{F} > 0$, has two unique multiplicative decompositions of the form

$$\begin{aligned} \mathbf{F} &= \mathbf{RU} \qquad \text{(right polar decomposition)}, \\ \mathbf{F} &= \mathbf{VR} \qquad \text{(left polar decomposition)}, \end{aligned}$$

where $\mathbf{R}$ is proper orthogonal (i.e., $\mathbf{R}^{-1} = \mathbf{R}^T$, with the superscript T denoting transpose, and $\det \mathbf{R} = 1$), representing the rotation tensor, and $\mathbf{U} = \left(\mathbf{F}^T\mathbf{F}\right)^{1/2}$ and $\mathbf{V} = \left(\mathbf{F}\mathbf{F}^T\right)^{1/2}$ are symmetric and positive definite, representing the right and left stretch tensors, respectively. [128, pp. 52-53], [98, pp. 92-94]

The right Cauchy-Green tensor $\mathbf{C} = \mathbf{F}^T\mathbf{F}$ measures the length of an elementary vector after deformation in terms of its definition in the reference configuration. The left Cauchy-Green tensor $\mathbf{B} = \mathbf{F}\mathbf{F}^T$ measures the length of an elementary vector after deformation in terms of its definition in the current configuration. By the polar decomposition theorem,

$$\mathbf{V} = \mathbf{R}\mathbf{U}\mathbf{R}^T, \tag{2.1.1}$$

hence the stretch tensors $\mathbf{U}$ and $\mathbf{V}$ have the same eigenvalues $\{\lambda_i\}_{i=1,2,3}$, called the principal stretches [98, p. 94]. It follows that the right and left Cauchy-Green tensors satisfy

$$\mathbf{B} = \mathbf{V}^2 = \mathbf{R}\mathbf{U}^2\mathbf{R}^T = \mathbf{R}\mathbf{C}\mathbf{R}^T, \tag{2.1.2}$$

and have the same eigenvalues $\{\lambda_i^2\}_{i=1,2,3}$ [128, pp. 52-53]. Thus the

following principal invariants are well defined

$$
\begin{aligned}
&I_1(\mathbf{B}) = \mathrm{tr}\mathbf{B} = I_1(\mathbf{C}),\\
&I_2(\mathbf{B}) = \mathrm{tr}(\mathrm{Cof}\ \mathbf{B}) = \frac{1}{2}\left[(\mathrm{tr}\ \mathbf{B})^2 - \mathrm{tr}\left(\mathbf{B}^2\right)\right] = I_2(\mathbf{C}),\\
&I_3(\mathbf{B}) = \det \mathbf{B} = I_3(\mathbf{C}).
\end{aligned}
$$

Finite strains. The polar decomposition theorem implies that, in nonlinear elasticity, different strain tensors can be defined [86]:

- The Lagrangian strain tensors [98, p. 156]

$$
\mathbf{e}_L^{(n)} = \begin{cases} \left(\mathbf{U}^n - \mathbf{I}\right)/n & \text{if } n \neq 0, \\ \ln \mathbf{U} & \text{if } n = 0, \end{cases} \tag{2.1.3}
$$

  where $\mathbf{U}$ is the right stretch tensor. In particular, when $n = 2$, the so-called Green-Lagrange strain tensor is obtained, which is often used in practice and is calculated also by the Finite Elements for Biomechanics (FEBio) software [73] employed for our numerical simulations (see Chapters 4 and 5).

- The Eulerian strain tensors [98, p. 159]

$$
\mathbf{e}_E^{(n)} = \begin{cases} \left(\mathbf{V}^n - \mathbf{I}\right)/n & \text{if } n \neq 0, \\ \ln \mathbf{V} & \text{if } n = 0, \end{cases} \tag{2.1.4}
$$

  where $\mathbf{V}$ is the left stretch tensor. By (2.1.1),

$$
\mathbf{e}_E^{(n)} = \mathbf{R}\mathbf{e}_L^{(n)}\mathbf{R}^T. \tag{2.1.5}
$$

For small elastic deformations, all of these strain tensors are equivalent

to the infinitesimal strain from the linear elastic theory

$$\mathbf{e} = \frac{1}{2}\left(\boldsymbol{\nabla}\mathbf{u} + \boldsymbol{\nabla}\mathbf{u}^T\right).$$

Definition 2.1.5 We consider a function

$$m : \mathbb{B} \to \mathbb{R}$$

defined over the set of bodies $\mathbb{B}$, such that, for an arbitrary material body $\mathcal{B} \in \mathbb{B}$,

$$m(\mathcal{B}) \geq 0,$$

and for any two separate bodies $\mathcal{B}, \mathcal{B}' \in \mathbb{B}$,

$$m(\mathcal{B} \cup \mathcal{B}') = m(\mathcal{B}) + m(\mathcal{B}').$$

We call the quantity $m(\mathcal{B})$ the mass of the body $\mathcal{B}$.

Definition 2.1.6 We further assume that the mass m arises from a mass density as follows

$$m(\mathcal{B}) = \int_{\mathcal{B}} \rho(\mathbf{x}, t) dv(\mathbf{x}),$$

where $dv(\mathbf{x})$ is the volume element, and

$$\rho(\mathbf{x}, t) \geq 0, \qquad \forall \mathbf{x} \in \mathcal{B}.$$

We call ρ the mass density of the material in the configuration $\mathcal{B}$.

Principle of mass conservation. Since, by definition, the mass does not depend of the observer, this is an objective scalar, and therefore,

for any arbitrary body $\mathcal{B}$, assuming that no mass is lost or created,

$$\frac{d}{dt}m(\mathcal{B}) = 0 = \frac{d}{dt}\int_{\mathcal{B}} \rho(\mathbf{x}, t)dv(\mathbf{x}),$$

i.e., the mass is conserved regardless of the configuration occupied by $\mathcal{B}$. From the mass conservation principle it follows that, at any time t, if $\mathcal{B}_0$ is a reference configuration of the body, with the corresponding mass density ρ_0 and volume element $dV(\mathbf{X})$, and $\mathcal{B}$ is the current configuration of the body, with the corresponding mass density ρ and volume element dv, then

$$\int_{\mathcal{B}} \rho(\mathbf{x}, t)dv(\mathbf{x}) = \int_{\mathcal{B}_0} \rho_0(\mathbf{X}, t)dV(\mathbf{X}).$$

Thus

$$J\rho = \rho_0,$$

where $J = \det \mathbf{F}$ and $\mathbf{F} = \text{Grad}\, \boldsymbol{\chi}$ is the gradient of the deformation $\boldsymbol{\chi}$ from $\mathcal{B}_0$ to $\mathcal{B}$. This is due to the fact that $\mathcal{B}$ is an arbitrary measurable set, and therefore, if the two integrals are equal, then the corresponding integrated functions are equal. If the deformation is isochoric (i.e., $J = 1$), then $\rho = \rho_0$.

Definition 2.1.7 The linear momentum of the material body $\mathcal{B}$ is defined (in Eulerian form) by

$$\mathbf{M}(\mathcal{B}) = m\mathbf{v} = \int_{\mathcal{B}} \rho(\mathbf{x}, t)\mathbf{v}(\mathbf{x}, t)dv(\mathbf{x}),$$

where $\mathbf{v}(\mathbf{x}, t) = \dot{\boldsymbol{\chi}}(\mathbf{X}, t) = \partial\boldsymbol{\chi}(\mathbf{X}, t)/\partial t$ is the velocity of the material.

Definition 2.1.8 The rotational (angular) momentum of the material

body $\mathcal{B}$ with respect to a point $\mathbf{x}_0$ is defined (in Eulerian form) by

$$\mathbf{H}(\mathcal{B}) = \int_{\mathcal{B}} \rho(\mathbf{x}, t)(\mathbf{x} - \mathbf{x}_0) \times \mathbf{v}(\mathbf{x}, t) dv(\mathbf{x}).$$

In what follows, we consider the concept of force in the context of Newton mechanics, and refer to such forces as "applied forces". Then an applied force (or system of forces) acting on a material body $\mathcal{B}$ may contain a body force defined by

$$\mathbf{F}_b = \int_{\mathcal{B}} \rho(\mathbf{x}, t)\mathbf{b}(\mathbf{x}, t) dv(\mathbf{x}),$$

where $\mathbf{b}$ is the (external) body-force density (body-force per unit mass) defined on the body $\mathcal{B}$ (e.g., gravity), and a surface (contact) force (traction)

$$\mathbf{F}_c = \int_{\partial\mathcal{B}} \mathbf{c}(\mathbf{x}, \partial\mathcal{B}) da(\mathbf{x}),$$

where $\mathbf{c}$ is the (internal) contact force density defined over any piecewise smooth oriented surface in $\mathcal{B} \cup \partial\mathcal{B}$, and may consist of a tangential component, which is parallel to the surface (e.g., friction), and a normal component, which is perpendicular to the surface (e.g., pressure), and $a(\mathbf{x})$ is the surface element. The resultant (total) applied force is then

$$\mathbf{F}_r = \int_{\mathcal{B}} \rho(\mathbf{x}, t)\mathbf{b}(\mathbf{x}, t) dv(\mathbf{x}) + \int_{\partial\mathcal{B}} \mathbf{c}(\mathbf{x}, \partial\mathcal{B}) da(\mathbf{x}),$$

and the resultant moment (or torque) of the applied forces about a point $\mathbf{x}_0$ is

$$\mathbf{G}_r = \int_{\mathcal{B}} \rho(\mathbf{x}, t)(\mathbf{x} - \mathbf{x}_0) \times \mathbf{b}(\mathbf{x}, t) dv(\mathbf{x}) + \int_{\partial\mathcal{B}} (\mathbf{x} - \mathbf{x}_0) \times \mathbf{c}(\mathbf{x}, \partial\mathcal{B}) da(\mathbf{x}).$$

Force balance laws. From Newton's laws of dynamics, it follows that

there is a balance between the resultant moment of applied forces and the rate of change of linear momentum of the body

$$\frac{d\mathbf{M}}{dt} = \mathbf{F}_r,$$

i.e.,

$$\frac{d}{dt}\int_{\mathcal{B}} \rho(\mathbf{x},t)\mathbf{v}(\mathbf{x},t)dv(\mathbf{x}) = \int_{\mathcal{B}} \rho(\mathbf{x},t)\mathbf{b}(\mathbf{x},t)dv(\mathbf{x}) + \int_{\partial\mathcal{B}} \mathbf{c}(\mathbf{x},\partial\mathcal{B})da(\mathbf{x}),$$

or equivalently,

$$\int_{\mathcal{B}} \rho(\mathbf{x},t)\dot{\mathbf{v}}(\mathbf{x},t)dv(\mathbf{x}) = \int_{\mathcal{B}} \rho(\mathbf{x},t)\mathbf{b}(\mathbf{x},t)dv(\mathbf{x}) + \int_{\partial\mathcal{B}} \mathbf{c}(\mathbf{x},\partial\mathcal{B})da(\mathbf{x}),$$

where $\dot{\mathbf{v}}(\mathbf{x},t) = \partial\mathbf{v}(\mathbf{x},t)/\partial t = \ddot{\boldsymbol{\chi}}(\mathbf{X},t) = \partial^2\boldsymbol{\chi}(\mathbf{X},t)/\partial t^2$ is the acceleration of the material. Similarly, there is a balance between the resultant moment of applied forces and the rate of change of rotational (angular) momentum of the body

$$\frac{d\mathbf{H}}{dt} = \mathbf{G}_r,$$

i.e.,

$$\frac{d}{dt}\int_{\mathcal{B}} \rho(\mathbf{x},t)(\mathbf{x}-\mathbf{x}_0)\times\mathbf{v}(\mathbf{x},t)dv(\mathbf{x}) = \int_{\mathcal{B}} \rho(\mathbf{x},t)(\mathbf{x}-\mathbf{x}_0)\times\mathbf{b}(\mathbf{x},t)dv(\mathbf{x}) + \int_{\partial\mathcal{B}} (\mathbf{x}-\mathbf{x}_0)\times\mathbf{c}(\mathbf{x},\partial\mathcal{B})da(\mathbf{x}),$$

or equivalently,

$$\int_{\mathcal{B}} \rho(\mathbf{x},t)(\mathbf{x}-\mathbf{x}_0)\times\dot{\mathbf{v}}(\mathbf{x},t)dv(\mathbf{x}) = \int_{\mathcal{B}} \rho(\mathbf{x},t)(\mathbf{x}-\mathbf{x}_0)\times\mathbf{b}(\mathbf{x},t)dv(\mathbf{x}) + \int_{\partial\mathcal{B}} (\mathbf{x}-\mathbf{x}_0)\times\mathbf{c}(\mathbf{x},\partial\mathcal{B})da(\mathbf{x}).$$

From the above balance laws, we deduce that the body $\mathcal{B}$ is in *static*

equilibrium if the total force and the total torque satisfy respectively

$$\mathbf{F}_r = \int_{\mathcal{B}} \rho(\mathbf{x})\mathbf{b}(\mathbf{x})dv(\mathbf{x}) + \int_{\partial\mathcal{B}} \mathbf{c}(\mathbf{x}, \partial\mathcal{B})da(\mathbf{x}) = 0$$

and

$$\mathbf{G}_r = \int_{\mathcal{B}} \rho(\mathbf{x})(\mathbf{x}-\mathbf{x}_0)\times\mathbf{b}(\mathbf{x})dv(\mathbf{x}) + \int_{\partial\mathcal{B}} (\mathbf{x}-\mathbf{x}_0)\times\mathbf{c}(\mathbf{x}, \partial\mathcal{B})da(\mathbf{x}) = 0.$$

Forces and stress. From the static equilibrium principle, we obtain

$$-\int_{\partial\mathcal{B}} \mathbf{c}(\mathbf{x}, \partial\mathcal{B})da(\mathbf{x}) = \int_{\mathcal{B}} \rho(\mathbf{x})\mathbf{b}(\mathbf{x})dv(\mathbf{x}).$$

We assume that $\mathbf{c}(\mathbf{x}, \partial\mathcal{B})$ has the same value for all surfaces through $\mathbf{x}$, with the outward unit normal vector $\mathbf{n}$ at $\mathbf{x}$, and denote $\mathbf{c}(\mathbf{x}, \partial\mathcal{B}) = \mathbf{c}(\mathbf{x}, \mathbf{n})$. This is *Cauchy's fundamental postulate*, stating that traction is a function of $\mathbf{x}$ and depends on the internal surface only through its outward normal $\mathbf{n}$ (i.e., it is not influenced by the curvature). Then the following result holds.

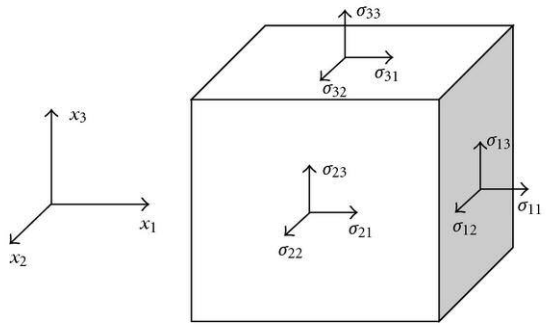

Figure 2.1.2: Schematic of the components of the Cauchy stress tensor in a cuboid of elastic material.

Cauchy theorem If $\mathbf{c}(\mathbf{x}, \mathbf{n})$ is continuous in $\mathbf{x}$, then there exists a 2nd-order tensor field $\boldsymbol{\sigma}$, called the Cauchy (or true) stress tensor

(figure 2.1.2), such that [98, pp. 146-147]

$$\boldsymbol{\sigma}(\mathbf{x})\mathbf{n} = \mathbf{c}(\mathbf{x}, \mathbf{n}).$$

By the Divergence Theorem,

$$\begin{aligned} -\int_{\mathcal{B}} \text{div } \boldsymbol{\sigma}(\mathbf{x}) dv(\mathbf{x}) &= -\int_{\partial\mathcal{B}} \boldsymbol{\sigma}(\mathbf{x})\mathbf{n} da(\mathbf{x}) \\ &= -\int_{\partial\mathcal{B}} \mathbf{c}(\mathbf{x}, \mathbf{n}) da(\mathbf{x}) \\ &= \int_{\mathcal{B}} \rho(\mathbf{x})\mathbf{b}(\mathbf{x}) dv(\mathbf{x}). \end{aligned}$$

Since $\mathcal{B}$ is an arbitrary measurable set, the fact that the integrals are equal implies that the corresponding integrated functions are equal. After eliminating the integral, we deduce the following equilibrium equation in Eulerian (current) representation

$$\text{div } \boldsymbol{\sigma}(\mathbf{x}) + \rho(\mathbf{x})\mathbf{b}(\mathbf{x}) = 0 \qquad \text{(3 equations)}.$$

Furthermore, the conservation of angular momentum implies

$$\boldsymbol{\sigma}(\mathbf{x}) = \boldsymbol{\sigma}(\mathbf{x})^T \qquad \text{(symmetry)}.$$

See [98, 149] for a detailed proof. These field equations provide 3 scalar equations for the 9 unknowns: $\{\chi_i\}_{i=1,2,3}$, $\{\sigma_{ij}\}_{i\leq j=1,2,3}$. In order to solve them, these equations must be completed by the *constitutive law for* $\boldsymbol{\sigma}$ depending on material properties (6 scalar equations), and supplemented by *boundary conditions*.

Definition 2.1.9 The normal stress is defined by

$$\sigma_n = \mathbf{n} \cdot (\boldsymbol{\sigma}\mathbf{n}),$$

where $\mathbf{n}$ is the unit vector in the normal direction (perpendicular to the surface). If $\sigma_n > 0$, then the normal stress is tensile, and if $\sigma_n < 0$, then the normal stress is compressive. The associated tangential (shear) stress is defined by

$$\sigma_t = (\boldsymbol{\sigma}\mathbf{n}) - [\mathbf{n} \cdot (\boldsymbol{\sigma}\mathbf{n})]\mathbf{n}.$$

Definition 2.1.10 The hydrostatic stress tensor is defined as

$$\boldsymbol{\sigma} = \text{diag}(-p) = -p\mathbf{I},$$

where p is a scalar function.

Piola transform. The Piola transform is the basic tool for transforming the Cauchy stress tensor while preserving the structure of the equations of equilibrium. In the reference configuration, by the Divergence Theorem and Nanson's formula, it follows that

$$\begin{aligned}\int_{\mathcal{B}} \text{div } \boldsymbol{\sigma} dv &= \int_{\partial\mathcal{B}} \boldsymbol{\sigma}\mathbf{n} da \\ &= \int_{\partial\mathcal{B}_0} \boldsymbol{\sigma} \left(\text{Cof } \mathbf{F}\right) \mathbf{N} dA \\ &= \int_{\partial\mathcal{B}_0} \mathbf{P}\mathbf{N} dA \\ &= \int_{\mathcal{B}_0} \text{Div } \mathbf{P} dV,\end{aligned}$$

where

$$\mathbf{P} = \boldsymbol{\sigma} \text{ Cof } \mathbf{F} = J\boldsymbol{\sigma}\mathbf{F}^{-T}$$

is called the 1st Piola-Kirchhoff (PK) stress tensor. Its transpose $\mathbf{P}^T$ is known as the nominal stress. From the above relations and the

equilibrium equation involving the Cauchy stress tensor, we obtain

$$-\int_{\mathcal{B}_0} \text{Div } \mathbf{P} dV = -\int_{\mathcal{B}} \text{div } \boldsymbol{\sigma} dv = \int_{\mathcal{B}} \rho \mathbf{b} dv = \int_{\mathcal{B}_0} \rho_0 \mathbf{b}_0 dV,$$

where $\rho_0(\mathbf{X}) = J\rho(\mathbf{x})$ and $\mathbf{b}_0(\mathbf{X}) = J^{-1}\mathbf{b}(\chi(\mathbf{X}))$. Then the equilibrium equation in Lagrangian (reference) representation takes the form

$$-\text{Div } \mathbf{P}(\mathbf{X}) = \rho_0(\mathbf{X})\mathbf{b}_0(\mathbf{X}).$$

Since, in general, the 1st Piola-Kirchhoff stress is not symmetric, the 2nd Piola-Kirchhoff can be used instead. This is defined by

$$\mathbf{S} = \mathbf{F}^{-1}\mathbf{P} = J\mathbf{F}^{-1}\boldsymbol{\sigma}\mathbf{F}^{-T}.$$

2.2 Hyperelastic materials

Hyperelastic (or Green elastic) materials are the class of homogeneous elastic material models described by a *strain (or stored) energy density* function (free energy per unit volume of the undeformed configuration) [9, 50, 51, 53, 57, 98, 128]. In this thesis, we consider homogeneous isotropic hyperelastic material, which can be described by a strain energy function $\mathcal{W}(\mathbf{F})$ depending only on the deformation gradient $\mathbf{F}$. Then, by the principles of material objectivity (frame indifference), stating that *constitutive equations must be invariant under changes of frame of reference* [128, p. 44], and material symmetry due to isotropy, the scalar strain energy function can be expressed equivalently in terms of the principal invariants, I_1, I_2, I_3, of the Cauchy-Green tensors $\mathbf{B}$ and $\mathbf{C}$ [122], or alternatively, in terms of the principal stretches, $\lambda_1, \lambda_2, \lambda_3$. In order to simplify the notation, we represent the strain

energy function as $\mathcal{W}$ and infer its argument from the context [98]. The corresponding Cauchy stress tensor takes on the following representation in terms of the left Cauchy-Green tensor $\mathbf{B}$ [9]

$$\boldsymbol{\sigma} = \beta_0\mathbf{I} + \beta_1\mathbf{B} + \beta_{-1}\mathbf{B}^{-1}, \tag{2.2.1}$$

where the elastic response coefficients

$$\begin{aligned} \beta_0 &= \frac{2}{\sqrt{I_3}}\left(I_2\frac{\partial\mathcal{W}}{\partial I_2} + I_3\frac{\partial\mathcal{W}}{\partial I_3}\right), \\ \beta_1 &= \frac{2}{\sqrt{I_3}}\frac{\partial\mathcal{W}}{\partial I_1}, \\ \beta_{-1} &= -2\sqrt{I_3}\frac{\partial\mathcal{W}}{\partial I_2} \end{aligned} \tag{2.2.2}$$

are scalar functions of the principal invariants. For incompressible materials,

$$\boldsymbol{\sigma} = -p\mathbf{I} + \beta_1\mathbf{B} + \beta_{-1}\mathbf{B}^{-1}, \tag{2.2.3}$$

where p is the Lagrange multiplier associated with the incompressibility constraint $J = 1$, also referred to as the arbitrary hydrostatic pressure [98, p. 200].

Remark 2.2.1 Note that, by (2.2.1)-(2.2.3), the Cauchy stress tensor $\boldsymbol{\sigma}$ and the left Cauchy-Green tensor $\mathbf{B}$ have the same eigenvectors, i.e., these two tensors are coaxial. This is an important observation for our subsequent analysis where nonlinear elastic moduli will be defined.

Simple tension. Next, we consider a homogeneous isotropic hyperelastic material subject to the following triaxial stretch

$$x_1 = \lambda_1 X_1, \qquad x_2 = \lambda_2 X_2, \qquad x_3 = \lambda_3 X_3, \tag{2.2.4}$$

where $\mathbf{X} = [X_1, X_2, X_3]^T$ and $\mathbf{x} = [x_1, x_2, x_3]^T$ denote the reference (Lagrangian, material) and current (Eulerian, spatial) coordinates, respectively, and $\lambda_i > 0$, $i = 1, 2, 3$, are positive constants. For a hyperelastic body under uniaxial (simple) tension acting in the first direction, the Cauchy stress takes the form

$$\boldsymbol{\sigma} = \begin{bmatrix} T & 0 & 0 \\ 0 & 0 & 0 \\ 0 & 0 & 0 \end{bmatrix}. \tag{2.2.5}$$

In this case, it can be shown that the corresponding deformation is a simple extension in the direction of the (positive) tensile force, $T > 0$, where the ratio between the tensile strain and the strain in the orthogonal direction is greater than one, if and only if the Baker-Ericksen (BE) inequalities stating that *the greater principal stress occurs in the direction of the greater principal stretch* hold [74, 82, 83, 91]. In other words, the deformation corresponding to (2.2.5), where $\sigma_{11} > 0$, has the form (2.2.4) where $\lambda_1 > \lambda_2 = \lambda_3 > 0$ if and only if the following BE inequalities hold

$$\beta_1 \lambda_i^2 \lambda_j^2 - \beta_{-1} > 0, \quad \text{for} \quad i, j = 1, 2, 3, \ i \neq j. \tag{2.2.6}$$

In the special case when this deformation is isochoric, i.e., $I_3 = 1$, the axial stretches take the form $\lambda_1 = \lambda$ and $\lambda_2 = \lambda_3 = 1/\sqrt{\lambda}$, and the non-zero component of the Cauchy stress is

$$\sigma_{11} \ = \ (\lambda\beta_1 - \beta_{-1}) \left(\lambda - \frac{1}{\lambda^2} \right).$$

For this deformation, the BE inequalities are equivalent to

$$\lambda\beta_1 - \beta_{-1} > 0, \tag{2.2.7}$$

i.e., $\sigma_{11} > 0$ for $\lambda > 1$, and $\sigma_{11} < 0$ for $\lambda < 1$, or in other words, axial tension produces elongation in the same direction, and axial compression produces contraction in the same direction. So the pressure-compression (PC) inequalities [128, p. 155] hold also. We conclude that, for this deformation, BE $\Leftrightarrow$ PC. In practice, a mean version of the PC conditions is also acceptable, namely

$$\sigma_1\left(1-\frac{1}{\lambda_1}\right)+\sigma_2\left(1-\frac{1}{\lambda_2}\right)+\sigma_3\left(1-\frac{1}{\lambda_3}\right)>0, \tag{2.2.8}$$

where λ_i and σ_i, $i = 1, 2, 3$, are the principal stretches and the principal stresses, respectively, if not all λ_i are equal to 1. For the above isochoric deformation, since $\sigma_{22} = \sigma_{33} = 0$, the PC inequality (2.2.8) is

$$\sigma_{11}\left(1-\frac{1}{\lambda}\right)=(\lambda\beta_1-\beta_{-1})\left(\lambda-\frac{1}{\lambda^2}\right)\left(1-\frac{1}{\lambda}\right)>0, \tag{2.2.9}$$

and is equivalent to the BE inequality (2.2.7).

Then, if $\lambda > 1$, the deformation is a simple (or uniaxial) extension in the X_1-direction, and if $\lambda < 1$, the deformation is a equibiaxial extension in the orthogonal directions.

Necking instability. When subjected to the normal tension

$$\lambda_1 = \lambda > 1, \quad \lambda_2 = \lambda_3 = 1/\sqrt{\lambda} < 1, \tag{2.2.10}$$

an hyperelastic material characterised by $\widehat{\mathcal{W}}(\lambda) = \mathcal{W}(\lambda_1, \lambda_2, \lambda_3)$ may manifest the so-called necking instability whereby there exists a critical

stretch $\lambda_{cr} > 1$, such that the function

$$\widehat{\mathcal{W}}'(\lambda) = \frac{\partial \widehat{\mathcal{W}}}{\partial \lambda} \tag{2.2.11}$$

is not everywhere increasing as $\lambda > \lambda_{cr}$ increases, and therefore the force required to extend the material may decrease. In view of the subsequent computational models, we consider here the classical Mooney-Rivlin model [92] characterised by the strain energy density function

$$\mathcal{W}(\lambda_1, \lambda_2, \lambda_3) = \frac{C_1}{2}\left(\lambda_1^2 + \lambda_2^2 + \lambda_3^2 - 3\right) + \frac{C_2}{2}\left(\lambda_1^{-2} + \lambda_2^{-2} + \lambda_3^{-2} - 3\right), \tag{2.2.12}$$

where $C_1 > 0$ and $C_2 > 0$ are independent of deformation. If $C_2 = 0$, then this material model reduces to the classical neo-Hookean model [110]. If a Mooney-Rivlin material is subject to the normal tension (2.2.10), then the strain energy function (2.2.12) takes the form

$$\mathcal{W}(\lambda) = \frac{C_1}{2}\left(\lambda^2 + 2\lambda^{-1} - 3\right) + \frac{C_2}{2}\left(\lambda^{-2} + 2\lambda - 3\right),$$

its derivative is

$$\widehat{\mathcal{W}}'(\lambda) = \frac{\partial \widehat{\mathcal{W}}}{\partial \lambda} = C_1\left(\lambda - \lambda^{-2}\right) + C_2\left(1 - \lambda^{-3}\right),$$

and it always increases, since the second derivative is always positive, i.e.,

$$\widehat{\mathcal{W}}''(\lambda) = \frac{\partial^2 \widehat{\mathcal{W}}}{\partial \lambda^2} = C_1\left(1 + 2\lambda^{-3}\right) + 3C_2\lambda^{-4} > 0.$$

Hence, necking instability does not occur in Mooney-Rivlin materials.

2.3 Boundary value problems

The equilibrium of an elastic body in the presence of a dead (constant) load is described in terms of the Cauchy (true) stress by the Eulerian field equation

$$-\text{div}\ \boldsymbol{\sigma}(\mathbf{x}) = \mathbf{f}(\mathbf{x}). \tag{2.3.1}$$

The above governing equation is completed by the constitutive law for $\boldsymbol{\sigma}$ depending on material properties, and supplemented by boundary conditions. Since the domain occupied by the deformed material is usually unknown, it is more convenient to rewrite the above equilibrium problem as an equivalent problem in the reference (undeformed) configuration where the independent variables are $\mathbf{X} \in \Omega$. The corresponding Lagrangian equation of nonlinear elastostatics is

$$-\text{Div}\ \mathbf{P}(\mathbf{X}) \ = \ \mathbf{f}(\mathbf{X}), \tag{2.3.2}$$

where $\mathbf{P} = \boldsymbol{\sigma}\ \text{Cof}\ \mathbf{F}$ is the 1st Piola-Kirchhoff stress tensor, $\mathbf{F} = \text{Grad}\ \boldsymbol{\chi}$ is the gradient of the deformation $\boldsymbol{\chi}(\mathbf{X}) = \mathbf{x}$, such that $J = \det \mathbf{F} > 0$, and for dead loading, $\mathbf{f}(\mathbf{X}) = J\mathbf{f}(\mathbf{x})$.

Boundary conditions. The general boundary value problem is to find the displacement $\mathbf{u}(\mathbf{X}) = \mathbf{x} - \mathbf{X}$, for all $\mathbf{X} \in \Omega$, that satisfies the equilibrium equation (2.3.2) subject to the Dirichlet (displacement) boundary conditions

$$\mathbf{u}(\mathbf{X}) = \mathbf{u}_D \ \text{ on } \ \emptyset \neq \Gamma_D \subset \partial\Omega, \tag{2.3.3}$$

and the Neumann (stress) boundary conditions

$$\mathbf{P}(\mathbf{X})\mathbf{N} = \mathbf{g} = \boldsymbol{\tau}\,(\text{Cof}\ \mathbf{F})\,\mathbf{N} \ \text{ on } \ \Gamma_N = \partial\Omega \setminus \Gamma_D, \tag{2.3.4}$$

where $\mathbf{N}$ is the outward unit normal vector to the (reference) domain boundary $\partial\Omega$, and $\boldsymbol{\tau}\mathbf{n}$ is the (true) applied surface traction in the deformed configuration. At the boundary points where subsets with Dirichlet conditions and Neumann conditions intersect, the Dirichlet conditions take priority, and when subsets with different Neumann conditions intersect, these conditions are imposed simultaneously. However, in many cases, the solution may not be unique.

Semi-inverse approach. The semi-inverse method is one of the very few methods to obtain exact solution in continuum mechanics. It consists of the following steps:

1. Describe:
   (a) The material characteristics (e.g., hyperelastic), its geometry, and whether it is in a static or dynamic state;
   (b) The deformation and the boundary conditions.
2. Deduce:
   (a) The material responses (stresses);
   (b) The mechanical behaviour (e.g., stiffening or softening).

For many complex deformations, the deformation cannot be prescribed and therefore the semi-inverse method cannot be employed. In some cases, approximate solutions to the boundary value problem can be obtained by suitable numerical procedures. For hyperelastic materials, boundary value problems can be cast as variational problems which can be used to generate finite element methods.

Chapter 3

Enhanced elasticity of core-rind cellular structures

3.1 Introduction

In nature and engineering, cellular materials are designed to perform certain functions while using as little material as possible (e.g., by minimizing an objective such as volume or density), provided that they meet some target values on common physical properties (e.g., strength, stiffness, thermal conductivity) [3, 7, 8, 19, 44, 49, 54, 58, 109, 114, 115, 131]. For example, many natural cellular structures maintain their integrity under unforeseen or more typical loading conditions by adjusting their composition or quantity in responses to changes in loads through a combination of fibre reinforcement or thickening of the walls in load-bearing regions: bones of larger animals are thicker in proportion to their size than those of smaller animals, while bones in the skull are less dense than those in the legs; in monocotyledon stems (e.g., corn, palm, bamboo), mechanical failure is prevented through a combination of initiation of growth with an overbuilt stem that is sufficiently wide for future support demands and sustained sclerification

(thickening and lignification) of cell walls toward the stem periphery and base. Moreover, in many living, load-bearing structures, the cells are not voids, but are chambers filled with a liquid or solid core. For example, paw and foot cushions are part of the locomotor system designed to absorb mechanical shock, redistribute excessive local stress, and store and return elastic strain energy. Histologically, they are soft cellular bodies built from closed compartments or cells separated by collagen reinforced elastic septa and filled with fat (adipose tissue) [1, 12, 23, 24, 60, 65, 67, 90, 93–95, 106, 112, 136]. While new optimisation criteria associated with different stages of development or healing in natural structures are still to be identified, there is also a need for appropriate theoretical approaches to be developed that take into account the large stress and strain fields caused by physiological or pathological change.

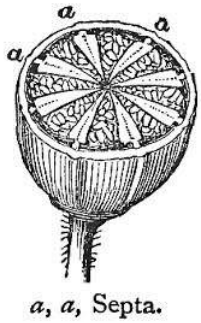

Figure 3.1.1: Schematic of natural cellular structure.

For "cell-filled" or "core-rind" composite structures (figure 3.1.1), several main factors determine the magnitude of the stress level in the cellular material, including the individual cell geometry, the cell wall thickness, and the presence of cell inclusions. In the case of small strain deformations, a comparison between empty and fluid-filled cells was proposed by Warner *et al.* (1999) [134], where it was shown that, if a

cell wall is bent, then the elastic modulus in the direction of the force causing the deflection increases in a fluid-filled cell compared to that of an empty cell. Indeed, if the underlying material is linearly elastic, then the dominant mechanism for the deformation of a cellular body is the bending of the cell walls, and thresholds on strength or stiffness can be set as constraints in the optimal design process [49, 115]. However, an additional level of difficulty arises when the cell wall material is nonlinear elastic, in which case, if the elastic modulus is constrained, then the existence of a feasible solution is not guaranteed, and must be established before this modulus can be used to predict other structural properties. In figure 3.1.2, examples are shown where an optimal solution (a) exists under the linear constraints and (b) does not exist under the nonlinear constraints.

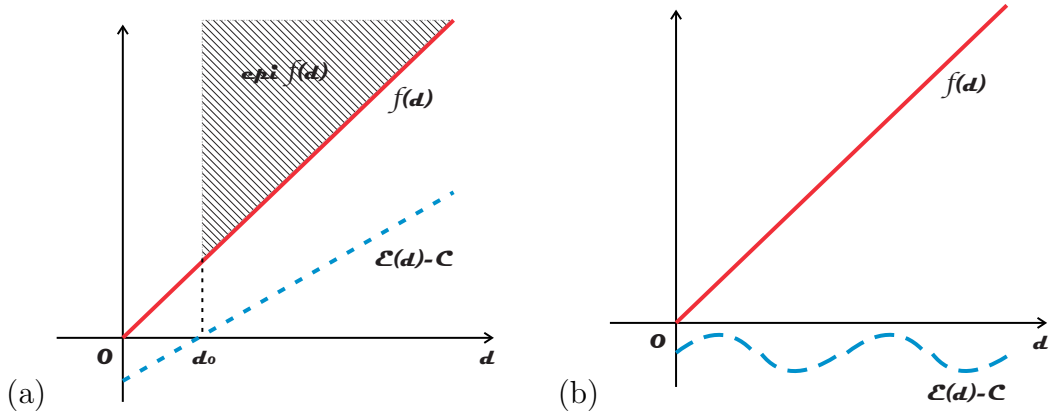

Figure 3.1.2: (a) Epigraph of function $f : V = \{d > 0 \mid \mathcal{E}(d) \geq C\} \to \mathbb{R},\ f(d) = d$; (b) Failure of constraint qualification $\mathcal{E}(d) \geq C$ $(V = \emptyset)$.

In this chapter, we compare the mechanical performance for individual cell walls of homogeneous, incompressible, isotropic, hyperelastic material in a single cell which is either empty or filled with an incompressible fluid or a compliant, elastic core, and subject to large strain deformations (figure 3.1.3). Analytically, for three generic cell walls of nonlinear hyperelastic material under large strain defor-

mations that can be maintained in every homogeneous, isotropic, incompressible, hyperelastic body by application of suitable tractions, namely a rectangular beam bent into a circular wedge, a circular wedge straighten into a rectangular wall, and a circular tube subject to torsion, we prove that the nonlinear elastic modulus representing the ratio between the stress and the strain in a principal direction associated with the largest change of curvature increases with increasing applied pressure, and also when the thickness of the wall increases or when the wall becomes multi-layer. Similarly, if a circular tube is filled with an incompressible elastic core, then the radial elastic modulus of the cylindrical core is enhanced also by the presence of a surrounding tube.

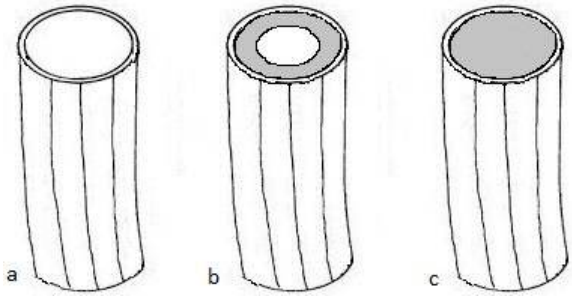

Figure 3.1.3: Schematic of (a) empty, (b) partially, and (c) fully filled circular tube.

For solid cellular structures with uniform cell size, wall thickness, and shape, another important question is whether the same volume of cell wall material has the same effect when arranged as many small cells or as fewer large cells. For the bending and stretching of a cuboid wall, the straightening and stretching of an annular wedge, and the extension and torsion of a circular cylindrical tube, we demonstrate that the mean value of the nonlinear elastic modulus representing the ratio between the stress and the strain in the direction associated with the largest change of curvature in multiple thin walls deforming sepa-

rately is greater than the mean modulus of a single thick wall, and this modulus increases as the number of thin walls increases while the total volume of elastic material remains fixed. Since the results obtained here are independent of the choice of the strain energy function describing the cell wall material, the nonlinear elastic modulus identified here can be taken as indicative for finding the optimum wall thickness, number of walls, or cell pressure under similar deformations in a wide range of different hyperelastic materials. In contrast, when the cell wall material is linearly elastic, the elastic modulus of the cell wall is independent of initial cell pressure [48, p. 253]. For a circular tube of nonlinear elastic material also, the classical torsion modulus, measured as the ratio between the torque and the twist, increases as the tube thickness increases, but is independent of the applied pressure.

In Section 3.2, we define and analyse the nonlinear elastic modulus for a rectangular wall which is bent into an annular wedge. Similarly, in Section 3.3, we study the elastic modulus for an annular wedge which is straighten into a rectangular wall. In Section 3.4, we investigate the moduli of a circular tube which is stretched and twisted.

3.2 Bending of rectangular walls

A cuboid cell wall with reference geometry $(X, Y, Z) \in [X_1, X_2] \times [-Y_0, Y_0] \times [-Z_0, Z_0]$, where X_1, X_2, Y_0 and Z_0 are positive constants, is deformed by the triaxial stretch [128, pp. 186-188]

$$\tilde{X} = aX, \qquad \tilde{Y} = \frac{1}{\sqrt{a}}Y, \qquad \tilde{Z} = \frac{1}{\sqrt{a}}Z, \tag{3.2.1}$$

where $(\tilde{X}, \tilde{Y}, \tilde{Z})$ and (X, Y, Z) are the Cartesian coordinates for the deformed and the reference configuration, respectively, and a is a positive constant. For the deformation (3.2.1), the deformation gradient satisfies

$$\begin{bmatrix} d\tilde{X} \\ d\tilde{Y} \\ d\tilde{Z} \end{bmatrix} = \mathbf{F} \begin{bmatrix} dX \\ dY \\ dZ \end{bmatrix}$$

and is equal to:

$$\mathbf{F} = \begin{bmatrix} d\tilde{X}/dX & 0 & 0 \\ 0 & d\tilde{Y}/dY & 0 \\ 0 & 0 & d\tilde{Z}/dZ \end{bmatrix} = \begin{bmatrix} a & 0 & 0 \\ 0 & 1/\sqrt{a} & 0 \\ 0 & 0 & 1/\sqrt{a} \end{bmatrix}.$$

The associated left Cauchy-Green tensor and its inverse are respectively

$$\mathbf{B} = \mathbf{F}\mathbf{F}^T = \begin{bmatrix} a^2 & 0 & 0 \\ 0 & 1/a & 0 \\ 0 & 0 & 1/a \end{bmatrix}, \qquad \mathbf{B}^{-1} = \begin{bmatrix} 1/a^2 & 0 & 0 \\ 0 & a & 0 \\ 0 & 0 & a \end{bmatrix}.$$

By the representation (2.2.3), the non-zero components of the corresponding Cauchy stress tensor take the form

$$\sigma^{(0)}_{\tilde{X}\tilde{X}} = -p + \beta_1 a^2 + \frac{\beta_{-1}}{a^2}, \qquad \sigma^{(0)}_{\tilde{Y}\tilde{Y}} = \sigma^{(0)}_{\tilde{Z}\tilde{Z}} = -p + \frac{\beta_1}{a} + \beta_{-1} a.$$

Next, the deformed wall is "bent" into a sector of a circular cylindrical tube (annular wedge) by the deformation [128, pp. 186-188]

$$r = \sqrt{2\tilde{X}}, \qquad \theta = A\tilde{Y}, \qquad z = \frac{\tilde{Z}}{A}, \tag{3.2.2}$$

where $(r, \theta, z) \in [r_1, r_2] \times [-\theta_0, \theta_0] \times [-z_0, z_0]$ are the cylindrical polar coordinates for the current configuration, and r_1, r_2, θ_0, z_0, and A are positive constants (figure 3.2.1).

The combined deformation given by the successive deformations (3.2.1) and (3.2.2) takes the form [128, pp. 186-188]

$$r = \sqrt{2aX}, \qquad \theta = \frac{AY}{\sqrt{a}}, \qquad z = \frac{Z}{A\sqrt{a}}. \tag{3.2.3}$$

For this deformation, the gradient satisfies

$$\begin{bmatrix} dr \\ rd\theta \\ dz \end{bmatrix} = \mathbf{F} \begin{bmatrix} dX \\ dY \\ dZ \end{bmatrix}.$$

hence, in terms of the current cylindrical polar coordinates (r, θ, z), the deformation gradient takes the form

$$\mathbf{F} = \begin{bmatrix} \partial r/\partial X & 0 & 0 \\ 0 & r\partial\theta/\partial Y & 0 \\ 0 & 0 & \partial z/\partial Z \end{bmatrix} = \begin{bmatrix} a/r & 0 & 0 \\ 0 & Ar/\sqrt{a} & 0 \\ 0 & 0 & 1/(A\sqrt{a}) \end{bmatrix}.$$

The corresponding left Cauchy-Green tensor and its inverse are respectively

$$\mathbf{B} = \mathbf{F}\mathbf{F}^T = \begin{bmatrix} a^2/r^2 & 0 & 0 \\ 0 & A^2r^2/a & 0 \\ 0 & 0 & 1/(A^2a) \end{bmatrix},$$

$$\mathbf{B}^{-1} = \begin{bmatrix} r^2/a^2 & 0 & 0 \\ 0 & a/\left(A^2r^2\right) & 0 \\ 0 & 0 & A^2a \end{bmatrix}.$$

By (2.2.3), the non-zero components of the associated Cauchy stress tensor can be expressed as follows

$$\begin{aligned}
\sigma_{rr} &= -p + \beta_1 \frac{a^2}{r^2} + \beta_{-1} \frac{r^2}{a^2}, \\
\sigma_{\theta\theta} &= -p + \beta_1 \frac{A^2 r^2}{a} + \beta_{-1} \frac{a}{A^2 r^2}, \\
\sigma_{zz} &= -p + \beta_1 \frac{1}{A^2 a} + \beta_{-1} A^2 a.
\end{aligned} \tag{3.2.4}$$

In the absence of body forces, by the equilibrium equation (2.3.1), the components of the Cauchy stress tensor satisfy the following system of equilibrium equations [98, p. 65]

$$\begin{aligned}
&\frac{\partial \sigma_{rr}}{\partial r} + \frac{1}{r}\frac{\partial \sigma_{\theta r}}{\partial \theta} + \frac{\partial \sigma_{zr}}{\partial z} + \frac{1}{r}(\sigma_{rr} - \sigma_{\theta\theta}) = 0, \\
&\frac{\partial \sigma_{r\theta}}{\partial r} + \frac{1}{r}\frac{\partial \sigma_{\theta\theta}}{\partial \theta} + \frac{\partial \sigma_{z\theta}}{\partial z} + \frac{1}{r}(\sigma_{r\theta} + \sigma_{\theta r}) = 0, \\
&\frac{\partial \sigma_{rz}}{\partial r} + \frac{1}{r}\frac{\partial \sigma_{\theta z}}{\partial \theta} + \frac{\partial \sigma_{zz}}{\partial z} + \frac{1}{r}\sigma_{rz} = 0.
\end{aligned} \tag{3.2.5}$$

By the semi-inverse method, since for the given deformation (3.2.3), the stress components (3.2.4) depend only on the radius r, the system of equilibrium equations (3.2.5) reduces to

$$\frac{\partial \sigma_{rr}}{\partial r} + \frac{1}{r}(\sigma_{rr} - \sigma_{\theta\theta}) = 0. \tag{3.2.6}$$

Then, integration with respect to r of equation (3.2.6) together with (3.2.5) gives [128, p. 185-187]

$$\begin{aligned}
\sigma_{rr} &= -\sigma_{rr}(r_1) - \int_{r_1}^{r} \frac{\beta_1}{\mathfrak{r}} \left(\frac{a^2}{\mathfrak{r}^2} - \frac{A^2 \mathfrak{r}^2}{a} \right) d\mathfrak{r} + \int_{r_1}^{r} \frac{\beta_{-1}}{\mathfrak{r}} \left(\frac{a}{A^2 \mathfrak{r}^2} - \frac{\mathfrak{r}^2}{a^2} \right) d\mathfrak{r}, \\
\sigma_{\theta\theta} &= \sigma_{rr} - \beta_1 \left(\frac{a^2}{r^2} - \frac{A^2 r^2}{a} \right) + \beta_{-1} \left(\frac{a}{A^2 r^2} - \frac{r^2}{a^2} \right), \\
\sigma_{zz} &= \sigma_{rr} + \beta_1 \left(\frac{1}{A^2 a} - \frac{a^2}{r^2} \right) - \beta_{-1} \left(\frac{r^2}{a^2} - A^2 a \right).
\end{aligned}$$

The deformation (3.2.2) superposed on (3.2.1) is a suitable approx-

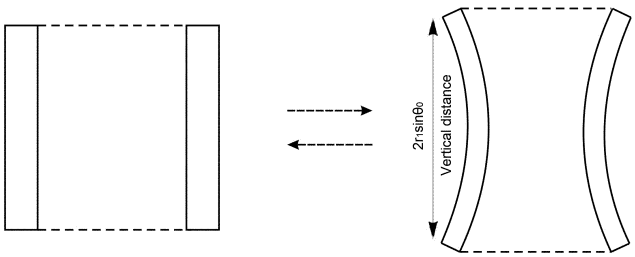

Figure 3.2.1: Schematic of finite bending (right) and straightening (left). The vertical distance between the ends of the wall may increase (closed, filled cell) or remain unchanged (open cell).

imation for the bending cell walls in a periodic structure as illustrated schematically in figure 3.2.2. In this figure, the cross-section sample of a structure with originally cuboid cells represented in figure 3.2.2 (a) deforms such that the initially vertical walls bend into circular walls, while the horizontal walls remain virtually horizontal and may extend or contract longitudinally, as shown in figure 3.2.2 (b) and (c). When the cells are filled with a compliant liquid or solid core, and the internal volume of the cells is preserved throughout the deformation, pre-stretching of the cell walls may be caused by the pressure in cell core before the walls bend. In order to study the changes in the mechanical properties of the walls in a filled cell compared to those of an empty cell, we assume that in both cases, the walls are deformed by (3.2.1) followed by (3.2.2). However, the non-zero pressure causing the pre-stretch is maintained in the filled cell, whereas in the empty cell, this pressure is removed. The same approach is employed for the analysis of other deformations in the subsequent sections.

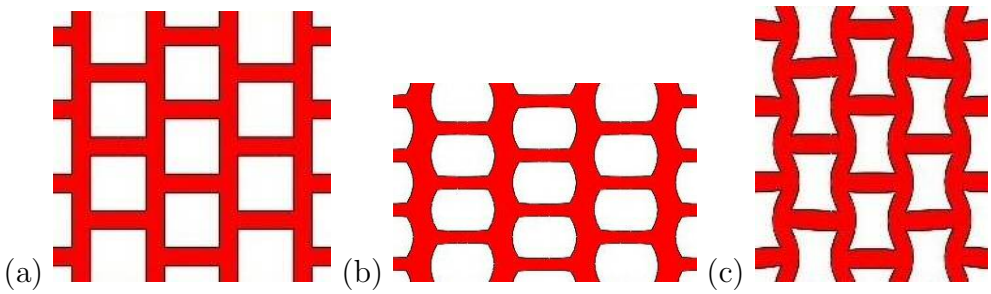

Figure 3.2.2: Sample of periodic cellular structure with cell walls that are (a) straight, (b) bent outside the cell, or (c) bent inside the cell.

3.2.1 Nonlinear elastic modulus

When the walls bend inside the cell, the distance between the ends of the deformed wall in the empty cell can remain equal to the length of the undeformed wall, i.e.,

$$Y_0 = r_1 \sin\theta_0 < r_1\theta_0 = r_1 \frac{AY_0}{\sqrt{a}}.$$

Hence $A > \sqrt{a}/r_1 > \sqrt{a}/r$, for all $r \in (r_1, r_2]$. Thus, we assume that, in the filled cell, the vertical distance between the ends of the wall will increase farther than in the empty cell, i.e., $\bar{A} > A$, where $\bar{A}$ and A are the constant parameters for the deformation (3.2.2) in the filled and the empty cell, respectively (figure 3.2.1).

For the deformed state due to (3.2.3), the radial direction is a principal direction. Assuming that this deformation is a contraction in the radial direction, i.e., $B_{rr} = a^2/r^2 < 1$, by the PC inequalities, the associated stress component is negative (radial compression). Setting $\sigma_{rr} = -p_0 \leq 0$ at the curved surface $r = r_2$, the radial stress takes the

form

$$\begin{aligned}\sigma_{rr} =& - p_0 + \int_{r_2}^{r} \frac{\beta_1}{\mathfrak{r}} \left(\frac{A^2\mathfrak{r}^2}{a} - \frac{a^2}{\mathfrak{r}^2} \right) d\mathfrak{r} \\ &+ \int_{r_2}^{r} \frac{\beta_{-1}}{\mathfrak{r}} \left(\frac{a}{A^2\mathfrak{r}^2} - \frac{\mathfrak{r}^2}{a^2} \right) d\mathfrak{r} \\ \leq& - p_0 \leq 0, \qquad r \in [r_1, r_2].\end{aligned}$$

In the above integrals, the integrands are positive due to the fact that $\beta_1 > 0$, $\beta_{-1} \leq 0$, and $A^2\mathfrak{r}^2/a > 1 > a^2/\mathfrak{r}^2$. Since $r < r_2$, both integrals are negative, and hence σ_{rr} increases as r increases. The radial stress can be written equivalently as follows

$$\begin{aligned}\sigma_{rr} =& \sigma_{rr}(r_1) + \int_{r_1}^{r} \frac{\beta_1}{\mathfrak{r}} \left(\frac{A^2\mathfrak{r}^2}{a} - \frac{a^2}{\mathfrak{r}^2} \right) d\mathfrak{r} \\ &+ \int_{r_1}^{r} \frac{\beta_{-1}}{\mathfrak{r}} \left(\frac{a}{A^2\mathfrak{r}^2} - \frac{\mathfrak{r}^2}{a^2} \right) d\mathfrak{r}, \qquad r \in [r_1, r_2].\end{aligned}$$

For the deforming wall, we define the nonlinear elastic modulus as the ratio between the Cauchy stress and the logarithmic strain [11, pp. 218-219] in the radial direction

$$\mathcal{E} = \frac{\sigma_{rr}}{\ln B_{rr}^{1/2}}. \tag{3.2.7}$$

We can define this modulus since, by Remark 2.2.1, the Cauchy stress tensor $\boldsymbol{\sigma}$ and the left Cauchy-Green tensor $\mathbf{B}$ are coaxial. Since both $\sigma_{rr} < 0$ and $1/\ln B_{rr}^{1/2} < 0$ increase as r increases, it follows that $\mathcal{E}$ decreases when r increases. To see this, we denote $f(r) = \sigma_{rr} < 0$ and $g(r) = 1/\ln B_{rr}^{1/2} < 0$, and since f and g increase with r, the first derivatives of these functions satisfy $f' > 0$ and $g' > 0$, hence $(fg)' = f'g + fg' < 0$, implying that fg decreases as r increases.

Influence of cell pressure. We first compare the values of the

modulus of elasticity (3.2.7) when the cell is empty and when the cell is filled with an incompressible fluid or solid core. Let $\boldsymbol{\sigma}'$ and $\boldsymbol{\sigma}$ represent the Cauchy stress of the wall in a filled and in an empty cell, respectively, and $\mathcal{E}'$ and $\mathcal{E}$ denote the corresponding elastic moduli. If $\sigma'_{rr}(r_2) = -p_0 < 0$ and $\sigma_{rr}(r_2) = 0$, then, at equal strains

$$\begin{aligned}\mathcal{E}' - \mathcal{E} =& -\frac{p_0}{\ln(a/r)} + \frac{1}{\ln(a/r)}\int_{r_2}^{r}\frac{\beta_1\mathfrak{r}}{a}\left(A'^2 - A^2\right)d\mathfrak{r} \\ &+ \frac{1}{\ln(a/r)}\int_{r_2}^{r}\frac{\beta_{-1}a}{\mathfrak{r}^3}\left(\frac{1}{A'^2} - \frac{1}{A^2}\right)d\mathfrak{r} \\ \geq& -\frac{p_0}{\ln(a/r)} > 0, \qquad r \in [r_1, r_2].\end{aligned}$$

In the above integrals, the integrands are positive due to the fact that $\beta_1 > 0$, $\beta_{-1} \leq 0$, and $A' > A$, and both integrals are negative since $r < r_2$. Then $-p_0 < 0$ and $\ln(a/r) < 0$ imply that the radial elastic modulus of the deformed wall is larger in the filled cell than in the empty cell, and the gap between the respective moduli increases as the magnitude of p_0 increases.

Another possible situation is when the internal volume of the filled cell begins to increase under the deformation (3.2.3) of the cell walls, and the walls become free from the pressure due to the incompressible inclusion, which now occupies less than the total internal volume of the deformed cell. In this cell, the vertical distance between the ends of the wall may increase farther than in the filled cell with fixed internal volume, and we set $A'' = \sqrt{A'^2 + \delta^2}$ as the constant parameter for the deformation (3.2.2), where $\delta^2 > 0$.

Let $\boldsymbol{\sigma}'$ and $\boldsymbol{\sigma}''$ denote the Cauchy stress of the wall in a filled cell with fixed and increased internal volume, respectively, and $\mathcal{E}'$ and $\mathcal{E}''$ be the respective elastic moduli. If $\sigma'_{rr}(r_2) = -p_0 < 0$ and $\sigma''_{rr}(r_2) = 0$,

then, at equal strains

$$\begin{aligned}\mathcal{E}' - \mathcal{E}'' =& -\frac{p_0}{\ln(a/r)} + \frac{1}{\ln(a/r)}\int_{r_2}^{r}\frac{\beta_1\mathfrak{r}}{a}\left(A'^2 - A''^2\right)d\mathfrak{r} \\ &+ \frac{1}{\ln(a/r)}\int_{r_2}^{r}\frac{\beta_{-1}a}{\mathfrak{r}^3}\left(\frac{1}{A'^2} - \frac{1}{A''^2}\right)d\mathfrak{r} \\ =& -\frac{p_0}{\ln(a/r)} - \frac{\delta^2}{\ln(a/r)}\int_{r_2}^{r}\frac{\beta_1\mathfrak{r}}{a}d\mathfrak{r} \\ &+ \frac{\delta^2}{A'^2\left(A'^2+\delta^2\right)\ln(a/r)}\int_{r_2}^{r}\frac{\beta_{-1}a}{\mathfrak{r}^3}d\mathfrak{r}, \\ \leq& -\frac{p_0}{\ln(a/r)} > 0, \qquad r \in [r_1, r_2].\end{aligned}$$

In the above integrals, $\beta_1 > 0$, $\beta_{-1} \leq 0$, and $r < r_2$. Then there exists $\delta_0^2 > 0$, such that

$$\mathcal{E}' - \mathcal{E}'' > 0, \qquad \forall\delta^2 \in (0, \delta_0^2).$$

Finally, comparing the elastic moduli in the cell with increasing internal volume and in the empty cell, we obtain

$$\begin{aligned}\mathcal{E}'' - \mathcal{E} =& \frac{1}{\ln(a/r)}\int_{r_2}^{r}\frac{\beta_1\mathfrak{r}}{a}\left(A''^2 - A^2\right)d\mathfrak{r} \\ &+ \frac{1}{\ln(a/r)}\int_{r_2}^{r}\frac{\beta_{-1}a}{\mathfrak{r}^3}\left(\frac{1}{A''^2} - \frac{1}{A^2}\right)d\mathfrak{r} \\ &> 0, \qquad r \in [r_1, r_2].\end{aligned}$$

In the above integrals, the integrands are positive due to the fact that $\beta_1 > 0$, $\beta_{-1} \leq 0$, and $A'' > A$, and both integrals are negative since $r < r_2$. Then $\ln(a/r) < 0$ implies that the radial elastic modulus of the deformed wall is larger in the filled cell with increasing internal volume and no internal pressure than in the empty cell.

We conclude that, for sufficiently small δ^2,

$$\mathcal{E}' > \mathcal{E}'' > \mathcal{E},$$

i.e., the radial elastic modulus of the deforming wall is larger in the filled cell with fixed internal volume (and non-zero cell pressure) than when the internal volume increases (and there is no internal pressure), and smaller in the empty cell.

Influence of wall thickness. Next, we compare the behaviour of two walls of different thickness subject to the deformation (3.2.3). Taking the original wall as the 'thin' wall, we assume that the 'thicker' wall occupies the reference domain $[X_1, X_2'] \times [-Y_0, Y_0] \times [-Z_0, Z_0]$, where $X_2' > X_2$, and denote by $\boldsymbol{\sigma}'$ the Cauchy stress in this wall, and by $\mathcal{E}'$ the associated elastic modulus (3.2.7). Then setting $\sigma_{rr}'(r_2') = \sigma_{rr}(r_2) = -p_0 \leq 0$, we obtain

$$\begin{aligned}\mathcal{E}' - \mathcal{E} =& \frac{1}{\ln(a/r)} \int_{r_2'}^{r_2} \frac{\beta_1}{\mathfrak{r}} \left(\frac{A^2\mathfrak{r}^2}{a} - \frac{a^2}{\mathfrak{r}^2} \right) d\mathfrak{r} \\ &+ \frac{1}{\ln(a/r)} \int_{r_2'}^{r_2} \frac{\beta_{-1}}{\mathfrak{r}} \left(\frac{a}{A^2\mathfrak{r}^2} - \frac{\mathfrak{r}^2}{a^2} \right) d\mathfrak{r} \\ &> 0, \qquad r \in [r_1, r_2].\end{aligned}$$

In the above integrals, the integrands are positive due to the fact that $\beta_1 > 0$, $\beta_{-1} \leq 0$, and $A^2\mathfrak{r}^2/a > 1 > a^2/\mathfrak{r}^2$, and both integrals are negative since $r_2 < r_2'$. Then $\ln(a/r) < 0$ implies that the radial elastic modulus increases as the thickness of the cell wall increases.

Multi-layer wall. We also consider the case when a second wall is "attached" to the first wall in the sense that the relative radial displacement across the common interface is equal to zero, and both walls deform by (3.2.3), while each wall may made from a different

hyperelastic material. Specifically, let the second wall occupy the domain $[X_2, X_2'] \times [-Y_0, Y_0] \times [-Z_0, Z_0]$ in the reference state, and $[r_2, r_2'] \times [-\theta_0, \theta_0] \times [-z_0, z_0]$ in the deformed state, where $X_2' > 0$ and $r_2' > 0$ are constants (figure 3.2.3).

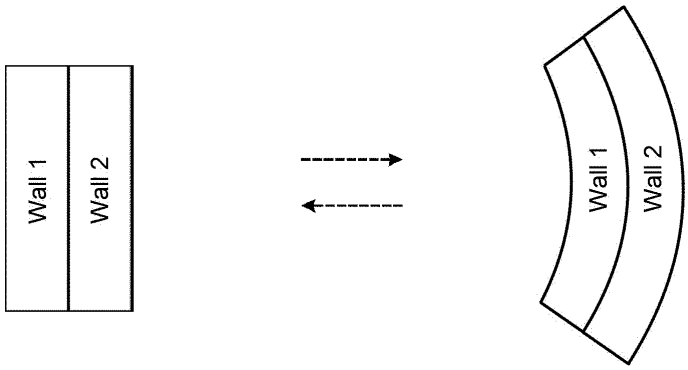

Figure 3.2.3: Schematic of elastic bending of a two-layer wall, where each layer may contain a different hyperelastic material.

We verify how the stiffness of the first wall is modified by the presence of the second wall. We denote by $\boldsymbol{\sigma}'$ the Cauchy stress for either walls, and by $\mathcal{E}'$ the associated radial elastic modulus (3.2.7). When the radial strain satisfies $B_{rr} < 1$ for both walls, setting $\sigma_{rr}'(r_2') = -p_0 \leq 0$, the radial stress of the second wall takes the form

$$\begin{aligned}\sigma_{rr}'(r) &= -p_0 + \int_{r_2'}^{r} \frac{\beta_1'}{\mathfrak{r}} \left(\frac{A^2\mathfrak{r}^2}{a} - \frac{a^2}{\mathfrak{r}^2} \right) d\mathfrak{r} + \int_{r_2'}^{r} \frac{\beta_{-1}'}{\mathfrak{r}} \left(\frac{a}{A^2\mathfrak{r}^2} - \frac{\mathfrak{r}^2}{a^2} \right) d\mathfrak{r} \\ &\leq -p_0, \qquad r \in [r_2, r_2'],\end{aligned}$$

where $\beta_1' > 0$ and $\beta_{-1}' \leq 0$ are the material responses for this wall.

For the first wall, the radial stress is

$$\begin{aligned}\sigma_{rr}'(r) =& \sigma_{rr}'(r_2) + \int_{r_2}^{r} \frac{\beta_1}{\mathfrak{r}} \left(\frac{A^2\mathfrak{r}^2}{a} - \frac{a^2}{\mathfrak{r}^2} \right) d\mathfrak{r} \\ &+ \int_{r_2}^{r} \frac{\beta_{-1}}{\mathfrak{r}} \left(\frac{a}{A^2\mathfrak{r}^2} - \frac{\mathfrak{r}^2}{a^2} \right) d\mathfrak{r} \\ \leq& \sigma_{rr}'(r_2), \qquad r \in [r_1, r_2],\end{aligned}$$

where $\beta_1 > 0$ and $\beta_{-1} \leq 0$ are the corresponding material responses.

If $\boldsymbol{\sigma}$ represents the Cauchy stress of the original wall when no other wall is attached, such that $\sigma_{rr}(r_2) = -p_0$, then

$$\begin{aligned}\mathcal{E}' - \mathcal{E} =& \frac{\sigma'_{rr}(r_2) + p_0}{\ln B_{rr}^{1/2}} \\ =& \frac{1}{\ln(a/r)} \int_{r'_2}^{r_2} \frac{\beta'_1}{\mathfrak{r}} \left(\frac{A^2\mathfrak{r}^2}{a} - \frac{a^2}{\mathfrak{r}^2} \right) d\mathfrak{r} \\ &+ \frac{1}{\ln(a/r)} \int_{r'_2}^{r_2} \frac{\beta'_{-1}}{\mathfrak{r}} \left(\frac{a}{A^2\mathfrak{r}^2} - \frac{\mathfrak{r}^2}{a^2} \right) d\mathfrak{r} \\ &> 0, \qquad r \in [r_1, r_2].\end{aligned}$$

In the above integrals, the integrands are positive due to the fact that $\beta'_1 > 0$, $\beta'_{-1} \leq 0$, and $A^2r^2/a > 1 > a^2/r^2$, and both integrals are negative since $r_2 < r'_2$. Then $\ln(a/r) < 0$ implies that the radial elastic modulus of the first wall is larger when a second wall is attached to it in the direction of its decreasing curvature. Since the magnitude of $\sigma'_{rr}(r_2)$ relative to $-p_0$ increases when the thickness of the second wall increases, the elastic modulus of the first wall increases with the thickness of the attached wall.

This analysis extends to the case with multiply layered cell walls. In particular, when a third wall, which may be made from a different material occupying the reference domain $[X'_2, X''_2] \times [-Y_0, Y_0] \times [-Z_0, Z_0]$, where $X''_2 > 0$ is constant, is further attached to the second wall in the direction of its decreasing curvature, and the three walls deform simultaneously by (3.2.3), then the stiffness of both the first and the second (middle) wall is enhanced by the contact with the adjacent walls. For sandwich structures in bending, this implies that the stiffness of the middle layer will be enhanced in part by the contact conditions with the adjacent layers.

Influence of number of walls when the total material volume is fixed. We further examine the mean elastic modulus for two thin walls which deform separately by (3.2.3) with that for a single thick wall made from the same material and subject to the same deformation, when the total volume of the two thin walls is equal to that of the thick wall. We take the two thin walls equal in size, with a thin wall $[X_1, X_2] \times [-Y_0, Y_0] \times [-Z_0, Z_0]$ deforming into $[r_1, r_2] \times [-\theta_0, \theta_0] \times [-z_0, z_0]$, and the thick wall $[X_1, X_2'] \times [-Y_0, Y_0] \times [-Z_0, Z_0]$ deforming into $[r_1, r_2'] \times [-\theta_0, \theta_0] \times [-z_0, z_0]$, where $X_2' - X_1 = 2(X_2 - X_1)$, implying that $r_2'^2 - r_1^2 = 2\left(r_2^2 - r_1^2\right)$ (figure 3.2.4).

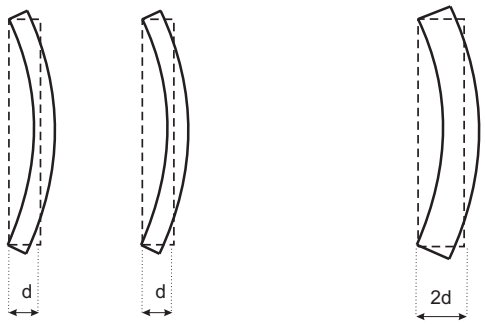

Figure 3.2.4: Schematic of elastic bending of two thin blocks (left) and one thick block (right).

In the radial direction, we define the mean elastic modulus for the thin walls as

$$\bar{\mathcal{E}} = \frac{2}{r_2^2 - r_1^2} \int_{r_1^2}^{r_2^2} \mathcal{E} r dr,$$

and for the thick wall as

$$\bar{\mathcal{E}}' = \frac{2}{r_2'^2 - r_1^2} \int_{r_1^2}^{r_2'^2} \mathcal{E} r dr,$$

where $\mathcal{E}$ is the radial elastic modulus given by (3.2.7). Note that the mean elastic modulus for the two equal thin walls is the same as for a single thin wall.

If the corresponding stresses satisfy $\sigma_{rr}(r_2) = -p_0 \leq 0$ and $\sigma'_{rr}(r'_2) = -p'_0 \leq 0$, respectively, such that $\sigma_{rr}(r_1) = \sigma'_{rr}(r_1)$, we obtain

$$\begin{aligned}
\bar{\mathcal{E}} - \bar{\mathcal{E}}' =& \frac{2}{r_2^2 - r_1^2} \int_{r_1^2}^{r_2^2} \mathcal{E} r dr - \frac{2}{r_2'^2 - r_1^2} \int_{r_1^2}^{r_2'^2} \mathcal{E} r dr \\
=& \frac{2}{r_2^2 - r_1^2} \int_{r_1^2}^{r_2^2} \mathcal{E} r dr - \frac{2}{r_2'^2 - r_1^2} \int_{r_1^2}^{r_2^2} \mathcal{E} r dr - \frac{2}{r_2'^2 - r_1^2} \int_{r_2^2}^{r_2'^2} \mathcal{E} r dr \\
=& \frac{2}{r_2^2 - r_1^2} \int_{r_1^2}^{r_2^2} \mathcal{E} r dr - \frac{1}{r_2^2 - r_1^2} \int_{r_1^2}^{r_2^2} \mathcal{E} r dr - \frac{1}{r_2^2 - r_1^2} \int_{r_2^2}^{r_2'^2} \mathcal{E} r dr \\
=& \frac{1}{2(X_2 - X_1)} \int_{X_1}^{X_2} \mathcal{E} dX - \frac{1}{2(X_2 - X_1)} \int_{X_2}^{X_2'} \mathcal{E} dX \\
=& \frac{1}{2(X_2 - X_1)} \int_{X_1}^{X_2} \left[\mathcal{E}(X) - \mathcal{E}(X_2 + X - X_1) \right] dX \\
& > 0.
\end{aligned}$$

The above inequality holds since $\mathcal{E}$ defined by (3.2.7) decreases as r increases and r increases as X increases, hence $\mathcal{E}$ decreases as X increases. Therefore the mean elastic modulus of the thin walls is greater than the mean modulus of the thick wall.

Since the mean elastic modulus for n equal thin walls is the same as for a single thin wall, the calculations remain unchanged when the two thin walls $[X_1, X_2] \times [-Y_0, Y_0] \times [-Z_0, Z_0]$ are replaced by four equal walls $[X_1, X_2] \times [-Y_0/2, Y_0/2] \times [-Z_0, Z_0]$.

The analysis extends to the case with $n > 2$ equal cell walls. For example, if three equal thin walls having reference domains $[X_1, X_2] \times [-Y_0, Y_0] \times [-Z_0, Z_0]$ are compared with two equal thicker walls with reference domains $[X_1, X'_2] \times [-Y_0, Y_0] \times [-Z_0, Z_0]$, where $2(X'_2 - X_1) =$

$3(X_2 - X_1)$, which implies that $2\left(r_2'^2 - r_1^2\right) = 3\left(r_2^2 - r_1^2\right)$, then

$$\begin{aligned}
\bar{\mathcal{E}} - \bar{\mathcal{E}}' =& \frac{2}{r_2^2 - r_1^2}\int_{r_1^2}^{r_2^2} \mathcal{E} r dr - \frac{2}{r_2'^2 - r_1^2}\int_{r_1^2}^{r_2'^2} \mathcal{E} r dr \\
=& \frac{2}{r_2^2 - r_1^2}\int_{r_1^2}^{r_2^2} \mathcal{E} r dr - \frac{2}{r_2'^2 - r_1^2}\int_{r_1^2}^{r_2^2} \mathcal{E} r dr - \frac{2}{r_2'^2 - r_1^2}\int_{r_2^2}^{r_2'^2} \mathcal{E} r dr \\
=& \frac{6}{3(r_2^2 - r_1^2)}\int_{r_1^2}^{r_2^2} \mathcal{E} r dr - \frac{4}{3(r_2^2 - r_1^2)}\int_{r_1^2}^{r_2^2} \mathcal{E} r dr \\
& - \frac{4}{3(r_2^2 - r_1^2)}\int_{r_2^2}^{r_2'^2} \mathcal{E} r dr \\
=& \frac{1}{3(X_2 - X_1)}\int_{X_1}^{X_2} \mathcal{E} dX - \frac{2}{3(X_2 - X_1)}\int_{X_2}^{X_2'} \mathcal{E} dX \\
=& \frac{1}{3(X_2 - X_1)}\int_{X_1}^{X_2} \left[\mathcal{E}(X) - \mathcal{E}(X_2 + (X - X_1)/2)\right] dX \\
& > 0.
\end{aligned}$$

It follows that the mean elastic modulus increases as the number of equal thin walls increases when the total material volume remains unchanged. Similar results are obtained when $B_{rr} > 1$ (radial extension. In this case, by the PC inequalities, the associated stress component is positive, i.e. $\sigma_{rr} > 0$ (radial tension).

3.2.2 Optimisation problem

Since the radial elastic modulus (3.2.7) increases monotonically as the thickness of the cell wall increases, we employ this modulus to determine the minimum cell wall thickness for the deformation (3.2.3). Assuming $B_{rr} < 1$, we formulate the following optimisation problem [41]

$$\text{find } r_1 = \sup\ V, \qquad V = \{r < r_2 \,|\, \mathcal{E}(r) \geq C\}\,,$$

where $C > 0$ is a given target value.

The goal is to find the range of values for the internal radius r_1 under which the above optimisation problem is well posed. For this problem, the existence of a solution is guaranteed since the range of admissible values V is a bounded non-empty set.

Next, we employ the radial elastic modulus to find the minimum applied pressure for the deformation (3.2.3), and formulate the following constrained optimisation problem

$$\text{find } p_0 = \inf\ V, \qquad V = \{p > 0 \mid \mathcal{E}(r) \geq C\}\,.$$

This problem also has a solution if the set of admissible values V is non-empty. Since $\mathcal{E}(r)$ increases monotonically as p_0 increases, there exist $p_0 > 0$, such that $\mathcal{E}(r) \geq C$ for all $r \in [r_1, r_2]$, i.e., the set V is non-empty.

Similarly, the radial elastic modulus can be useful in finding the minimum number of walls for the deformation (3.2.3) when the total volume of material is fixed

$$\text{find } n_0 = \min\ \left\{ n \in \mathbb{N} \;\middle|\; \frac{1}{n(r_2^2 - r_1^2)} \int_{r_1^2}^{r_1^2 + n(r_2^2 - r_1^2)} \mathcal{E}(r)dr \geq C \right\}.$$

Since, for a fixed volume of elastic material, the mean elastic modulus increases as n increases, the set of feasible values is non-empty, hence this optimisation problem has a solution.

We conclude that constraints involving a bound on the radial elastic modulus (3.2.7) guarantee a feasible solution to the problem of finding the optimal wall thickness, surface pressure, or number of walls when the total volume of solid material remains fixed under the deformation (3.2.3). The epigraph for the corresponding optimisation function is

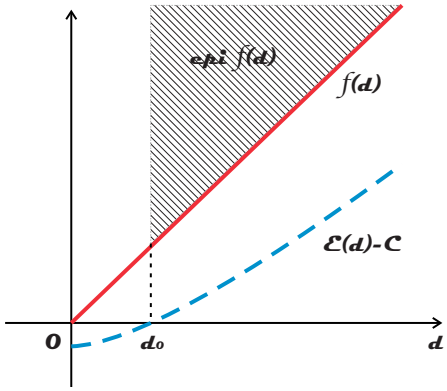

Figure 3.2.5: Epigraph of function $f : V = \{d > 0 \mid \mathcal{E}(d) \geq C\} \to \mathbb{R},\ f(d) = d$.

illustrated graphically in figure 3.2.5.

3.3 Straightening of curved walls

A cell wall in the shape of an annular wedge with reference geometry $(R, \Theta, Z) \in [R_1, R_2] \times [-\Theta_0, \Theta_0] \times [-Z_0, Z_0]$, where R_1, R_2, Θ_0, and Z_0 are positive constants, is first deformed by the uniform stretch [128, pp. 188-189]

$$\tilde{R} = \sqrt{a}R, \qquad \tilde{\Theta} = \Theta, \qquad \tilde{Z} = \frac{Z}{a}, \tag{3.3.1}$$

where $(\tilde{R}, \tilde{\Theta}, \tilde{Z})$ and (R, Θ, Z) are the cylindrical polar coordinates for the deformed and the reference configuration, respectively, and a is a positive constant. For the deformation (3.3.1), the deformation gradient satisfies

$$\begin{bmatrix} d\tilde{R} \\ \tilde{R}d\tilde{\Theta} \\ d\tilde{Z} \end{bmatrix} = \mathbf{F} \begin{bmatrix} dR \\ Rd\Theta \\ dZ \end{bmatrix}$$

and is equal to

$$\mathbf{F} = \begin{bmatrix} \partial\tilde{R}/\partial R & 0 & 0 \\ 0 & (\tilde{R}/R)\partial\tilde{\Theta}/\partial\Theta & 0 \\ 0 & 0 & \partial\tilde{Z}/\partial Z \end{bmatrix} = \begin{bmatrix} \sqrt{a} & 0 & 0 \\ 0 & \sqrt{a} & 0 \\ 0 & 0 & 1/a \end{bmatrix}.$$

The associated left Cauchy-Green tensor and its inverse are respectively

$$\mathbf{B} = \mathbf{F}\mathbf{F}^T = \begin{bmatrix} a & 0 & 0 \\ 0 & a & 0 \\ 0 & 0 & 1/a^2 \end{bmatrix},$$

$$\mathbf{B}^{-1} = \begin{bmatrix} 1/a & 0 & 0 \\ 0 & 1/a & 0 \\ 0 & 0 & a^2 \end{bmatrix}.$$

By the representation (2.2.3), the non-zero components of the corresponding Cauchy stress tensor take the form [128, p. 190]

$$\sigma^{(0)}_{\tilde{R}\tilde{R}} = \sigma^{(0)}_{\tilde{\Theta}\tilde{\Theta}} = -p + \beta_1 a + \frac{\beta_{-1}}{a}, \qquad \sigma^{(0)}_{\tilde{Z}\tilde{Z}} = -p + \frac{\beta_1}{a^2} + \beta_{-1}a^2,$$

or equivalently, by setting $-p_0 := -p + \beta_1 a + \beta_{-1}/a$

$$\sigma^{(0)}_{\tilde{R}\tilde{R}} = \sigma^{(0)}_{\tilde{\Theta}\tilde{\Theta}} = -p_0, \qquad \sigma^{(0)}_{\tilde{Z}\tilde{Z}} = -p_0 - \beta_1 a\left(1 - \frac{1}{a^3}\right) + \frac{\beta_{-1}}{a}\left(a^3 - 1\right).$$

Next, the deformed wall is "straightened" into a rectangular block by the deformation [128, pp. 188-189]

$$x = \frac{A^2}{2}\tilde{R}^2, \qquad y = \frac{\tilde{\Theta}}{A}, \qquad z = \frac{\tilde{Z}}{A}, \tag{3.3.2}$$

where $(x, y, z) \in [x_1, x_2] \times [-y_0, y_0] \times [-z_0, z_0]$ are the Cartesian coordinates for the current configuration, and x_1, x_2, y_0, z_0, and A are positive constants (figure 3.3.1).

The combined deformation given by the successive deformations (3.3.1) and (3.3.2) is defined by [128, pp. 188-189]

$$x = \frac{A^2 a}{2}R^2, \qquad y = \frac{\Theta}{A}, \qquad z = \frac{Z}{Aa}. \tag{3.3.3}$$

For this deformation, the gradient satisfies

$$\begin{bmatrix} dx \\ dy \\ dz \end{bmatrix} = \mathbf{F} \begin{bmatrix} dR \\ Rd\Theta \\ dZ \end{bmatrix},$$

hence, in terms of the current Cartesian coordinates (x, y, z), the deformation gradient is equal to

$$\begin{aligned} \mathbf{F} &= \begin{bmatrix} \partial x/\partial R & 0 & 0 \\ 0 & (1/R)\partial y/\partial\Theta & 0 \\ 0 & 0 & \partial z/\partial Z \end{bmatrix} \\ &= \begin{bmatrix} A\sqrt{2ax} & 0 & 0 \\ 0 & \sqrt{a/(2x)} & 0 \\ 0 & 0 & 1/(Aa) \end{bmatrix}. \end{aligned}$$

The corresponding left Cauchy-Green tensor and its inverse are re-

spectively

$$\mathbf{B} = \begin{bmatrix} 2A^2ax & 0 & 0 \\ 0 & a/(2x) & 0 \\ 0 & 0 & 1/(A^2a^2) \end{bmatrix},$$
$$\mathbf{B}^{-1} = \begin{bmatrix} 1/\left(2A^2ax\right) & 0 & 0 \\ 0 & 2x/a & 0 \\ 0 & 0 & A^2a^2 \end{bmatrix}.$$

By (2.2.3), the non-zero components of the associated Cauchy stress tensor take the form

$$\begin{aligned} \sigma_{xx} &= -p + \beta_1 2A^2ax + \beta_{-1}\frac{1}{2A^2ax}, \\ \sigma_{yy} &= -p + \beta_1\frac{a}{2x} + \beta_{-1}\frac{2x}{a}, \\ \sigma_{zz} &= -p + \beta_1\frac{1}{A^2a^2} + \beta_{-1}A^2a^2. \end{aligned} \tag{3.3.4}$$

In the absence of body forces, by the equilibrium equation (2.3.1), the non-zero components of the Cauchy stress satisfy

$$\begin{aligned} \frac{\partial\sigma_{xx}}{\partial x} + \frac{\partial\sigma_{yx}}{\partial y} + \frac{\partial\sigma_{zx}}{\partial z} &= 0, \\ \frac{\partial\sigma_{yx}}{\partial x} + \frac{\partial\sigma_{yy}}{\partial y} + \frac{\partial\sigma_{zy}}{\partial z} &= 0, \\ \frac{\partial\sigma_{zx}}{\partial x} + \frac{\partial\sigma_{zy}}{\partial y} + \frac{\partial\sigma_{zz}}{\partial z} &= 0. \end{aligned} \tag{3.3.5}$$

By the semi-inverse method, since for the deformation (3.3.3), the stress components (3.3.4) depend only on x , the system of equations (3.3.5) simplifies to

$$\frac{\partial\sigma_{xx}}{\partial x} = 0, \tag{3.3.6}$$

and integration with respect to x of equation (3.3.6) together with

(3.3.4) gives [128, p. 189]

$$\begin{aligned}
\sigma_{xx} &= -p_0, \\
\sigma_{yy} &= \sigma_{xx} + \beta_1 \left(\frac{a}{2x} - 2A^2 ax \right) + \beta_{-1} \left(\frac{2x}{a} - \frac{1}{2A^2 ax} \right), \\
\sigma_{zz} &= \sigma_{xx} + \beta_1 \left(\frac{1}{A^2 a^2} - 2A^2 ax \right) + \beta_{-1} \left(A^2 a^2 - \frac{1}{2A^2 ax} \right).
\end{aligned}$$

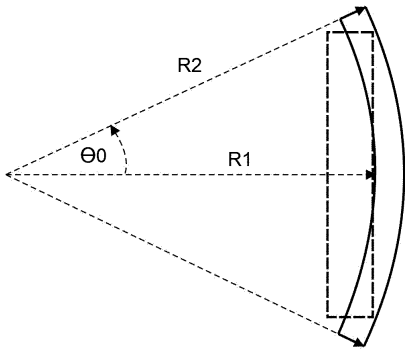

Figure 3.3.1: Schematic of straightening of a curved wall.

3.3.1 Nonlinear elastic modulus

For the deformation (3.3.3), the x-direction is a principal direction. Assuming that this deformation is a contraction in the x-direction, i.e., $B_{xx} = 2A^2 ax < 1$, by the PC inequalities, the associated stress component is compressive, i.e.

$$\sigma_{xx} = -p_0 \leq 0, \qquad x \in [x_1, x_2].$$

Since p_0 is constant, the stress component σ_{xx} is constant.

For the deforming wall, we define the nonlinear elastic modulus as the ratio between the Cauchy stress and the logarithmic strain [11, pp. 218-219] in the x-direction

$$\mathcal{E} = \frac{\sigma_{xx}}{\ln B_{xx}^{1/2}}. \tag{3.3.7}$$

Note that, since $\sigma_{xx} < 0$ is constant and $1/\ln B_{xx}^{1/2} < 0$ decreases as x increases, it follows that $\mathcal{E}$ increases as x increases.

Influence of internal pressure. We compare the values of the modulus of elasticity (3.3.7) when the cell is empty and when the cell is filled with an incompressible core. Let $\boldsymbol{\sigma}'$ and $\boldsymbol{\sigma}$ denote the Cauchy stress for the filled cell and the empty cell, respectively, and $\mathcal{E}'$ and $\mathcal{E}$ be the corresponding elastic moduli. Setting $\sigma'_{xx} = -p_0 < 0$ and $\sigma_{xx} = 0$, we obtain

$$\mathcal{E}' - \mathcal{E} = -\frac{p_0}{\ln(A\sqrt{2ax})} > 0, \qquad x \in [x_1, x_2].$$

Hence the elastic modulus in the transverse direction of the deformed wall is greater in the filled cell than in the empty cell, and the gap between the two moduli increases as the magnitude of $-p_0$ increases.

Influence of wall thickness. Since σ_{xx} is constant, if $-p_0 < 0$, then the elastic modulus (3.3.7) is a monotonic function of x and increases as the thickness of the wall increases.

Influence of number of walls when the total material volume is fixed. We also compare the mean elastic modulus of two thin walls deforming separately by (3.3.3) with that of a single thick wall made from the same material and subject to the same deformation, when the total volume of the two thin walls is equal to that of the thick wall. We take the two thin walls equal in size, with a thin wall $[R_1, R_2] \times [-\Theta_0, \Theta_0] \times [-Z_0, Z_0]$ deforming into $[x_1, x_2] \times [-y_0, y_0] \times [-z_0, z_0]$, and the thick wall $[R'_1, R_2] \times [-\Theta_0, \Theta_0] \times [-Z_0, Z_0]$ deforming into $[x'_1, x_2] \times [-y_0, y_0] \times [-z_0, z_0]$, where $R_2^2 - R_1'^2 = 2(R_2^2 - R_1^2)$, hence $x_2 - x'_1 = 2(x_2 - x_1)$.

In the x-direction, we define the mean elastic modulus for the thin

walls as

$$\bar{\mathcal{E}} = \frac{1}{x_2 - x_1} \int_{x_1}^{x_2} \mathcal{E} dx,$$

and for the thick wall as

$$\bar{\mathcal{E}}' = \frac{1}{x_2 - x_1'} \int_{x_1'}^{x_2} \mathcal{E} dx,$$

where $\mathcal{E}$ is the elastic modulus given by (3.3.7). Note that the mean elastic modulus for the two equal thin walls is the same as for a single thin wall.

If the associated stresses satisfy $\sigma_{xx} = \sigma'_{xx} = -p_0 \leq 0$, then

$$\begin{aligned}
\bar{\mathcal{E}} - \bar{\mathcal{E}}' =& \frac{1}{x_2 - x_1} \int_{x_1}^{x_2} \mathcal{E} dx - \frac{1}{x_2 - x_1'} \int_{x_1'}^{x_2} \mathcal{E} dx \\
=& \frac{1}{x_2 - x_1} \int_{x_1}^{x_2} \mathcal{E} dx - \frac{1}{x_2 - x_1'} \int_{x_1'}^{x_1} \mathcal{E} dx - \frac{1}{x_2 - x_1'} \int_{x_1}^{x_2} \mathcal{E} dx \\
=& \frac{1}{2(x_2 - x_1)} \int_{x_1}^{x_2} 2\mathcal{E} dx - \frac{1}{2(x_2 - x_1)} \int_{x_1'}^{x_1} \mathcal{E} dx \\
& - \frac{1}{2(x_2 - x_1)} \int_{x_1}^{x_2} \mathcal{E} dx \\
=& \frac{1}{2(x_2 - x_1)} \int_{x_1}^{x_2} \left[\mathcal{E}(x) - \mathcal{E}(x_1 + x - x_2) \right] dx \\
& > 0.
\end{aligned}$$

The above inequality holds since $\mathcal{E}$ defined by (3.3.7) is an increasing function of x. Hence the mean elastic modulus of the thin walls is greater than the mean modulus of the thick wall.

Since the mean elastic modulus for n equal thin walls is the same as for a single thin wall, the calculations remain unchanged if the two thin walls $[R_1, R_2] \times [-\Theta_0, \Theta_0] \times [-Z_0, Z_0]$ are replaced by four equal walls $[R_1, R_2] \times [-\Theta_0/2, \Theta_0/2] \times [-Z_0, Z_0]$.

The analysis extends to the case with $n > 2$ equal cell walls.

For example, when three equal thin walls having reference domains $[R_1, R_2] \times [-\Theta_0, \Theta_0] \times [-Z_0, Z_0]$ are compared with two equal thicker walls with reference domains $[R_1', R_2] \times [-\Theta_0, \Theta_0] \times [-Z_0, Z_0]$, where $2(R_2^2 - R_1'^2) = 3(R_2^2 - R_1^2)$, hence $2(x_2 - x_1') = 3(x_2 - x_1)$,

$$\begin{aligned}
\bar{\mathcal{E}} - \bar{\mathcal{E}}' =& \frac{1}{x_2 - x_1} \int_{x_1}^{x_2} \mathcal{E} dx - \frac{1}{x_2 - x_1'} \int_{x_1'}^{x_2} \mathcal{E} dx \\
=& \frac{1}{x_2 - x_1} \int_{x_1}^{x_2} \mathcal{E} dx - \frac{1}{x_2 - x_1'} \int_{x_1'}^{x_1} 2\mathcal{E} dx - \frac{1}{x_2 - x_1'} \int_{x_1}^{x_2} 2\mathcal{E} dx \\
=& \frac{1}{3(x_2 - x_1)} \int_{x_1}^{x_2} 3\mathcal{E} dx - \frac{1}{3(x_2 - x_1)} \int_{x_1'}^{x_1} 2\mathcal{E} dx \\
& - \frac{1}{3(x_2 - x_1)} \int_{x_1}^{x_2} 2\mathcal{E} dx \\
=& \frac{1}{3(x_2 - x_1)} \int_{x_1}^{x_2} \left[\mathcal{E}(x) - \mathcal{E}(x_1 + (x - x_2)/2) \right] dx \\
& > 0.
\end{aligned}$$

Thus the mean elastic modulus increases as the number of equal thin walls increases if the total material volume remains unchanged. Similar results can be obtained when $B_{xx} > 1$. In this case, by the PC inequalities, $\sigma_{xx} > 0$.

3.3.2 Optimisation problem

Since the nonlinear elastic modulus defined by (3.3.7) increases with the wall thickness, we can employ this modulus to find the minimum wall thickness for the deformation (3.3.3). When $B_{xx} = 2A^2 ax < 1$, we formulate the following optimisation problem [41]

$$\text{find } x_2 = \inf\ V, \qquad V = \{x > x_1 \mid \mathcal{E}(x) \geq C\},$$

where $C > 0$ is given. Since

$$\mathcal{E}(x) = -\frac{p_0}{\ln(A\sqrt{2ax})} \geq C, \quad \text{for all} \quad x \geq \frac{e^{-2C/p_0}}{2A^2a},$$

we deduce that V is bounded and non-empty, hence the optimisation problem has a solution.

If $B_{xx} > 1$, then the optimisation problem is

$$\text{find } x_1 = \sup\ V, \qquad V = \{x < x_2 \mid \mathcal{E}(x) \geq C\},$$

where $C > 0$ is given. In this case, since

$$\mathcal{E}(x) = -\frac{p_0}{\ln(A\sqrt{2ax})} \geq C, \quad \text{for all} \quad x \leq \frac{e^{-2p_0/C}}{2A^2a},$$

V is bounded and non-empty, hence the optimisation problem has a solution.

The problem of finding the minimum surface pressure or number of walls when the total volume of elastic material is fixed can be formulated analogously.

Therefore the constraint represented by a bound on the elastic modulus (3.3.7) can be employed to determine the minimum wall thickness, surface pressure, or number of walls when the total volume of solid material remains fixed under the deformation (3.3.3).

3.4 Torsion of circular tubes and cylinders

A circular cylindrical tube (or annular wedge) occupying the domain $(R, \Theta, Z) \in [R_1, R_2] \times [-\Theta_0, \Theta_0] \times [-Z_0, Z_0]$, where R_1, R_2, Θ_0, and Z_0 are positive constants, is first deformed by the uniform stretch (3.3.1). The deformed tube is then further subjected to the simple

torsion [128, pp. 189-191]

$$r = \tilde{R}, \qquad \theta = \tilde{\Theta} + \tau \tilde{Z}, \qquad z = \tilde{Z}, \tag{3.4.1}$$

where (r, θ, z) and $(\tilde{R}, \tilde{\Theta}, \tilde{Z})$ are the cylindrical polar coordinates for the current and the pre-deformed tube, respectively, and τ is a positive constant (figure 3.4.1). Note that, during the deformation (3.4.1), the circular plane section at $Z = 0$ remains fixed, and each circular plane section normal to the central axis remains plane and rotates by an angle τZ. Hence this deformation can also be regarded as a shear deformation in the transverse direction Θ. The combined deformation given by the successive deformations (3.3.1) and (3.4.1) takes the form [86], [128, pp. 188-191]

$$r = \sqrt{a} R, \qquad \theta = \Theta + \frac{\tau}{a} Z, \qquad z = \frac{Z}{a}. \tag{3.4.2}$$

For this deformation, the gradient satisfies

$$\begin{bmatrix} dr \\ r d\theta \\ dz \end{bmatrix} = \mathbf{F} \begin{bmatrix} dR \\ R d\Theta \\ dZ \end{bmatrix},$$

hence the deformation gradient in terms of the current cylindrical polar coordinates (r, θ, z) is equal to

$$\mathbf{F} = \begin{bmatrix} \partial r/\partial R & 0 & 0 \\ 0 & (r/R)\partial\theta/\partial\Theta & r\partial\theta/\partial Z \\ 0 & 0 & \partial z/\partial Z \end{bmatrix} = \begin{bmatrix} \sqrt{a} & 0 & 0 \\ 0 & \sqrt{a} & \tau r/a \\ 0 & 0 & 1/a \end{bmatrix}.$$

The associated left Cauchy-Green tensor and its inverse are respectively

$$\mathbf{B} = \mathbf{F}\mathbf{F}^T = \begin{bmatrix} a & 0 & 0 \\ 0 & a + \tau^2 r^2/a^2 & \tau r/a^2 \\ 0 & \tau r/a^2 & 1/a^2 \end{bmatrix},$$
$$\mathbf{B}^{-1} = \begin{bmatrix} 1/a & 0 & 0 \\ 0 & 1/a & -\tau r/a \\ 0 & -\tau r/a & a^2 + \tau^2 r^2/a \end{bmatrix}.$$

By the representation (2.2.3), the non-zero components of the Cauchy stress tensor take the form

$$\begin{aligned} \sigma_{rr} &= -p + \beta_1 a + \beta_{-1}\frac{1}{a}, \\ \sigma_{\theta\theta} &= -p + \beta_1\left(a + \frac{\tau^2 r^2}{a^2}\right) + \beta_{-1}\frac{1}{a}, \\ \sigma_{\theta z} &= \beta_1\frac{\tau r}{a^2} - \beta_{-1}\frac{\tau r}{a}, \\ \sigma_{zz} &= -p + \beta_1\frac{1}{a^2} + \beta_{-1}\left(a^2 + \frac{\tau^2 r^2}{a}\right). \end{aligned} \tag{3.4.3}$$

By the semi-inverse method, since for the deformation (3.4.2) the stress components (3.4.3) depend only on r, the system of equations (3.2.5) reduces to (3.2.6), and integration with respect to r of (3.2.6) together with (3.4.3) implies [128, p. 190]

$$\begin{aligned} \sigma_{rr} &= \frac{\tau^2}{a^2}\int \beta_1 r dr, \\ \sigma_{\theta\theta} &= \sigma_{rr} + \beta_1 r^2\frac{\tau^2}{a^2}, \\ \sigma_{\theta z} &= r\frac{\tau}{a}\left(\frac{\beta_1}{a} - \beta_{-1}\right), \\ \sigma_{zz} &= \sigma_{rr} - \beta_1 a\left(1 - \frac{1}{a^3}\right) + \frac{\beta_{-1}}{a}\left(a^3 - 1\right) + \beta_{-1} r^2\frac{\tau^2}{a}. \end{aligned}$$

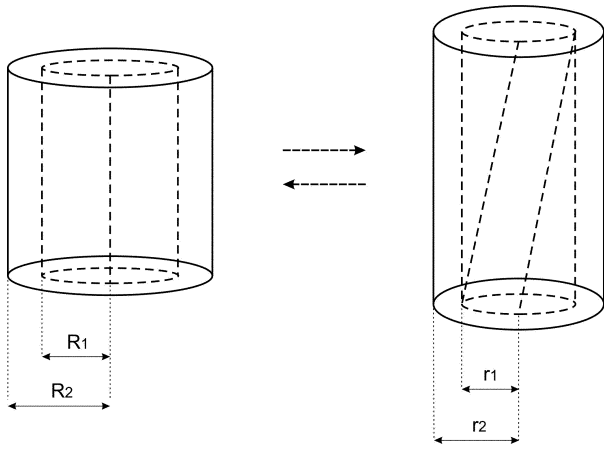

Figure 3.4.1: Schematic of combined stretch and torsion of a circular cylindrical tube.

3.4.1 Nonlinear elastic modulus

For the deformation (3.4.2), the radial direction is a principal direction. Assuming contraction in the radial direction, i.e., $B_{rr} = a < 1$, by the PC inequalities, the associated stress component is negative (radial compression). Setting $\sigma_{rr} = -p_0 \leq 0$ at the external surface $r = r_2$, we obtain

$$\sigma_{rr} = -p_0 + \int_{r_2}^{r} \beta_1 \mathfrak{r} \frac{\tau^2}{a^2} d\mathfrak{r} \leq -p_0 \leq 0, \qquad r \in [r_1, r_2].$$

Since, in the above integral, the integrand is positive, σ_{rr} is an increasing function of r. Equivalently, the radial stress can be expressed as follows

$$\sigma_{rr} = \sigma_{rr}(r_1) + \int_{r_1}^{r} \beta_1 \mathfrak{r} \frac{\tau^2}{a^2} d\mathfrak{r}, \qquad r \in [r_1, r_2].$$

For the deformed tube, we define the nonlinear elastic modulus as the ratio between the Cauchy stress and the logarithmic strain [11,

pp. 218-219] in the radial direction

$$\mathcal{E} = \frac{\sigma_{rr}}{\ln B_{rr}^{1/2}}. \tag{3.4.4}$$

Note that, since $\sigma_{rr} < 0$ increases as r increases and $1/\ln B_{rr}^{1/2} < 0$ is constant, it follows that $\mathcal{E}$ decreases when r increases.

Influence of internal pressure. We first compare the values of the modulus of elasticity (3.4.4) when the tube is empty and when the tube is filled with an incompressible core. Let $\boldsymbol{\sigma}'$ and $\boldsymbol{\sigma}$ denote the Cauchy stress for the filled tube and the empty tube, respectively, and $\mathcal{E}'$ and $\mathcal{E}$ be the corresponding elastic moduli. Setting $\sigma'_{rr}(r_2) = -p_0 < 0$ and $\sigma_{rr}(r_2) = 0$, at equal strains, we deduce that

$$\mathcal{E}' - \mathcal{E} = -\frac{p_0}{\ln \sqrt{a}} > 0, \qquad r \in [r_1, r_2].$$

Hence the radial elastic modulus of the deformed wall is greater for the filled tube than for the empty tube, and the gap between the respective moduli increases as the magnitude of $-p_0$ increases.

Influence of tube thickness. Next, we compare the behaviour of two tubes with different wall thickness. Let $\boldsymbol{\sigma}'$ denote the Cauchy stress when $r'_2 > r_2$ and $r'_1 = r_1$, and $\mathcal{E}'$ be the associated elastic modulus (3.4.4). Since σ_{rr} is an increasing function of r, if $\sigma'_{rr}(r'_2) = \sigma_{rr}(r_2) = -p_0 \leq 0$, then

$$\mathcal{E}' - \mathcal{E} = \frac{1}{\ln \sqrt{a}} \int_{r'_2}^{r_2} \beta_1 \mathfrak{r} \frac{\tau^2}{a^2} d\mathfrak{r} > 0, \qquad r \in [r_1, r_2].$$

In the above integral, the integrand is positive and $r_2 < r'_2$, hence the integral is negative. Since $\ln \sqrt{a} < 0$, the elastic modulus in the radial direction increases when the thickness of the tube wall increases.

Multi-layer tube. We also examine the case when the original tube is surrounded by a second tube which is "attached" to it in the sense that the relative radial displacement across the common interface is equal to zero, and both tubes deform by (3.4.2). Specifically, when the second tube occupies the domain $[R_2, R_2'] \times [-\Theta_0, \Theta_0] \times [-Z_0, Z_0]$ in the reference configuration, and $[r_2, r_2'] \times [-\theta_0, \theta_0] \times [-z_0, z_0]$ in the deformed configuration, where $R_2' > 0$ and $r_2' > 0$ are constants, we wish to verify how the stiffness of the first tube is modified by the presence of the surrounding tube.

We denote by $\boldsymbol{\sigma}'$ the Cauchy stress for either tubes, and by $\mathcal{E}'$ the associated elastic modulus (3.4.4). If the radial strain satisfies $B_{rr} < 1$ for both tubes, then setting $\sigma'_{rr}(r_2') = -p_0 \le 0$, the radial stress of the second tube takes the form

$$\sigma'_{rr}(r) = -p_0 + \int_{r_2'}^{r} \beta_1' \mathfrak{r} \frac{\tau'^2}{a^2} d\mathfrak{r} \le -p_0 \le 0, \qquad r \in [r_2, r_2'],$$

where $\beta_1' > 0$ is the material response for this tube and $\tau' > 0$.

For the first tube, the radial stress is

$$\sigma'_{rr} = \sigma'_{rr}(r_2) + \int_{r_2}^{r} \beta_1 \mathfrak{r} \frac{\tau^2}{a^2} d\mathfrak{r} \le \sigma'_{rr}(r_2), \qquad r \in [r_1, r_2],$$

where $\beta_1 > 0$ is the corresponding material response and $\tau > 0$.

At the same strain, if $\boldsymbol{\sigma}$ represents the Cauchy stress of the original wall when no other wall is attached, such that $\sigma_{rr}(r_2) = -p_0$, then

$$\begin{aligned} \mathcal{E}' - \mathcal{E} =& \frac{\sigma'_{rr}(r_2) + p_0}{\ln B_{rr}^{1/2}} \\ =& \frac{1}{\ln \sqrt{a}} \int_{r_2'}^{r_2} \beta_1' \mathfrak{r} \frac{\tau^2}{a^2} d\mathfrak{r} \\ >& 0, \qquad r \in [r_1, r_2]. \end{aligned}$$

In the above integral, the integrand is positive and $r_2 < r_2'$, hence the integral is negative. Since $\ln\sqrt{a} < 0$, the radial elastic modulus in the first tube is greater when it is surrounded by a second tube. Since the magnitude of $\sigma_{rr}'(r_2)$ relative to $-p_0$ increases as the thickness of the second tube increases, the elastic modulus of the first tube also increases when the thickness of the surrounding tube increases.

The extension to the case of multiple tubes is straightforward. For example, when the second tube is further surrounded by a third tube with the reference domain $[R_2', R_2''] \times [-\Theta_0, \Theta_0] \times [-Z_0, Z_0]$, where $R_2'' > 0$ is constant, and all three tubes deform by (3.4.2), the stiffness of both the first and the second (middle) tube is enhanced by the contact with their surrounding tubes.

Influence of number of tubes when the total material volume is fixed. We further compare the mean elastic modulus for two thin tubes deforming separately by (3.4.2) with that of a single thick tube made form the same material and subject to the same deformation, when the total volume of solid material in the two thin tubes is equal to that in the thick tube. We take the two thin tubes equal in size, with each thin tube $[R_1, R_2] \times [-\Theta_0, \Theta_0] \times [-Z_0, Z_0]$ deforming into $[r_1, r_2] \times [-\theta_0, \theta_0] \times [-z_0, z_0]$, and the thick tube $[R_1, R_2'] \times [-\Theta_0, \Theta_0] \times [-Z_0, Z_0]$ deforming into $[r_1, r_2'] \times [-\theta_0, \theta_0] \times [-z_0, z_0]$, where $R_2'^2 - R_1^2 = 2(R_2^2 - R_1^2)$, hence $r_2'^2 - r_1^2 = 2(r_2^2 - r_1^2)$ (figure 3.4.2).

In the radial direction, we define the mean elastic modulus for the thin tubes as

$$\bar{\mathcal{E}} = \frac{2}{r_2^2 - r_1^2} \int_{r_1^2}^{r_2^2} \mathcal{E} r dr,$$

and for the thick tube as

$$\bar{\mathcal{E}}' = \frac{2}{r_2'^2 - r_1^2} \int_{r_1^2}^{r_2'^2} \mathcal{E} r dr$$

where $\mathcal{E}$ is the radial elastic modulus given by (3.4.4). Note that the mean elastic modulus for the two equal thin tubes is the same as for a single thin tube.

Setting $\sigma_{rr}(r_2) = -p_0 \leq 0$ and $\sigma'_{rr}(r'_2) = -p'_0 \leq 0$ for the corresponding stresses, respectively, such that $\sigma_{rr}(r_1) = \sigma'_{rr}(r_1)$, yields

$$\begin{aligned}
\bar{\mathcal{E}} - \bar{\mathcal{E}}' &= \frac{2}{r_2^2 - r_1^2} \int_{r_1^2}^{r_2^2} \mathcal{E} r dr - \frac{2}{r_2'^2 - r_1^2} \int_{r_1^2}^{r_2'^2} \mathcal{E} r dr \\
&= \frac{2}{r_2^2 - r_1^2} \int_{r_1^2}^{r_2^2} \mathcal{E} r dr - \frac{2}{r_2'^2 - r_1^2} \int_{r_1^2}^{r_2^2} \mathcal{E} r dr - \frac{2}{r_2'^2 - r_1^2} \int_{r_2^2}^{r_2'^2} \mathcal{E} r dr \\
&= \frac{2}{r_2^2 - r_1^2} \int_{r_1^2}^{r_2^2} \mathcal{E} r dr - \frac{1}{r_2^2 - r_1^2} \int_{r_1^2}^{r_2^2} \mathcal{E} r dr - \frac{1}{r_2^2 - r_1^2} \int_{r_2^2}^{r_2'^2} \mathcal{E} r dr \\
&= \frac{1}{r_2^2 - r_1^2} \int_{r_1^2}^{r_2^2} \mathcal{E} r dr - \frac{1}{r_2^2 - r_1^2} \int_{r_2^2}^{r_2'^2} \mathcal{E} r dr \\
&= \frac{1}{2(C_2 - C_1)} \int_{C_1}^{C_2} \mathcal{E} dX - \frac{1}{2(C_2 - C_1)} \int_{C_2}^{C_2'} \mathcal{E} dX \\
&= \frac{1}{2(C_2 - C_1)} \int_{C_1}^{C_2} \left[\mathcal{E}(X) - \mathcal{E}(C_2 + X - C_1) \right] dX \\
&> 0,
\end{aligned}$$

where the change of variable $X = r^2$ was applied, and $C_1 = r_1^2$, $C_2 = r_2^2$, $C_2' = r_2'^2$. The above inequality holds since $\mathcal{E}$ defined by (3.4.4) decreases as r increases and r increases as X increases, hence $\mathcal{E}$ decreases as X increases. Therefore the mean modulus of the thin tubes is greater than the mean modulus of the thick tube.

Since the mean elastic modulus for n equal thin tubes is the same as for a single thin tube, the calculations remain unchanged when the

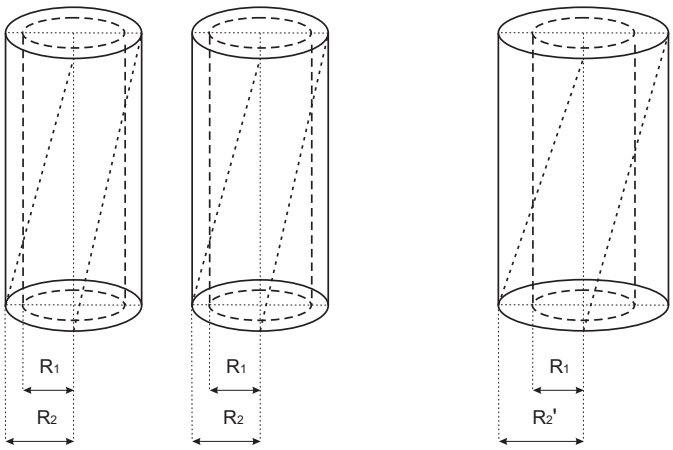

Figure 3.4.2: Schematic of combined stretch and torsion of two thin (left) and one thick (right) circular cylindrical tubes.

two thin tubes $[R_1, R_2] \times [-\Theta_0, \Theta_0] \times [-Z_0, Z_0]$ are replaced by four equal tubes $[R_1, R_2] \times [-\Theta_0, \Theta_0] \times [-Z_0/2, Z_0/2]$.

The analysis extends directly to the case with $n > 2$ equal thin tubes.

Another result of interest concerns the changes in the mechanical properties of a compliant cylindrical core which occupies the interior of a filled circular tube when subject to combined stretch and torsion. The cylinder occupies the domain $[0, R_1] \times [-\Theta_0, \Theta_0] \times [-Z_0, Z_0]$ in the undeformed state, and the tube and the cylinder are deformed simultaneously by (3.4.2). For the solid cylinder, such that $\sigma_{rr} = -p_0 \leq 0$ at the side surface $r = r_1$, the radial stress satisfies

$$\sigma_{rr} = -p_0 + \int_{r_1}^{r} \beta_1 r \frac{\tau^2}{a^2} dr \leq -p_0 \leq 0, \qquad r \in [0, r_1].$$

Influence of cylinder thickness. For two cylinders of different initial radius, let $\boldsymbol{\sigma}'$ be the radial stress when $r_1' > r_1$, and $\mathcal{E}'$ be the associated elastic modulus (3.4.4). Setting $\sigma_{rr}'(r_1') = \sigma_{rr}(r_1) = -p_0 \leq$

0 implies

$$\mathcal{E}' - \mathcal{E} = \frac{1}{\ln\sqrt{a}} \int_{r_1'}^{r_1} \beta_1 \mathfrak{r} \frac{\tau^2}{a^2} d\mathfrak{r} > 0, \qquad r \in [0, r_1].$$

In the above integral, the integrand is positive and $r_1 < r_1'$, hence the integral is negative. Since $\ln\sqrt{a} < 0$, the elastic modulus in the radial direction increases as the radius of the cylinder increases.

Multi-layer cylinder. We now compare the values of the modulus of elasticity, also defined by (3.4.4), when the cylinder is free and when it is surrounded by a circular tube. Let $\bar{\boldsymbol{\sigma}}$ and $\boldsymbol{\sigma}$ denote the Cauchy stress of the cylinder when this is enclosed in a tube and when it is is free, respectively, and $\bar{\mathcal{E}}$ and $\mathcal{E}$ be the corresponding elastic moduli. Since $B_{rr} < 1$, at equal strains, setting $\bar{\sigma}_{rr}(r_1) = -p_0 < 0$ and $\sigma_{rr}(r_1) = 0$, we obtain

$$\bar{\mathcal{E}} - \mathcal{E} = -\frac{p_0}{\ln\sqrt{a}} > 0, \qquad r \in [0, r_1].$$

Hence the radial elastic modulus is greater for the cylinder deforming within the tube, and the gap between the moduli increases as the magnitude of $-p_0$ increases.

Influence of number of cylinders when the total material volume is fixed. Finally, we compare the mean elastic modulus for two separate thin cylinders with the mean modulus for a single thick cylinder made from the same material and subject to the same deformation, when the total volume of the thin cylinders is equal to that of the thick cylinder. We take the two thin cylinders equal in size, with each thin cylinder $[0, R_1] \times [-\Theta_0, \Theta_0] \times [-Z_0, Z_0]$ deforming into $[0, r_1] \times [-\theta_0, \theta_0] \times [-z_0, z_0]$, and the thick cylinder $[0, R_1'] \times [-\Theta_0, \Theta_0] \times [-Z_0, Z_0]$ deforming into $[0, r_1'] \times [-\theta_0, \theta_0] \times [-z_0, z_0]$, where $R_1'^2 = 2R_1^2$

(figure 3.4.3).

Setting $\sigma_{rr}(r_1) = -p_0 \leq 0$ and $\sigma'_{rr}(r'_1) = -p'_0 \leq 0$ for the corresponding stresses, respectively, such that $\sigma_{rr}(0) = \sigma'_{rr}(0)$, yields

$$\begin{aligned}
\bar{\mathcal{E}} - \bar{\mathcal{E}}' =& \frac{2}{r_1^2}\int_0^{r_1^2} \mathcal{E} r dr - \frac{2}{r_1'^2}\int_0^{r_1'^2} \mathcal{E} r dr \\
=& \frac{2}{r_1^2}\int_0^{r_1^2} \mathcal{E} r dr - \frac{2}{r_1'^2}\int_0^{r_1'^2} \mathcal{E} r dr - \frac{2}{r_1'^2}\int_0^{r_1'^2} \mathcal{E} r dr \\
=& \frac{2}{r_1^2}\int_0^{r_1^2} \mathcal{E} r dr - \frac{1}{r_1^2}\int_0^{r_1^2} \mathcal{E} r dr - \frac{1}{r_1^2}\int_0^{r_1'^2} \mathcal{E} r dr \\
=& \frac{1}{r_1^2}\int_0^{r_1^2} \mathcal{E} r dr - \frac{1}{r_1^2}\int_0^{r_1'^2} \mathcal{E} r dr \\
=& \frac{1}{2C_1}\int_0^{C_1} \mathcal{E} dX - \frac{1}{2C_1}\int_{C_1}^{C_1'} \mathcal{E} dX \\
=& \frac{1}{2C_1}\int_0^{C_1} \left[\mathcal{E}(X) - \mathcal{E}(C_1 + X)\right] dX \\
& > 0,
\end{aligned}$$

where the change of variable $X = r^2$ was applied, and $C_1 = r_1^2$, $C'_1 = r_1'^2$. The above inequality holds since $\mathcal{E}$ defined by (3.4.4) decreases as r increases and r increases as X increases, hence $\mathcal{E}$ decreases as X increases. Therefore the mean modulus of the two thin cylinders is greater than the mean modulus of the thick cylinder.

Since the mean elastic modulus for n equal thin cyliners is the same as for a single thin cylinder, the calculations remain unchanged if the two thin cylinders $[0, R_1] \times [-\Theta_0, \Theta_0] \times [-Z_0, Z_0]$ are replaced by four equal cylinders $[0, R_1] \times [-\Theta_0, \Theta_0] \times [-Z_0/2, Z_0/2]$.

The analysis extends directly to the case with $n > 2$ equal thin cylinders.

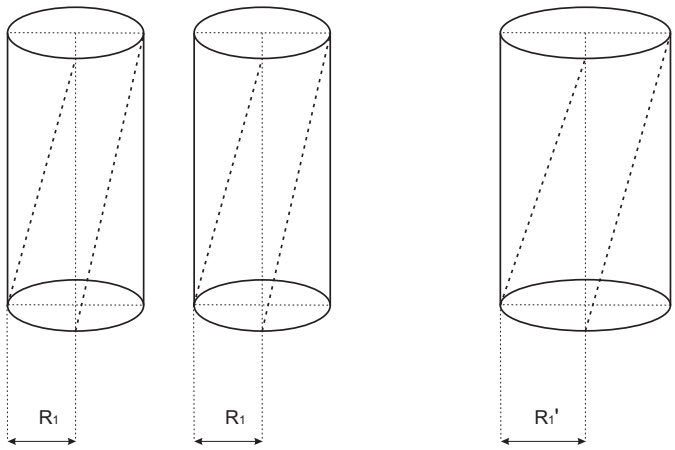

Figure 3.4.3: Schematic of combined stretch and torsion of two thin (left) and one thick (right) circular cylinders.

3.4.2 Optimisation problem

Since the radial elastic modulus defined by (3.4.4) increases with the tube wall thickness, we employ this modulus to find the minimum wall thickness for the deformation (3.4.2). Assuming $B_{rr} = a < 1$, we formulate the following optimisation problem [41]

$$\text{find } r_1 = \sup\ V, \qquad V = \{r < r_2 \mid \mathcal{E}(r) \geq C\},$$

where $C > 0$ is given. Since

$$\mathcal{E}(r) = -\frac{p_0}{\ln\sqrt{a}} + \frac{1}{\ln\sqrt{a}}\int_{r_2}^{r} \beta_1 r \frac{\tau^2}{a^2} dr \geq C,$$
$$\text{for all} \quad r^2 \geq r_2^2 + \frac{a^2 \ln a}{\beta_1 \tau^2}\left(C + \frac{p_0}{\ln\sqrt{a}}\right),$$

where $0 < a < 1$ and $p_0 < 0$ imply

$$\frac{a^2 \ln a}{\beta_1 \tau^2}\left(C + \frac{p_0}{\ln\sqrt{a}}\right) < 0,$$

we deduce that

$$\mathcal{E}(r) \geq C \qquad \text{for all} \quad \sqrt{r_2^2 + \frac{a^2 \ln a}{\beta_1 \tau^2}\left(C + \frac{p_0}{\ln \sqrt{a}}\right)} \leq r < r_2.$$

Thus V is bounded and non-empty and the optimisation problem has a solution.

The problem of finding the minimum surface pressure or number of tubes when the total volume of elastic material is fixed can be formulated analogously.

We conclude that the constraint involving a bound on the elastic modulus (3.4.4) can be employed to find the optimal tube thickness, surface pressure, or number of tubes when the total volume of solid material remains fixed under the deformation (3.4.2), regardless of the material responses.

3.5 Summary

In this chapter, for hyperelastic cell walls subject to different non-homogeneous deformations, we identified a nonlinear elastic modulus representing the ratio between the stress and the strain in a principal direction associated with the change of curvature, and proved that this modulus: (i) increases as the thickness of the cell wall increases or when the wall is multi-layer, (ii) is smaller for a single thick wall than for multiple thin walls made from the same volume of material, and increases as the number of thin walls increases while the volume of material remains unchanged, and (iii) increases also as the internal cell pressure increases. Since these results are independent of the choice of the strain energy function describing the cell wall material, the

nonlinear elastic modulus identified here can be taken as indicative for finding the optimum wall thickness, number of walls, or cell pressure under similar deformations in a wide range of different hyperelastic materials.

Chapter 4

Computational models

4.1 Introduction

In this chapter, we assess numerically the independent influence of mechanical features, such as: (i) the wall thickness, (ii) the number of cells when the total volume of elastic material in the structure is fixed, and (iii) the stiffness of the compliant inclusions on the collective behaviour of groups of cells under large strain deformations. To achieve this, we model periodic, honeycomb-like structures with regular geometry, such as square, diamond-shape, and hexagonal cells, formed from a single piece of elastic material which occupies a thin square domain of (dimensionless) side one in the X-(horizontal) and Y-(vertical) directions, and 0.1 in the Z-(out-of-plane) direction, such that the cells are equal in size throughout the structure. Each structure is deformed by imposing the following boundary conditions: the lower external horizontal face is fixed in the second/vertical/Y-direction and free to slide in the first/horizontal/X-direction and in the third/out-of-plane/Z-direction; the upper external horizontal face is subject to a prescribed vertical displacement and is free to slide horizontally and out-of-plane; and the remaining external and internal cell faces deform freely.

The numerical results recorded here were obtained by a standard finite element procedure implemented within the open-source software Finite Elements for Biomechanics (FEBio) environment [73] (see supplementary material for original source files). We note that, in the finite element simulations, the resulting nonlinear elastic deformations of the cell walls are generally more complex that the idealised deformations studied analytically in the previous chapter. Since the finite element implementation requires the strain energy function for the cell wall material to be specified a priori, the following two different hyperelastic models were used:

(NH) In the first model, the cell walls and the cell cores were characterised by a compressible neo-Hookean strain energy density function

$$\mathcal{W}(I_1, I_2, I_3) = \frac{\mu}{2}\left(I_1 - 3 - \ln I_3\right) + \frac{\lambda}{2}\left(\ln I_3^{1/2}\right)^2, \tag{4.1.1}$$

where $\mu = E/[2(1+\nu)] > 0$ and $\lambda = \nu E/[(1+\nu)(1-2\nu)] > 0$ are constants, and are equal to the corresponding Lamé parameters from the linear elastic theory. In the numerical examples, we set $E = 0.1$ MPa and $\nu = 0.49$ for the cell walls, and $E = 0.01$ MPa (cellular pads 1) or $E = 0.005$ MPa (cellular pads 2) and $\nu = 0.495$ for the cell cores.

(MR) In the second model, the cell walls and the cell inclusions were described by the generalised Mooney-Rivlin strain energy density function

$$\begin{aligned}\mathcal{W}(I_1, I_2, I_3) = \frac{\mu_1}{2}\left(I_3^{-1/3} I_1 - 3\right) + \frac{\mu_2}{2}\left(I_3^{-2/3} I_2 - 3\right) \\ + \frac{\kappa}{2}\left(I_3^{1/2} - 1\right)^2,\end{aligned} \tag{4.1.2}$$

where μ_1 and μ_2 are constants, such that $\mu = \mu_1 + \mu_2 > 0$ is the shear modulus, and $\kappa > 0$ is the bulk modulus form linear elasticity. In the numerical models, we set $\mu_1 = 0.0016$ MPa, $\mu_2 = 0.032$ MPa, $\kappa = 1.6667$ MPa for the cell walls, and $\mu_1 = 0.0001$ MPa, $\mu_2 = 0.0032$ MPa, $\kappa = 0.3333$ MPa (cellular pads 1) or $\mu_1 = 0.0002$ MPa, $\mu_2 = 0.0015$ MPa, $\kappa = 0.1667$ MPa (cellular pads 2) for the inclusions.

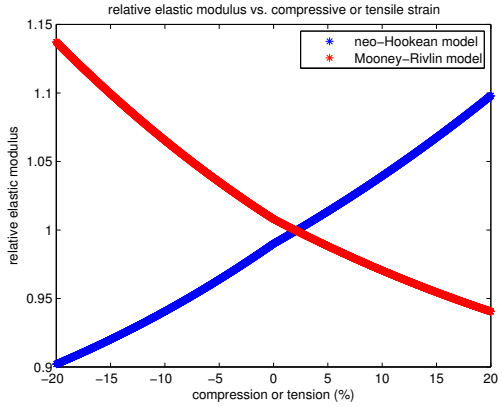

Figure 4.1.1: Nonlinear elastic modulus $\mathcal{E}$ normalised to E for the NH and MR models.

These material models are representative for nonlinear hyperelastic materials exhibiting different mechanical behaviours under simple tension or compression [25, 81, 137]. Specifically, the nonlinear elastic modulus representing the ratio between the Cauchy stress and the logarithmic strain in the direction of the applied tensile or compressive force [11, pp. 218-219],

$$E = \frac{a^3 - 1}{a^2 \ln a} \left(a\beta_1 - \beta_{-1} \right), \tag{4.1.3}$$

where $a > 0$ is the stretch in the corresponding direction, increases as tension increases and decreases as compression increases for the NH model (4.1.1), and decreases under increasing tension and increases

under increasing compression for the MR model (4.1.2). The parameter (4.1.3) illustrates the relative behaviour of the tensile or compressive stress of the hyperelastic material under the finite deformation (figure 4.1.1).

For the structural models, the nonlinear elastic modulus was computed as the quotient of the average value of the effective Cauchy stress σ_{eff} to the effective logarithmic strain $\ln C_{eff}^{1/2}$. The effective value of a symmetric tensor $\mathbf{S}$ was defined as [59, 64]

$$
\begin{aligned}
S_{eff} &= \sqrt{\frac{3}{2}\left[\left(\mathbf{S}-\frac{1}{3}tr(\mathbf{S})\mathbf{I}\right):\left(\mathbf{S}-\frac{1}{3}tr(\mathbf{S})\mathbf{I}\right)\right]} \\
&= \sqrt{\frac{3}{2}tr\left[\left(\mathbf{S}-\frac{1}{3}tr(\mathbf{S})\mathbf{I}\right)^{T}\left(\mathbf{S}-\frac{1}{3}tr(\mathbf{S})\mathbf{I}\right)\right]} \\
&= \sqrt{S_{11}^2+S_{22}^2+S_{33}^2-S_{11}S_{22}-S_{22}S_{33}-S_{33}S_{11}+3\left(S_{12}^2+S_{13}^2+S_{23}^2\right)}.
\end{aligned}
$$

The average effective value was calculated as

$$\bar{S}_{eff} = \frac{1}{N}\sum_{i=1}^{N} S_i,$$

where N is the number of finite elements and S_i is the effective value on the element i.

The rest of the chapter is organised as follows: in Section 4.2, numerical examples show the mechanical effects due to the presence of cell inclusions; in Section 4.3, the mechanical influence of increasing the cell wall thickness is illustrated numerically; in Section 4.4, the effects of increasing the number of cells while preserving the overall volume of cell wall material are recorded.

4.2 Influence of cell inclusions

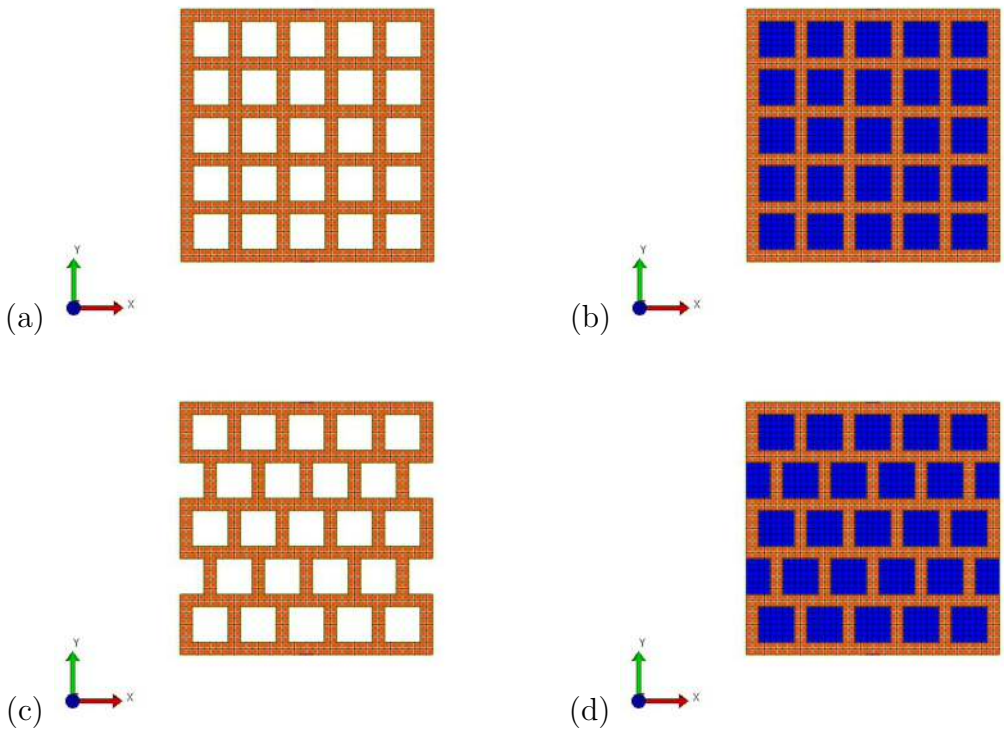

Figure 4.2.1: Undeformed (a,c) honeycomb structures and (b,d) cellular pads with (a,b) stacked and (c,d) staggered cells.

For the cellular structures shown in figure 4.2.1 (a) and (c), the cells are squares of approximate side 0.2 in the horizontal and vertical directions, and are arranged periodically in a stacked or staggered configuration throughout the structure. The cellular pads in figure 4.2.1 (b) and (d) are obtained by filling the empty cells of the corresponding honeycomb structure with a hyperelastic material which is softer than the cell wall material, and complies with the deformation of the cell walls in the sense that the displacements are continuous across the interface between the walls and the inclusions. In these figures, the finite element mesh is also shown.

For the honeycombs, the internal cell faces are free, while for the cellular pads, the displacements are continuous across the interface

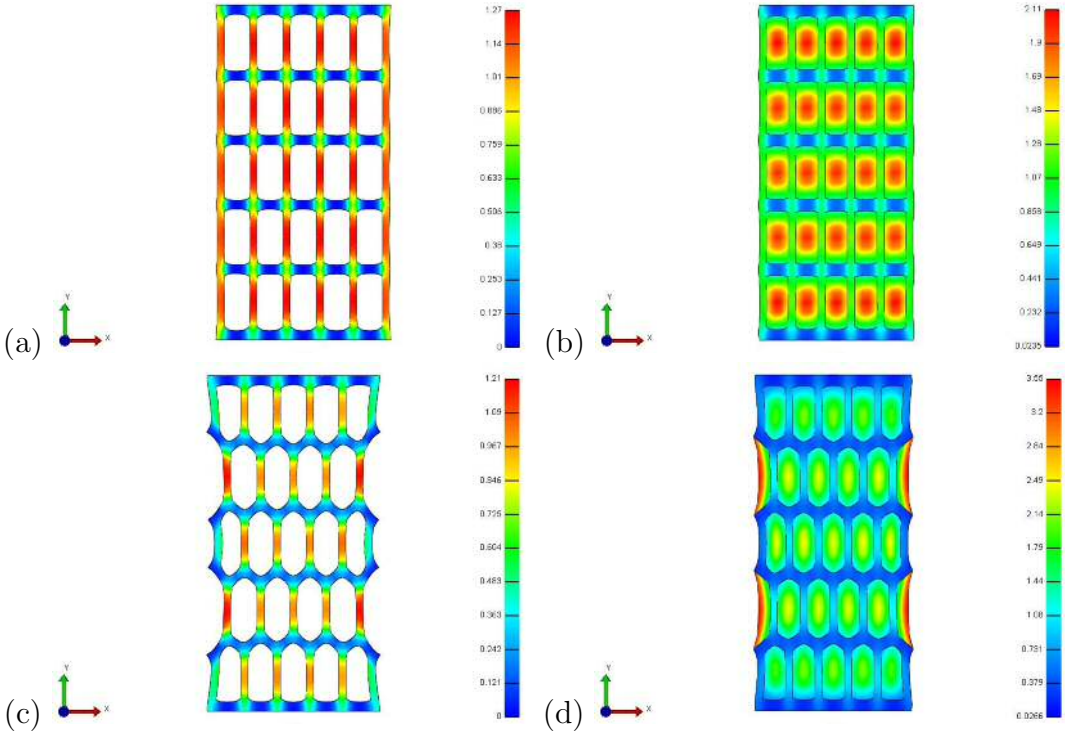

Figure 4.2.2: FEBio simulations of deformed structures with NH components subject to 50% stretch in the vertical direction, showing the non-homogeneous Green-Lagrange strains in the first principal (vertical) direction for (a,c) honeycomb structures and (b,d) cellular pads 1 with (a,b) stacked and (c,d) staggered cells.

between the cell walls and cell cores. The non-homogeneous deformations of the cellular structures of NH materials where $E = 0.1$ MPa for the cell walls and $E = 0.01$ MPa for the cell cores are depicted in figure 4.2.2. Note that, for the structures with staggered cells, the cell geometry changes as the original horizontal walls appear to 'bend' outside the cells. Analogous deformations were observed in structures made from MR materials.

In figure 4.2.3 (a,c) and figure 4.2.4 (a,c), we record the mean values of the effective Cauchy stress *vs.* those of the effective logarithmic strain throughout the solid matter. In figure 4.2.3 (b,d) and figure 4.2.4 (b,d), the *nonlinear elastic modulus* representing the ratio between the mean effective Cauchy stress and the mean effective logarithmic strain is indicated. In the plots, square symbols correspond to

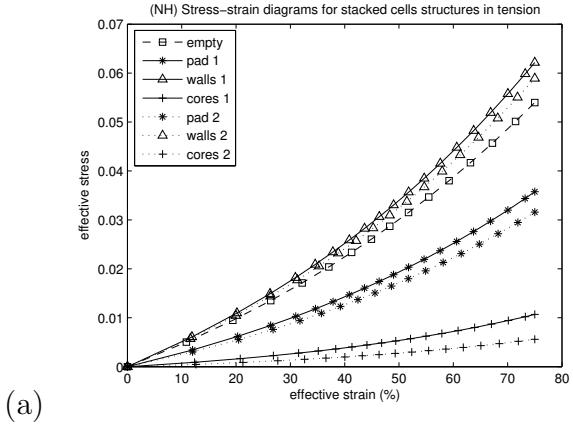

(a)

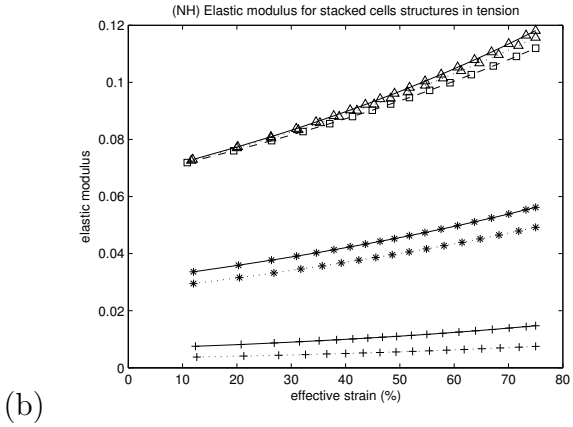

(b)

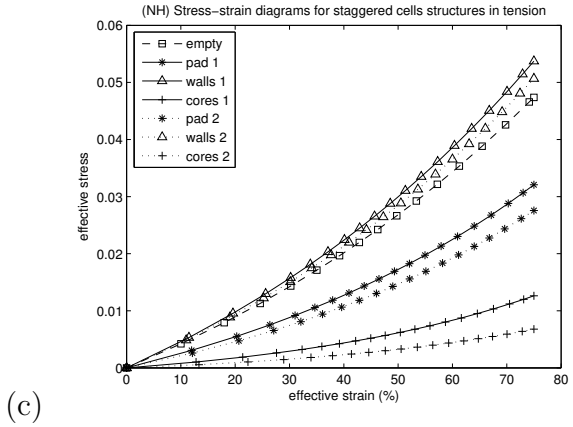

(c)

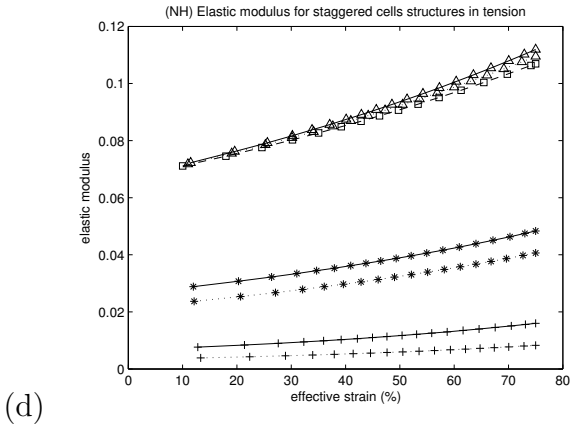

(d)

Figure 4.2.3: (a,c) Mean effective Cauchy stress (MPa) and (b,d) nonlinear elastic modulus (MPa) *vs.* mean effective logarithmic strain for cellular structures with (a,b) stacked and (c,d) staggered cells of NH material.

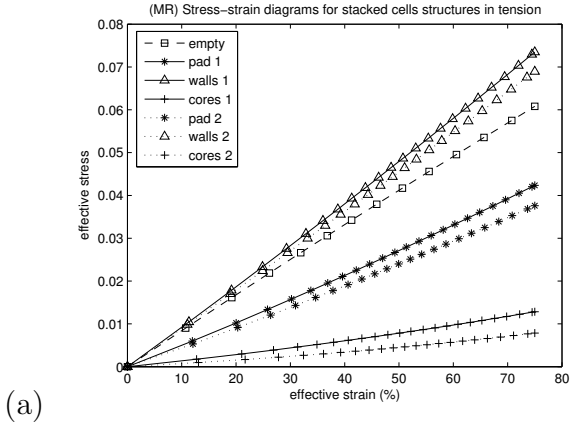

(a)

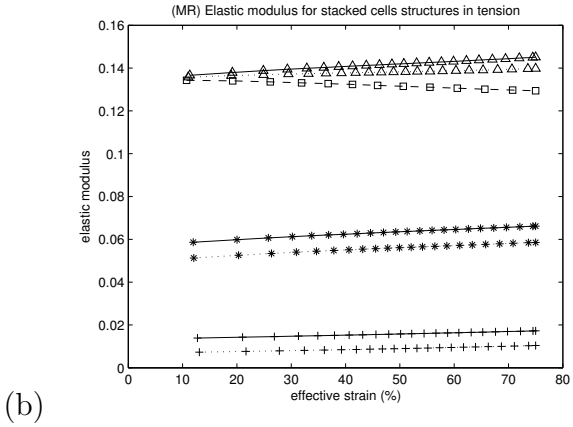

(b)

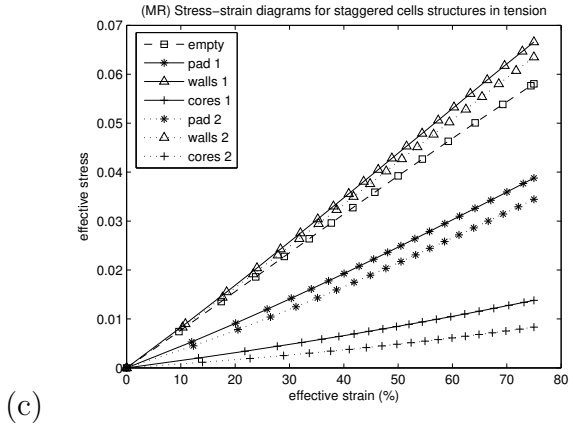

(c)

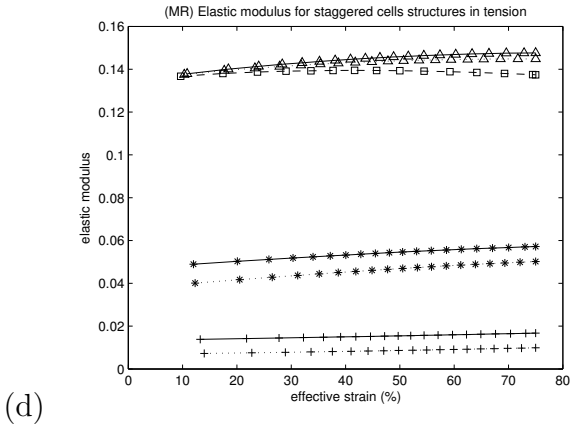

(d)

Figure 4.2.4: (a,c) Mean effective Cauchy stress (MPa) and (b,d) nonlinear elastic modulus (MPa) *vs.* mean effective logarithmic strain for cellular structures with (a,b) stacked and (c,d) staggered cells of MR material.

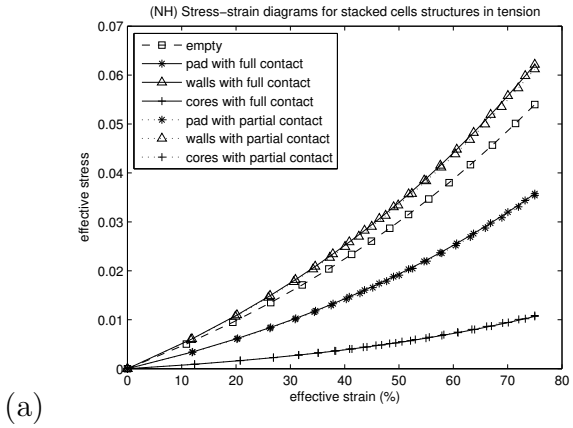

(a)

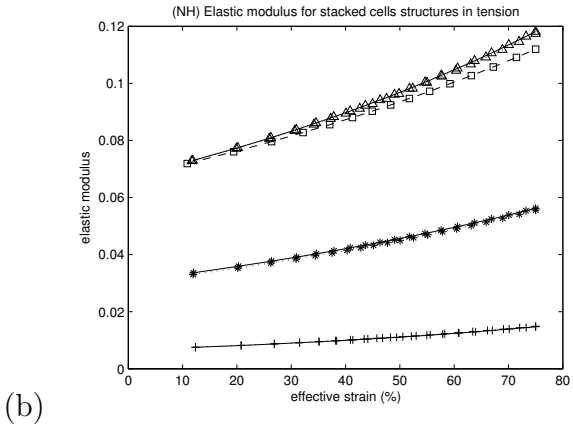

(b)

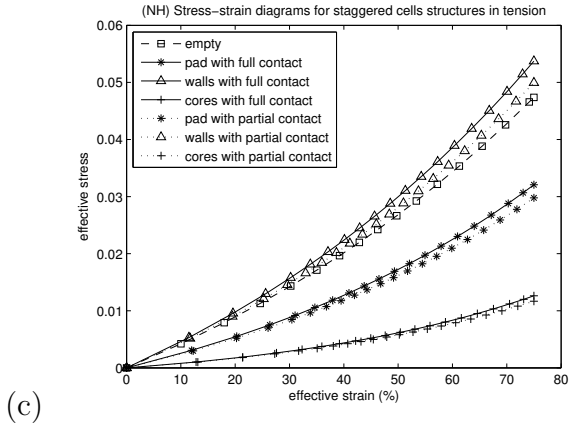

(c)

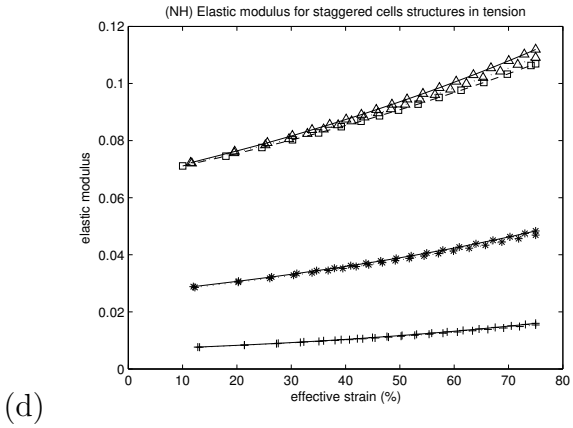

(d)

Figure 4.2.5: (a,c) Mean effective Cauchy stress (MPa) and (b,d) nonlinear elastic modulus (MPa) *vs.* mean effective logarithmic strain for cellular structures of NH material with different contact conditions between cell walls and cell cores.

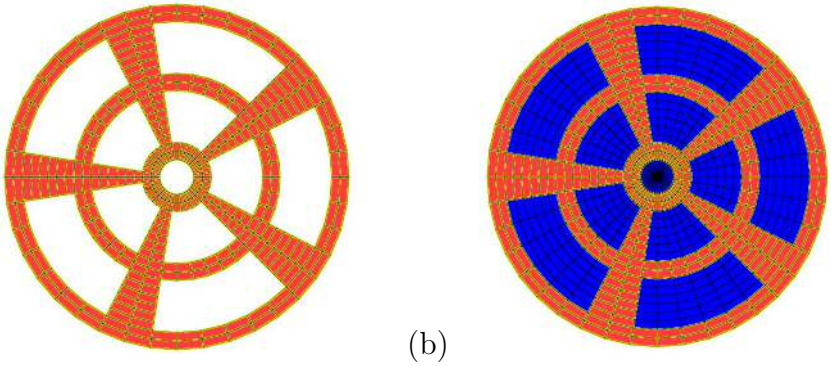

(a) (b)

Figure 4.2.6: Cross-section of undeformed (a) cylindrical structure and (b) cellular pad with wedge shaped cells.

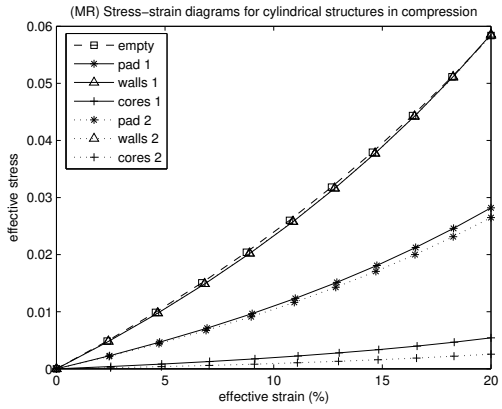

(a)

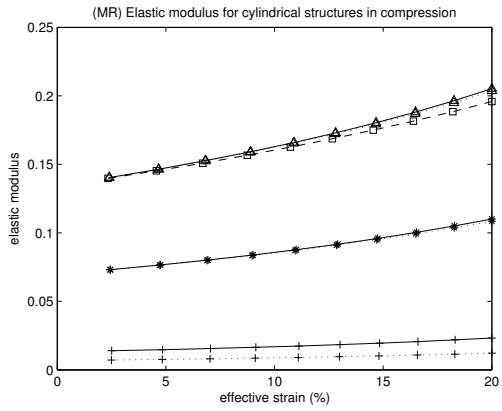

(b)

Figure 4.2.7: (a) Mean effective Cauchy stress (MPa) and (b) nonlinear elastic modulus (MPa) *vs.* mean effective logarithmic strain for cylindrical cellular structures with wedge shaped cells of MR material.

the cell walls in the empty cells structure, stars are for the overall filled cells structure (cellular pad), triangles correspond to the cell walls in the cellular pad, and plus symbols are for the cell cores.

From these results, we infer that the cell walls are stiffer in the cellular pads than in the corresponding honeycombs, and also in structures where the elastic modulus of the inclusions is higher (cellular pads 1) compared to those where the elastic modulus of the inclusions is lower (cellular pads 2). The numerical results for the staggered cells in figures 4.2.3 and 4.2.4 differ only slightly from those corresponding to the stacked cells, suggesting that the observed behaviour is mainly due to the elastic stretch, while the bending of the initially horizontal walls in the staggered cells is responsible for a reduction in both the stress level and the stiffness of the cell walls relative to those in the stacked cells.

The overall elastic modulus of the cellular pads also increases as the stiffness of the elastic core increases. For structures made from NH and MR components (figures 4.2.3 and 4.2.4, respectively), as the deformation increases, the nonlinear elastic modulus in the cell walls of NH material increases whereas in those made from MR material may decrease (figure 4.1.1), but in all cases, the stiffness of the cell inclusions increases. Consequently, while the mean elastic modulus of the cellular pads made from NH materials clearly increases, the mean elastic modulus of the pads made from MR materials is almost constant.

We further assess the nonlinear elastic modulus of cellular pads when gaps are allowed to open between vertical walls and cell core. In this case, figure 4.2.5 shows that the stiffness of the cell walls where

core separation occurs is higher than in the empty cells, but lower than in the case when full contact between cell walls and cell core is maintained everywhere. These differences in the respective cell wall stiffness also appear to increase as the deformation increases. The nonlinear elastic modulus of the cellular pads with or without gaps is approximately the same, and appears slightly larger when full contact between the cell walls and the cell core is maintained if the deformation is sufficiently large.

Finally, we model cylindrical structures with wedge shaped cells which are either empty or filled with compliant cores. For these models, the radius of the cross-section is (dimensionless) unity, the height is 0.2, and the cross-section geometry is illustrated in figure 4.2.6. The corresponding boundary conditions are: a small twist (1.5% of 360°) superposed on axial compression (up to 20% of 0.2) prescribed on the upper circular face, zero displacements on the lower circular face, and free side surface, while the internal faces of the empty cells are free, and at the interface between the cell walls and the cell cores, the displacements are continuous. For structures made from MR materials, the resulting stress-strain diagrams and elastic moduli are indicated in figure 4.2.7. In this case also, the nonlinear elastic modulus of the cell walls is larger when the cells are filled than when the cells are empty, and under sufficiently large deformation, slightly larger if the elastic modulus of the elastic core is higher (cylindrical pad 1) than when the elastic modulus of the core is lower (cylindrical pad 2). However, the overall elastic modulus of the cylindrical pads appears almost insensitive to the core stiffness.

4.3 Influence of cell wall thickness

In figure 4.3.1, the undeformed structures with uniform cell size and different cell wall thickness to length ratio (t/L) are shown. The deformed structures of NH material are illustrated in figure 4.3.2, where the initially horizontal walls of the staggered cells bend, while the inclined walls of the diamond cells are sheared. Similar deformations were observed in structures of MR material. For the model structures of NH or MR material, the mean values of the effective Cauchy stress *vs.* those of the effective logarithmic strain throughout the solid walls are shown in figures 4.3.3, 4.3.4, 4.3.5, and 4.3.6 (a,c). The values of the associated *nonlinear elastic modulus* defined as the ratio between the mean effective Cauchy stress and the mean effective logarithmic strain are represented in figures 4.3.3, 4.3.4, 4.3.5, and 4.3.6 (b,d), respectively. The numerical results suggest that the stress and the nonlinear elastic modulus increase with the cell wall thickness.

Table 4.3.1: Vertical displacement under applied tensile force of 100 N at the top horizontal boundary for cellular structures of NH material with square cells having different cell wall thickness to length ratio.

Cellular Structure	Cell Wall Thickness	Vertical Displacement
Stacked Cells	thin ($t/L \approx 0.15$)	1.229
	medium ($t/L \approx 0.33$)	0.4428
	thick ($t/L \approx 0.95$)	0.1686
Staggered Cells	thin ($t/L \approx 0.15$)	1.756
	medium ($t/L \approx 0.33$)	0.5941
	thick ($t/L \approx 0.95$)	0.1965

To see how the stiffness of the deformed cell walls affects the behaviour of the overall structure, we further compare the behaviour of the model structures wity square cells under a fixed vertical tensile load applied at the top horizontal boundary, while the conditions at

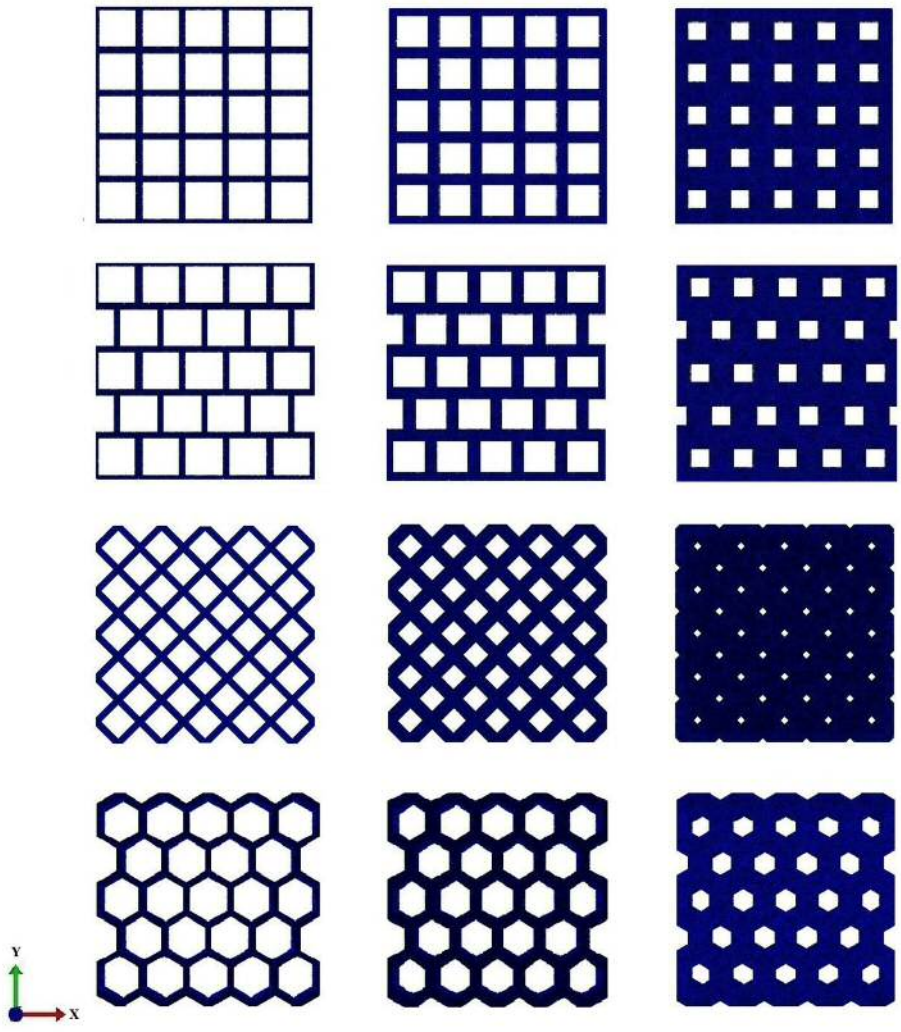

Figure 4.3.1: Undeformed model structures with stacked (top row), staggered (middle top row), diamond (middle bottom row), and hexagon (bottom row) cell geometry, and thin (left column), medium (middle column), and thick (right column) cell walls.

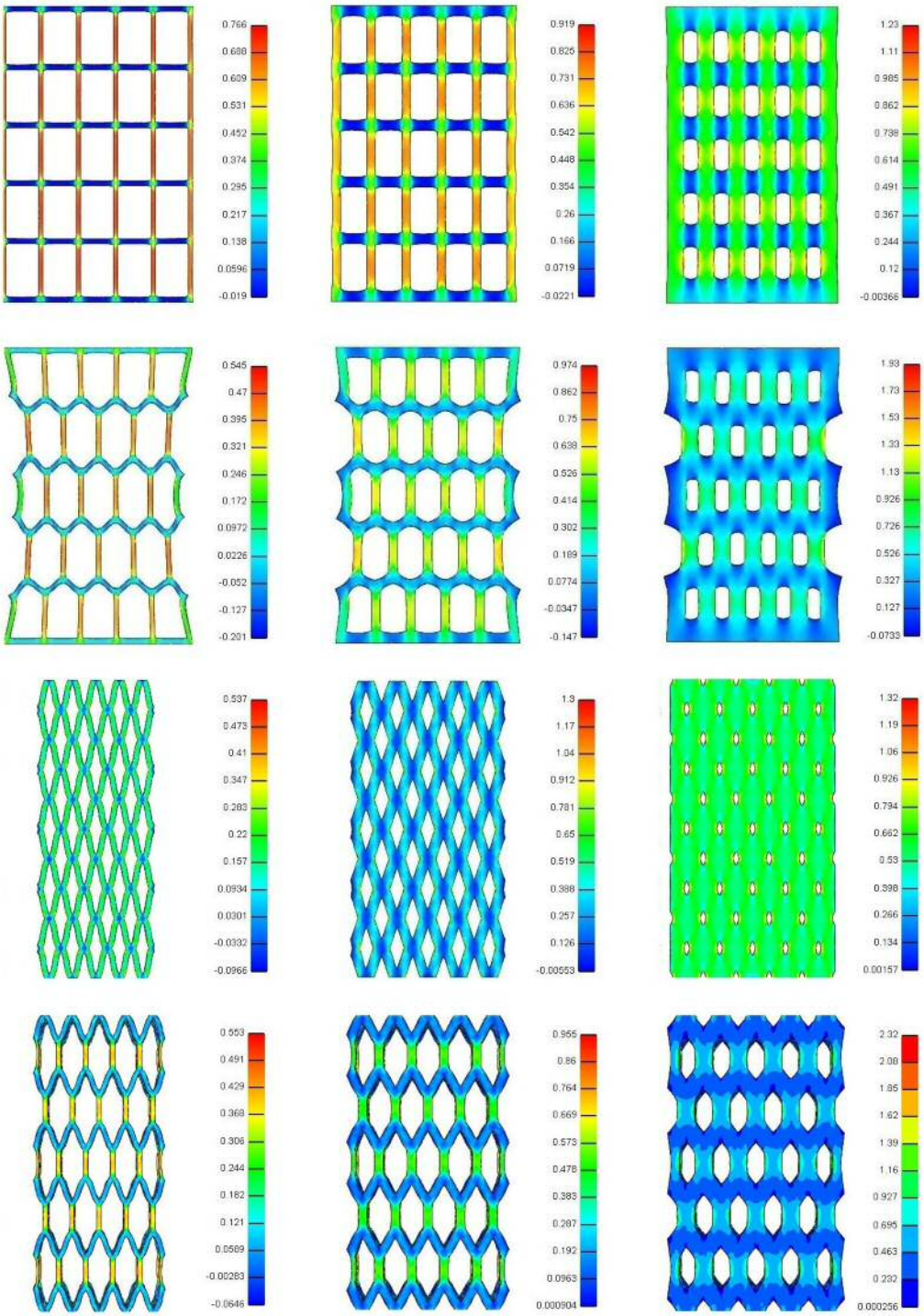

Figure 4.3.2: FEBio simulations of deformed structures with stacked (top row), staggered (middle top row), diamond (middle bottom row), and hexagon (bottom row) cell geometry, and thin (left column), medium (middle column), and thick (right column) cell walls of NH material subject to 50% stretch in the vertical direction, showing the non-homogeneous Green-Lagrange strains in the first principal (vertical) direction.

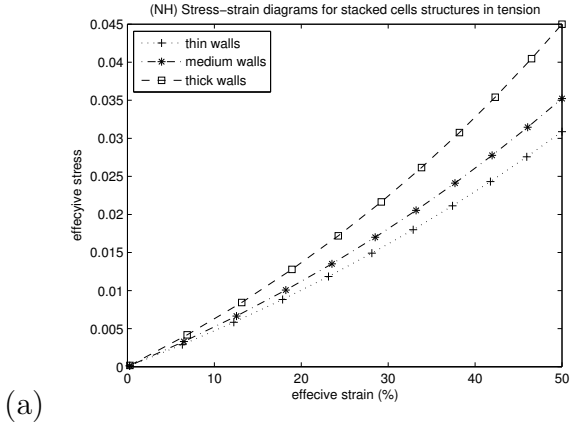

(a)

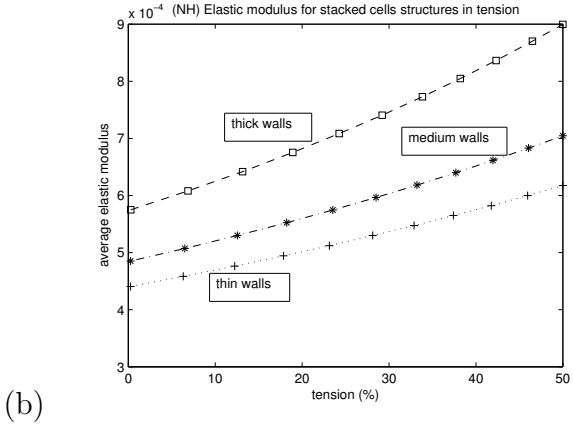

(b)

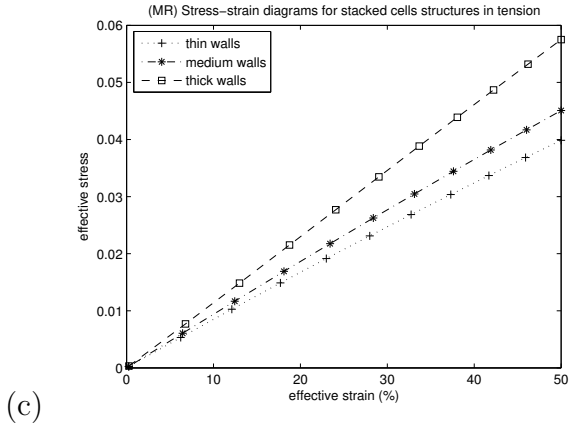

(c)

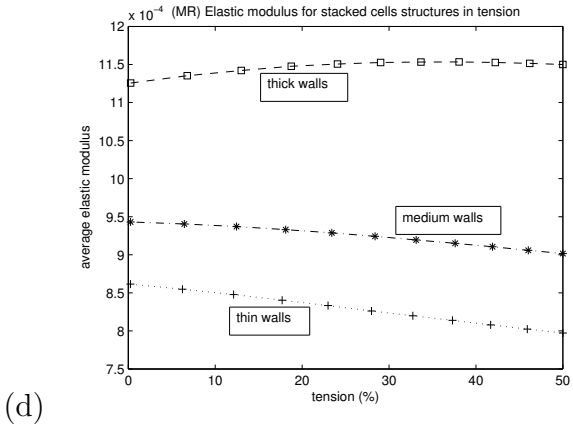

(d)

Figure 4.3.3: (a,c) Mean effective Cauchy stress (MPa) and (b,d) nonlinear elastic modulus (MPa) *vs.* mean effective logarithmic strain for stacked cells structures of (a,b) NH and (c,d) MR material with different cell wall thickness.

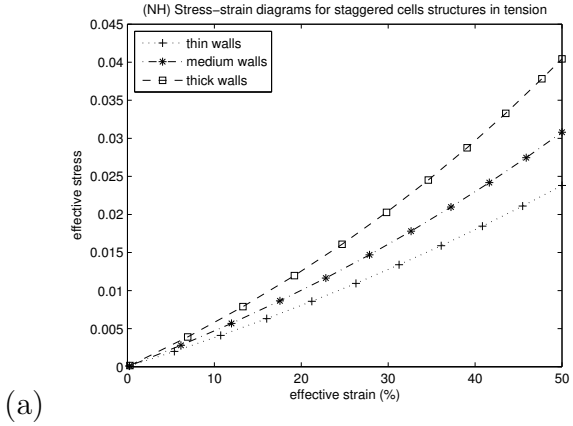

(a)

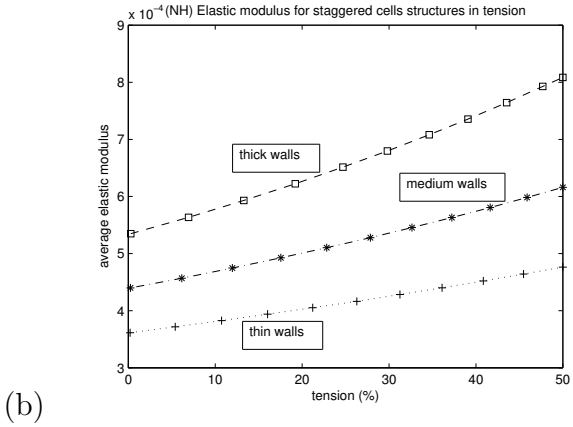

(b)

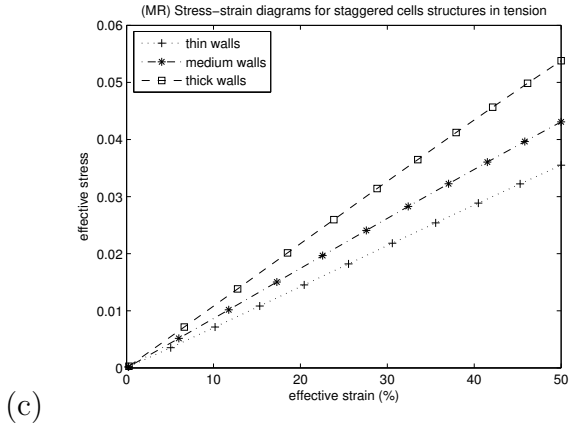

(c)

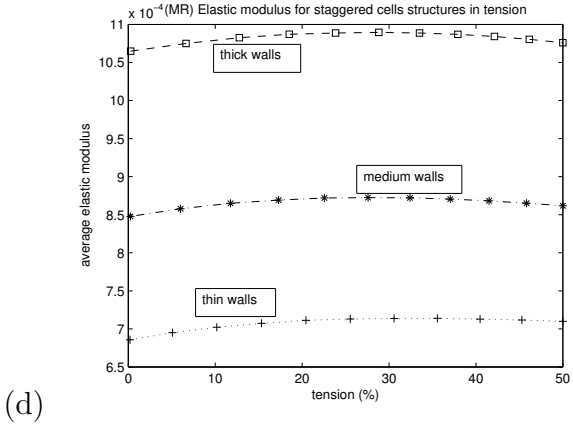

(d)

Figure 4.3.4: (a,c) Mean effective Cauchy stress (MPa) and (b,d) nonlinear elastic modulus (MPa) *vs.* mean effective logarithmic strain for staggered cells structures of (a,b) NH and (c,d) MR material with different cell wall thickness.

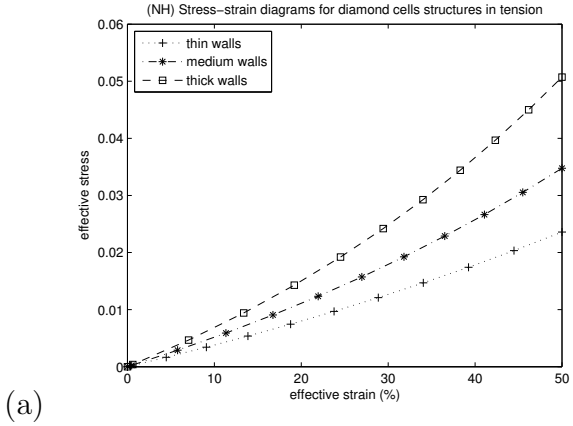

(a)

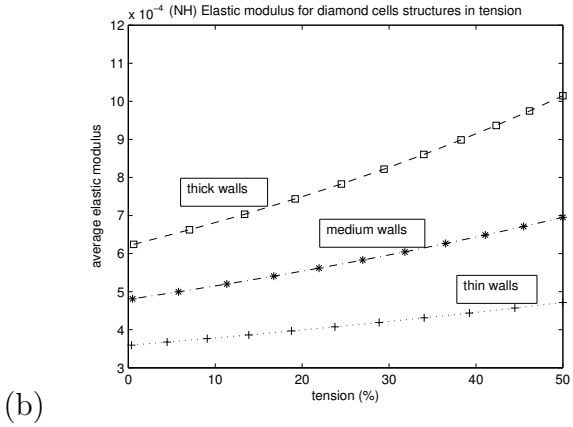

(b)

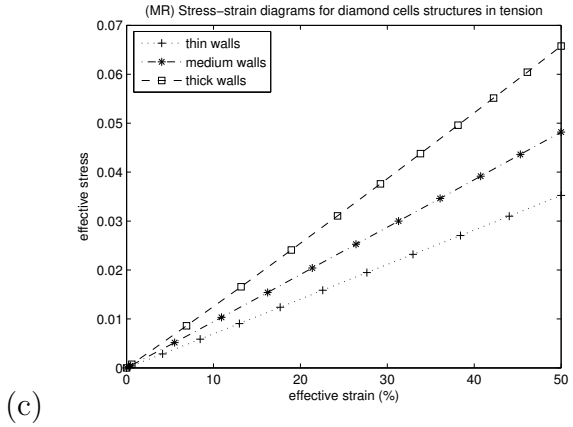

(c)

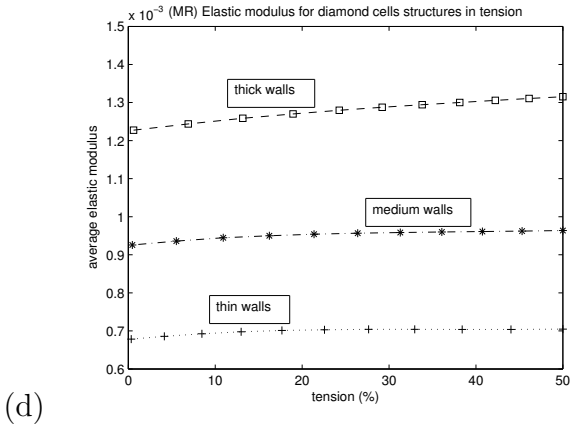

(d)

Figure 4.3.5: (a,c) Mean effective Cauchy stress (MPa) and (b,d) nonlinear elastic modulus (MPa) *vs.* mean effective logarithmic strain for diamond cells structures of (a,b) NH and (c,d) MR material with different cell wall thickness.

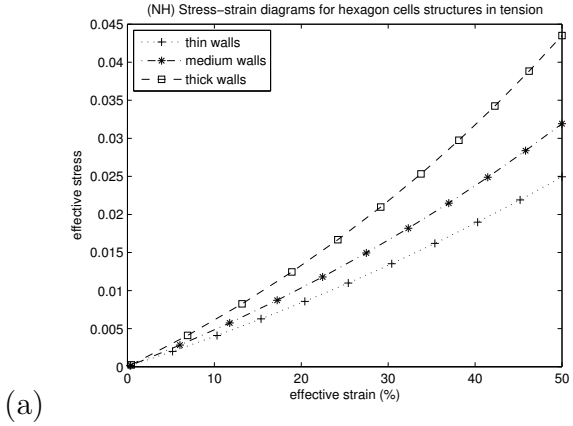

(a)

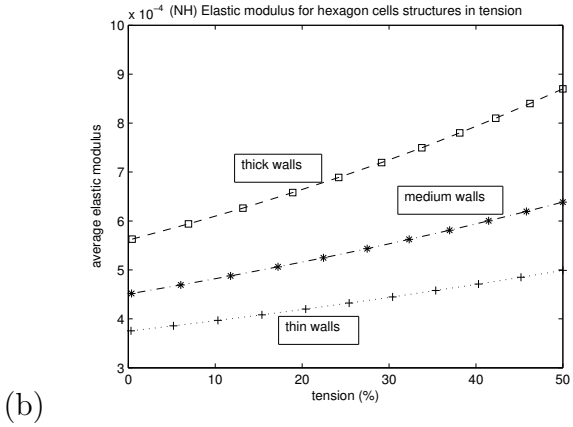

(b)

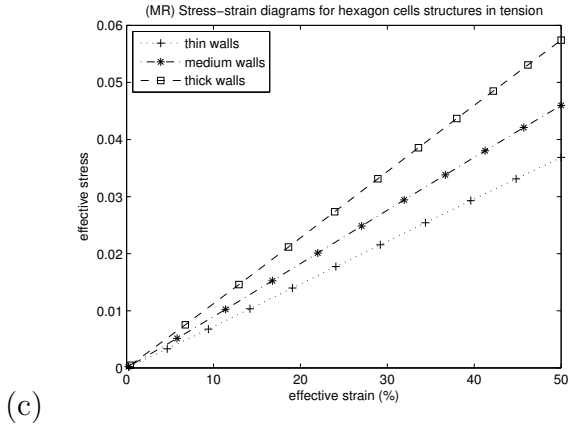

(c)

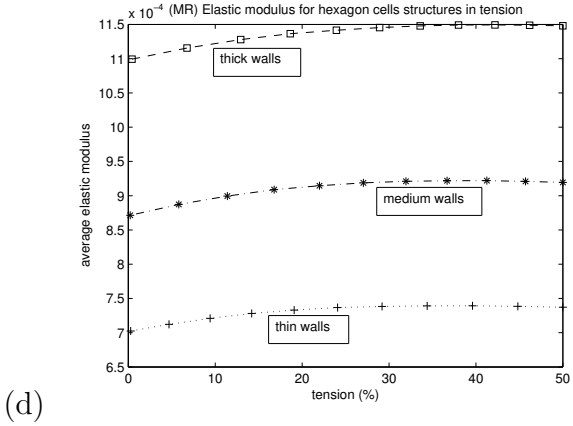

(d)

Figure 4.3.6: (a,c) Mean effective Cauchy stress (MPa) and (b,d) nonlinear elastic modulus (MPa) *vs.* mean effective logarithmic strain for hexagon cells structures of (a,b) NH and (c,d) MR material with different cell wall thickness.

the other boundaries remain as before. The values for the vertical displacements obtained for each structure are recorded in table 4.3.1, and confirm that, under the same vertical force, the structures with thicker walls will deform less than those with thinner walls.

4.4 Influence of cell density

In figure 4.4.1, the undeformed structures with uniform cell size and an increasing number of cells while the volume of solid material remains unchanged are presented. In these models, for the stacked and diamond cells, the ratio between the thickness and the length of the cell walls is also unchanged as the number of cells increases, while for the staggered and hexagonal cells, this ratio increases slightly. The deformed structures of NH material are shown in figure 4.4.2. For the structures of NH or MR material with an increasing number of cells, the mean values of the effective Cauchy stress *vs.* those of the effective logarithmic strain throughout the solid walls are recorded in figures 4.4.3, 4.4.4, 4.4.5, and 4.4.6 (a,c). The corresponding values of the *nonlinear elastic modulus* are indicated in figures 4.4.3, 4.4.4, 4.4.5, and 4.4.6 (b,d). These results indicate that the stress and the nonlinear elastic modulus increase as the number of cells increases. The increase in stiffness as the number of cells increases was also observed experimentally in similar structures of neo-Hookean silicone rubber (figure A1 in the Appendix).

To verify how the stiffness of the deformed cell walls affects the behaviour of the overall structure, we compare the behaviour of the model structures under a fixed vertical tensile load applied at the top horizontal boundary, while the conditions at the remaining boundaries

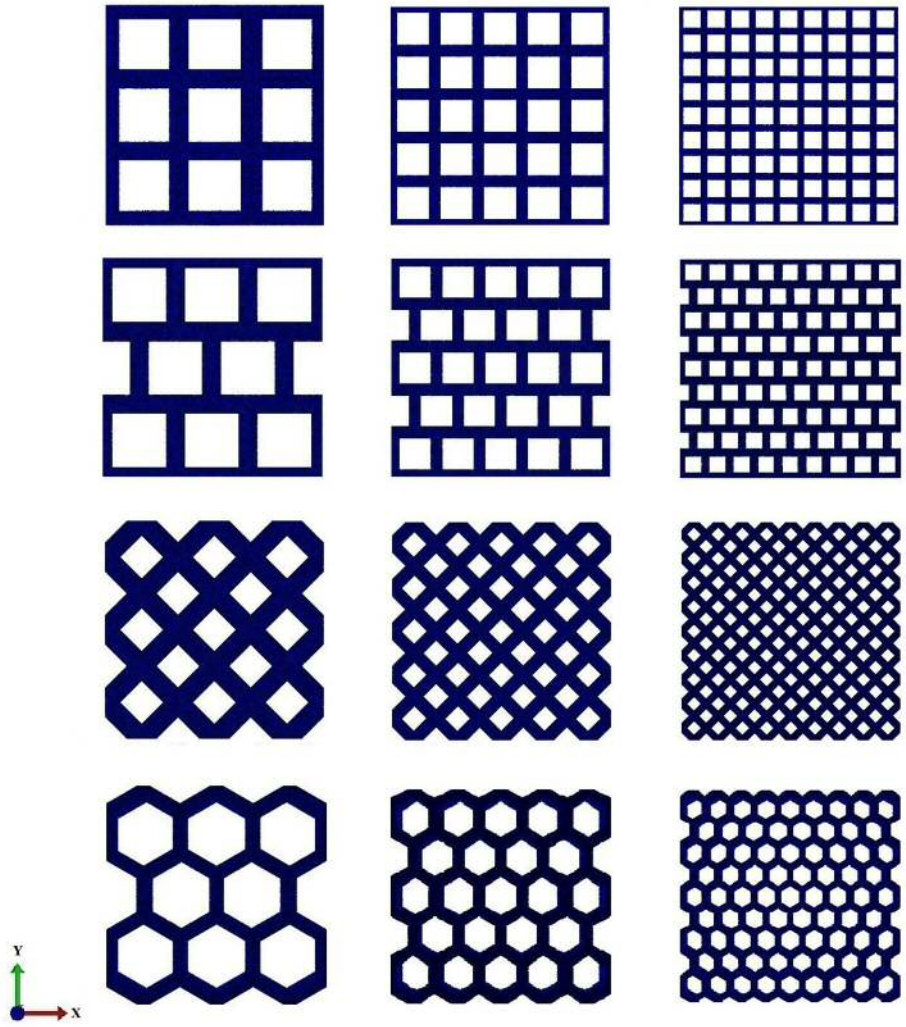

Figure 4.4.1: Undeformed model structures with stacked (top row), staggered (middle top row), diamond (middle bottom row), and hexagon (bottom row) cell geometry, and 3×3 (left column), 5×5 (middle column), and 9×9 (right column) cells.

Table 4.4.1: Vertical displacement under applied tensile force of 100 N at the top horizontal boundary for cellular structures of NH material with different number of cells and fixed material volume.

Cellular Structure	Number of Cells	Vertical Displacement
Stacked Cells	3×3	0.4914
	5×5	0.4428
	9×9	0.4061
Staggered Cells	3×3	0.6707
	5×5	0.5941
	9×9	0.4347

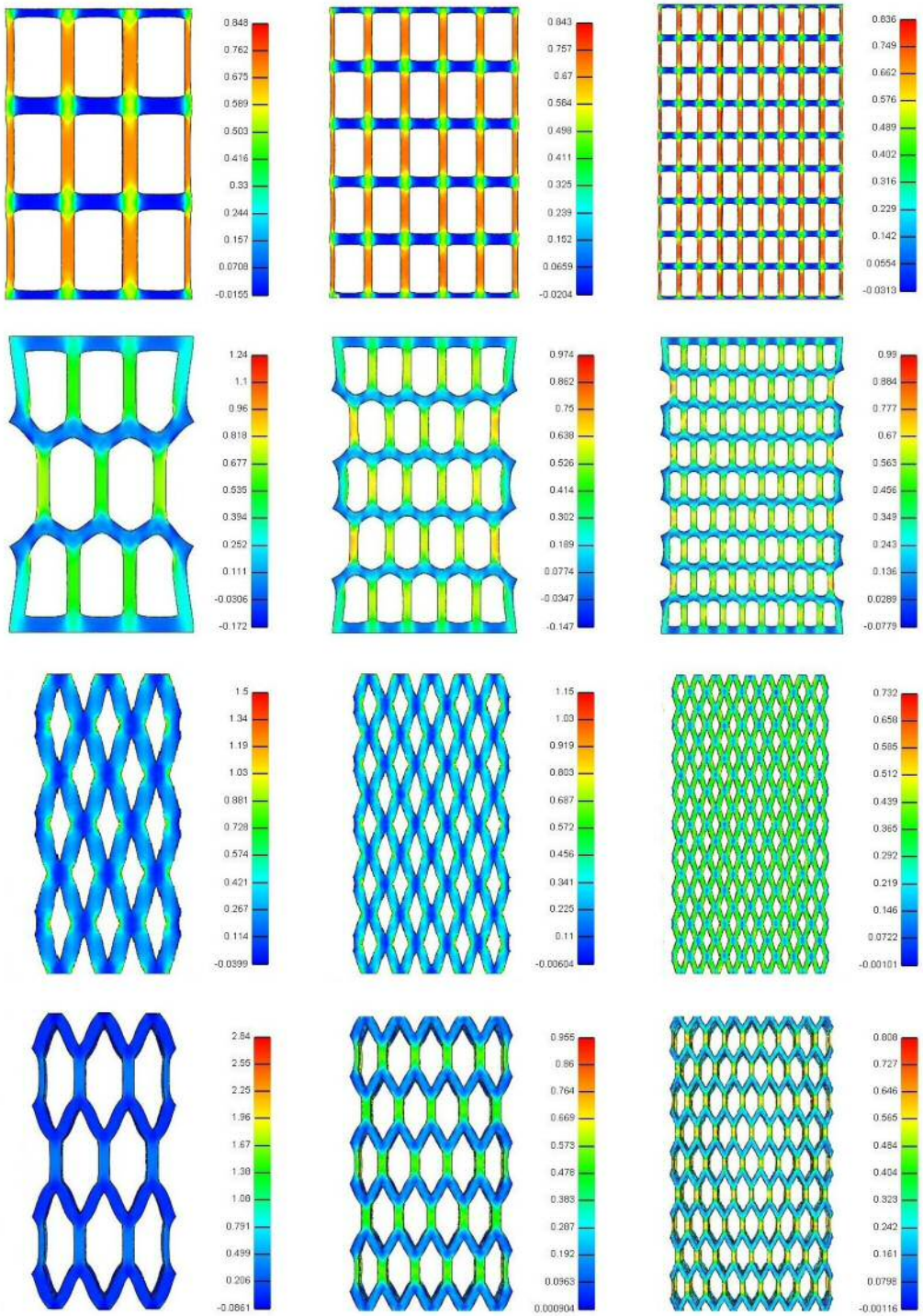

Figure 4.4.2: FEBio simulations of deformed structures with stacked (top row), staggered (middle top row), diamond (middle bottom row), and hexagon (bottom row) cell geometry, and 3×3 (left column), 5×5 (middle column), and 9×9 (right column) cells of NH material subject to 50% stretch in the vertical direction, showing the non-homogeneous Green-Lagrange strains in the first principal (vertical) direction.

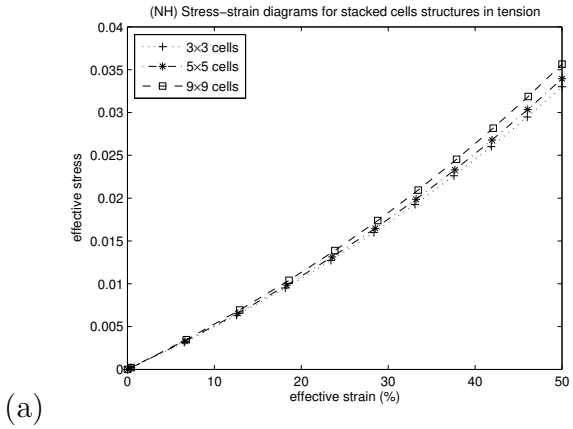

(a)

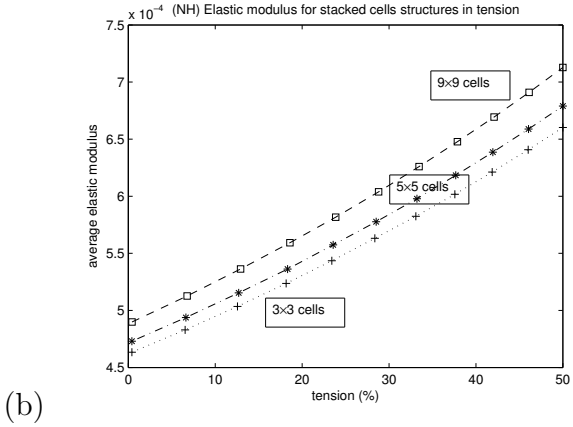

(b)

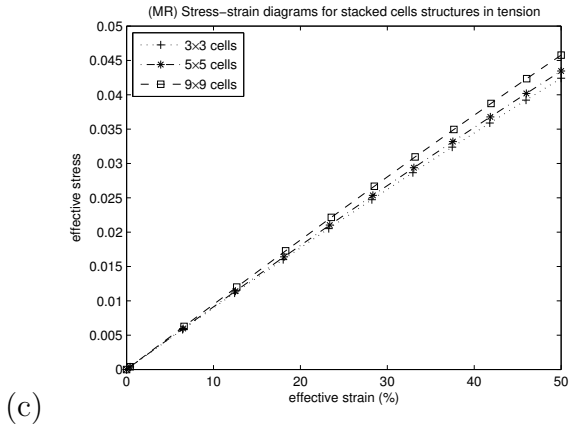

(c)

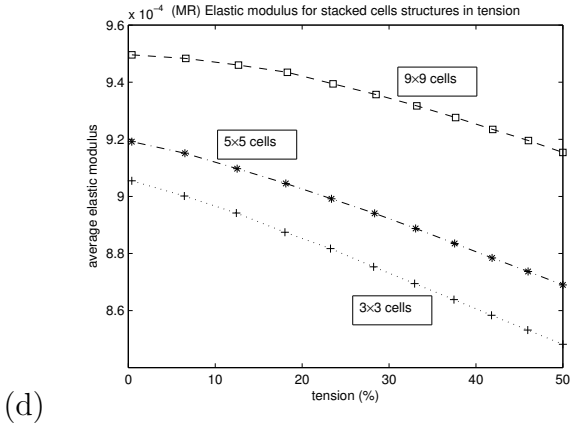

(d)

Figure 4.4.3: (a,c) Mean effective Cauchy stress (MPa) and (b,d) nonlinear elastic modulus (MPa) *vs.* mean effective logarithmic strain for stacked cells structures of (a,b) NH and (c,d) MR material with different number of cells and fixed material volume.

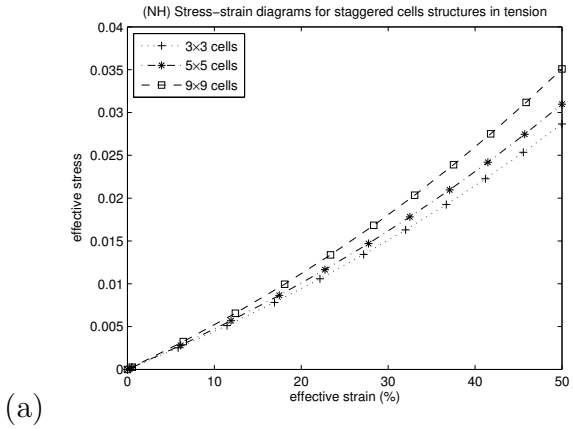

(a)

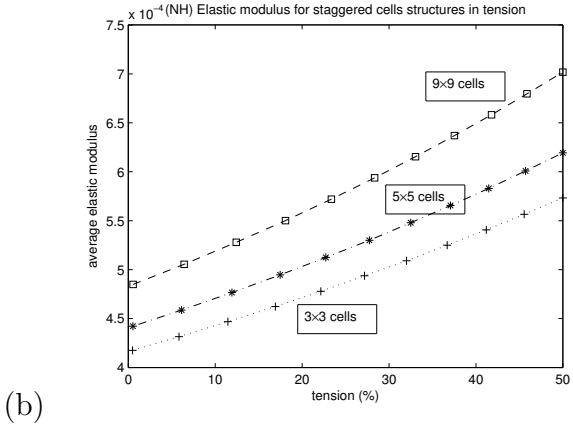

(b)

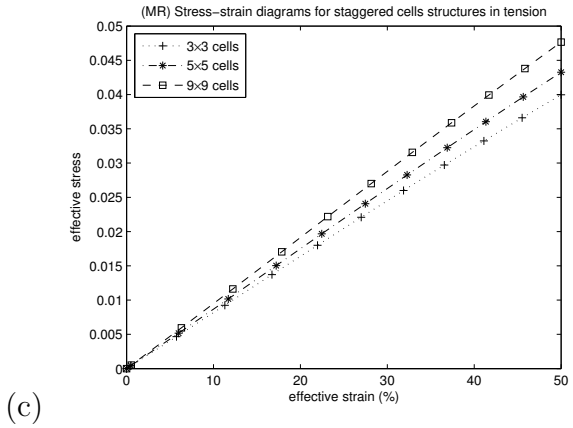

(c)

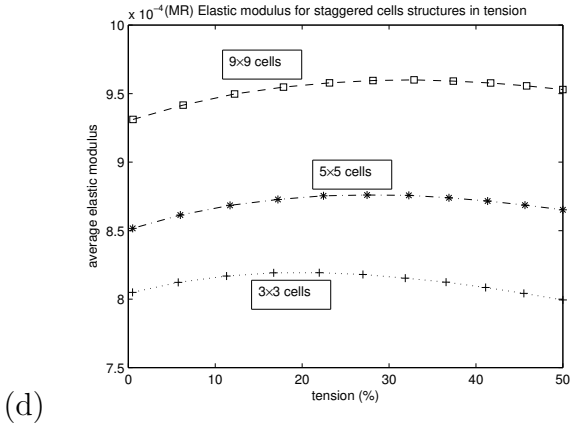

(d)

Figure 4.4.4: (a,c) Mean effective Cauchy stress (MPa) and (b,d) nonlinear elastic modulus (MPa) *vs.* mean effective logarithmic strain for staggered cells structures of (a,b) NH and (c,d) MR material with different number of cells and fixed material volume.

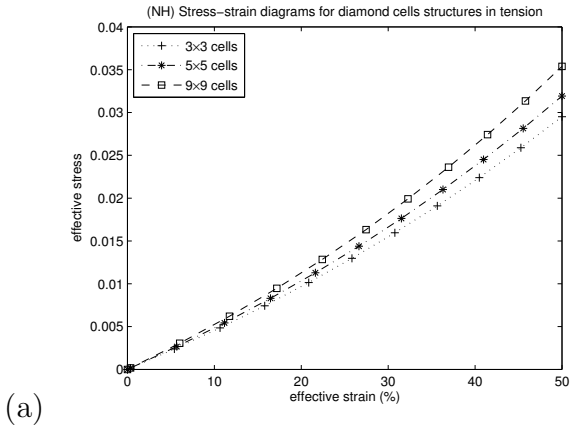

(a)

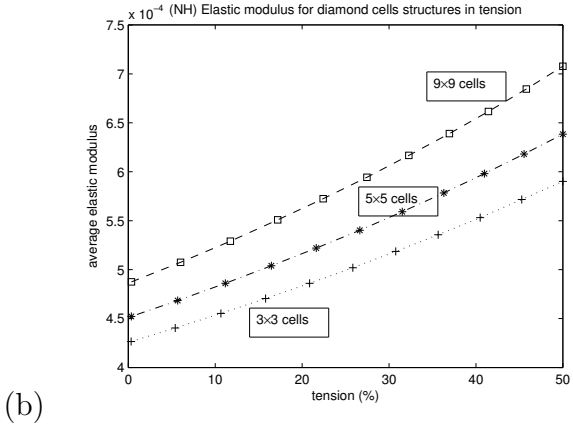

(b)

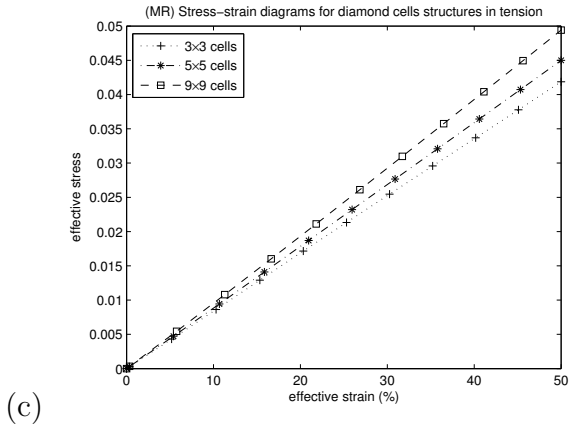

(c)

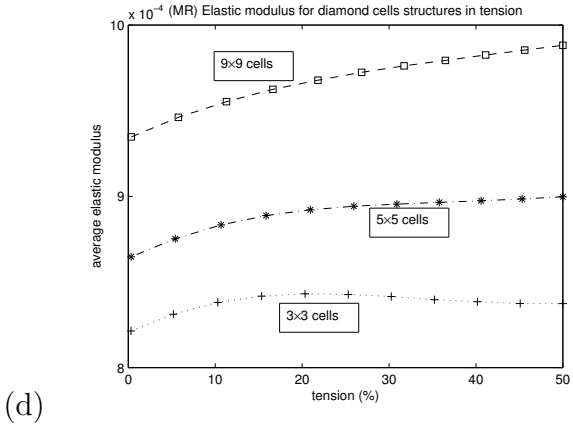

(d)

Figure 4.4.5: (a,c) Mean effective Cauchy stress (MPa) and (b,d) nonlinear elastic modulus (MPa) *vs.* mean effective logarithmic strain for diamond cells structures of (a,b) NH and (c,d) MR material with different number of cells and fixed material volume.

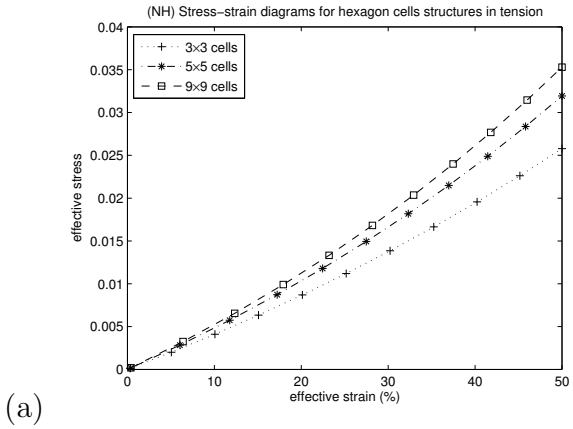

(a)

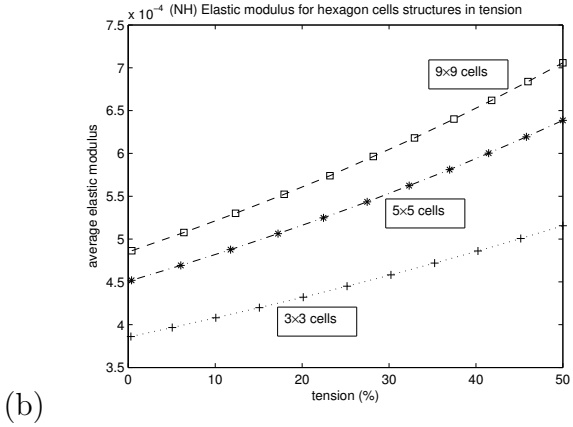

(b)

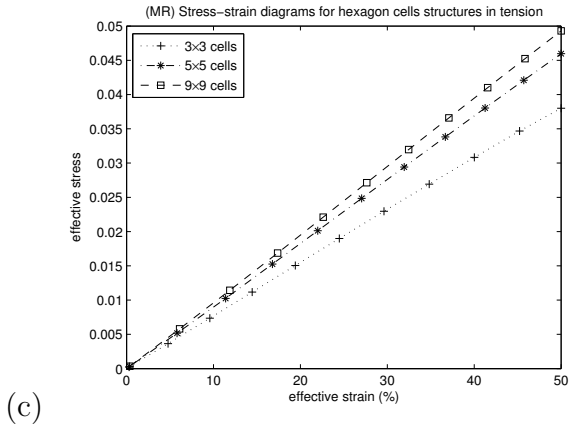

(c)

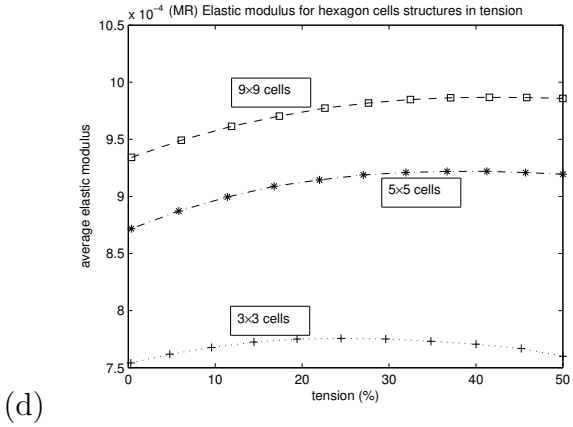

(d)

Figure 4.4.6: (a,c) Mean effective Cauchy stress (MPa) and (b,d) nonlinear elastic modulus (MPa) *vs.* mean effective logarithmic strain for hexagon cells structures of (a,b) NH and (c,d) MR material with different number of cells and fixed material volume.

are as before. The corresponding values for the vertical displacements of each structure are recorded in table 4.4.1, and confirm that, under the same vertical force, the structures with fewer and larger cells will deform more than those with smaller and more numerous cells.

The results obtained for the structures with increasing wall thickness and with an increasing number of cells, respectively, imply that, for cellular structures with similar cell geometries, if the number of cells increases while the wall thickness is fixed, then the nonlinear elastic modulus in the walls increases with the number of cells. This result is consistent with the classical result that the elastic modulus in a cellular structure increases as the ratio between the thickness and the length of the cell walls increases (see [48,49]). However, for cellular structures of nonlinear elastic material, the nonlinear elastic modulus may also increase if the cell size decreases while both the ratio between the thickness and the length of the cell walls and the total material volume remain fixed, as shown by the computed models with stacked and diamond cells.

In finitely deformed structures, the increase in the nonlinear elastic modulus is due to the enhanced elasticity of the cell walls when more material is added or when the same elastic material is distributed more uniformly throughout the structure, activating the elasticity of the hyperelastic walls. This type of elastic responses is similar to that obtained in the case when the cells are filled with a softer elastic core, where the elasticity of the deforming walls is activated and the walls stiffen due to the contact with the cell core.

4.5 Summary

In this chapter, for computational models made from different hyperelastic materials, our numerical results show that the nonlinear elastic modulus of the cell walls in the direction of the applied force is increased by increasing: (i) the thickness of the cell walls when the number of cells is fixed, (ii) the number of cells when the overall volume of cell wall material in the structure remains fixed, or (iii) the elastic modulus of the cell core. This is in agreement with the analytical results for the exact deformations from the previous chapter, and may be regarded as an extension of those results to the computer model structures. In all cases, the increase in the nonlinear elastic modulus is due to the enhancement of the elastic behaviour of the deforming cell walls when more material is added or if the same solid material is distributed more uniformly throughout the structure, and also when the cells are filled. Due to its monotonic behaviour, the nonlinear elastic modulus investigated here can be taken as indicative for finding the optimum wall thickness, number of cells, or cell pressure in similar structures.

Chapter 5

Nonlinear Poisson effects

5.1 Introduction

For an elastic material which is extended in one direction to a strain E_1 and deforms freely in the orthogonal direction to a strain E_2, the Poisson's ratio can be defined as $\nu = -E_2/E_1$. However, while for infinitesimal strains, the Poisson's ratio is a constant, for large strains, this ratio is usually a non-constant function of the deformation, as shown in [10]. The deformation of cellular bodies under external loading is typically non-homogeneous, due to both the cell wall material and the individual cell geometry. In [84], for periodic cellular structures of nonlinear hyperelastic material with square, diamond, and hexagonal cell geometry, it was demonstrated both analytically and numerically that, if a structure contains walls which are sheared under the applied tensile load, then the *nonlinear Poisson's ratio* computed as the negative quotient of the mean value of the logarithmic horizontal strain to that of the logarithmic vertical strain in the solid walls decreases as the vertical tension increases. The decrease in the nonlinear Poisson's ratio was also observed in recent experimental test for similar structures of neo-Hookean silicone rubber (figure A7 in the

Appendix). In this chapter, we show how the nonlinear Poisson's ratio in the cell walls may change with: (i) the wall thickness and (ii) the number of cells when the total volume of solid material in the structure remains fixed.

In Section 5.2, the nonlinear Poisson's ratio is computed and analysed locally for a cuboid wall which is sheared under the tensile loading applied at the outer boundaries of the structure; in Section 5.3, numerical results for the nonlinear Poisson's ratio obtained when the thickness of the cell walls increases and when the number of cells increases while the material volume of the cell walls is preserved are presented and discussed.

5.2 Sheared walls

In this section, following the analysis in [84], where cell walls which were sheared while a cellular structure is stretched were identified as causing a decrease in the nonlinear Poisson's ratio, we consider two generic large shear deformations of a cuboid cell wall of homogeneous isotropic nonlinear hyperelastic material.

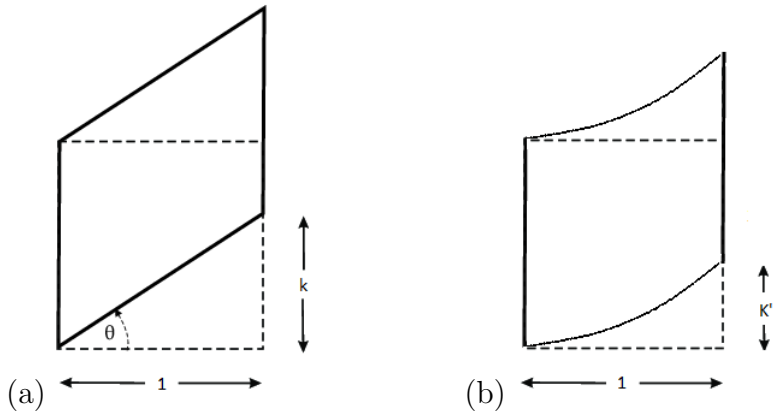

Figure 5.2.1: Schematics of cross-section of unit cube (dashed line) deformed by (a) simple or (b) generalised shear (continuous line).

Simple shear superposed on axial stretch. The classical problem of simple shear involves finite plane deformations of a rectangular section of a material in which straight lines parallel to, say the Y-axis, are displaced relative to one another in the Y-direction, but remain straight and parallel in the deformed body (figure 5.2.1 (a)). We consider a rectangular wall deformed by the following simple shear super-posed on triaxial stretch

$$x = aX, \qquad y = kaX + bY, \qquad z = \frac{Z}{ab}, \tag{5.2.1}$$

where (x, y, z) and (X, Y, Z) are the Cartesian coordinates for the deformed and the reference configuration, respectively, and a, b and k are positive constants [86, 108]. For the deformation (5.2.1), the gradient is equal to

$$\mathbf{F} = \begin{bmatrix} a & 0 & 0 \\ ak & b & 0 \\ 0 & 0 & 1/(ab) \end{bmatrix},$$

and the right Cauchy-Green tensor takes the form

$$\mathbf{C} = \mathbf{F}^T\mathbf{F} = \begin{bmatrix} a^2(1+k^2) & abk & 0 \\ abk & b^2 & 0 \\ 0 & 0 & 1/(a^2b^2) \end{bmatrix}.$$

Assuming that the cell wall belongs to a cellular structure which is stretched in the Y-direction, we can define the nonlinear Poisson's ratio throughout the structure as the negative quotient of the logarithmic

strain in the X-direction to the logarithmic strain in the Y-direction

$$\nu_C = -\frac{\ln C_{11}^{1/2}}{\ln C_{22}^{1/2}}. \tag{5.2.2}$$

Then, for the cell wall deformed by (5.2.1), the nonlinear Poisson's ratio (5.2.2) is equal to

$$\nu_C = -\frac{\ln\left[a^2\left(1+k^2\right)\right]}{\ln b^2} = -\frac{\ln a^2}{\ln b^2} - \frac{\ln\left(1+k^2\right)}{\ln b^2}, \tag{5.2.3}$$

Assuming that a and b are fixed and $0 < a < 1 < b$, this ratio decreases as the parameter k increases.

Generalised shear superposed on axial stretch. In the case of generalised shear deformation, the straight lines parallel to the Y-axis remain straight and parallel. For a Mooney-Rivlin material [92, 110], the straight lines parallel to the X-axis deform in the shape of a quadratic parabola (figure 5.2.1) [51, pp. 127-129]. For compressible isotropic materials, in the absence of body forces, the generalised shear reduces to a simple shear deformation [29]. These results can be proven as follows. We consider the following shear deformation

$$x = X, \qquad y = K(X) + Y, \qquad z = Z, \tag{5.2.4}$$

where K is a general function to be determined. For the deformation (5.2.4), the gradient is equal to

$$\mathbf{F} = \begin{bmatrix} 1 & 0 & 0 \\ K' & 1 & 0 \\ 0 & 0 & 1 \end{bmatrix},$$

where K' is the derivative of K with respect to X. By the represen-

tation (2.2.3), the non-zero components of the corresponding Cauchy stress tensor take the form

$$\begin{aligned}
\sigma_{11} &= -p + \beta_1 + \beta_{-1}\left[1 + (K')^2\right], \\
\sigma_{22} &= -p + \beta_1\left[1 + (K')^2\right] + \beta_{-1}, \\
\sigma_{12} &= (\beta_1 - \beta_{-1})K', \\
\sigma_{33} &= -p + \beta_1 + \beta_{-1}.
\end{aligned} \tag{5.2.5}$$

For a cuboid of general non-hyperelastic material, in the absence of body forces, by the equilibrium equation (2.3.1), the non-zero components of the Cauchy stress satisfy

$$\begin{aligned}
\frac{\partial \sigma_{11}}{\partial x} + \frac{\partial \sigma_{12}}{\partial y} &= 0, \\
\frac{\partial \sigma_{12}}{\partial x} + \frac{\partial \sigma_{22}}{\partial y} &= 0, \\
\frac{\partial \sigma_{33}}{\partial z} &= 0.
\end{aligned} \tag{5.2.6}$$

In the particular case when the material is described by the Mooney-Rivlin model (2.2.12), by (2.2.2), β_1 and β_{-1} are constants, and substitution of (5.2.5) in (5.2.6) yields

$$\begin{aligned}
-\frac{\partial p}{\partial x} + 2\beta_{-1}K'K'' &= 0, \\
-\frac{\partial p}{\partial y} + (\beta_1 - \beta_{-1})K'' &= 0, \\
-\frac{\partial p}{\partial z} &= 0,
\end{aligned} \tag{5.2.7}$$

where K'' denotes the second derivative of K with respect to X. From the third equation in (5.2.7) we deduce that p is independent of z, i.e., $p = p(x, y)$, and differentiating the first equation with respect to y and

the second equation with respect to x implies

$$\frac{\partial^2 p}{\partial x \partial y} = 0,$$
$$\frac{\partial^2 p}{\partial x \partial y} = (\beta_1 - \beta_{-1})K''',$$

where K''' denotes the third derivative of K with respect to X. Hence $K''' = 0$, i.e., K'' is constant. We distinguish the following two cases:

(i) If $K'' = 0$, then $K' = k_1$ is constant and $K = k_1 X + k_0$ is a linear function of X, where k_1 and k_0 are arbitrary constants. Assuming that, during the deformation, the points of coordinates $(0, Y, 0)$ remain fixed and those of coordinates $(1, Y, 0)$ are deformed into $(1, Y + k, 0)$ implies $K(0) = 0$ and $K(1) = k$, i.e., $k_0 = 0$ and $k_1 = k$, and the deformation (5.2.4) reduces to a simple shear with $K = kX$.

(ii) If $K'' = 2k_2 \neq 0$, then $K' = 2k_2 X + k_1$ is linear, and $K = k_2 X^2 + k_1 X + k_0$ is a quadratic function of X, where k_1 and k_0 are arbitrary constants. Assuming that the points of coordinates $(0, Y, 0)$ remain fixed and those of coordinates $(1, Y, 0)$ are deformed into $(1, Y + k, 0)$ implies $k_0 = 0$ and $k_1 + k_2 = k$.

Next, we analyse the nonlinear Poisson's ratio under the following generalised shear super-posed on triaxial stretch, where $k_1 = 0$,

$$x = aX, \qquad y = K(aX) + bY, \qquad z = \frac{Z}{ab}, \tag{5.2.8}$$

where $K(aX) = ka^2 X^2$, and a and k are constants. The gradient of

the deformation (5.2.8) is equal

$$\mathbf{F} = \begin{bmatrix} a & 0 & 0 \\ 2a^2kX & b & 0 \\ 0 & 0 & 1/(ab) \end{bmatrix},$$

and the right Cauchy-Green tensor takes the form

$$\mathbf{C} = \mathbf{F}^T\mathbf{F} = \begin{bmatrix} a^2\left(1+4k^2a^2X^2\right) & 2ka^2bX & 0 \\ 2ka^2bX & b^2 & 0 \\ 0 & 0 & 1/(a^2b^2) \end{bmatrix}.$$

In this case, the nonlinear Poisson's ratio (5.2.2) is defined as follows

$$\nu_C = -\frac{\ln\left[a^2\left(1+4k^2a^2X^2\right)\right]}{\ln b^2} = -\frac{\ln a^2}{\ln b^2} - \frac{\ln\left(1+4k^2a^2X^2\right)}{\ln b^2}. \quad (5.2.9)$$

Hence, if a and b are fixed and $0 < a < 1 < b$, then ν_C decreases as the parameter $k > 0$ increases, and decreases also as $X > 0$ increases.

Influence of wall thickness. To compare the Poisson's ratio of a thin wall with that of a thick wall under the same shear deformation (5.2.4), we assume that the thin wall occupies the reference domain $[X_1, X_2] \times [-Y_0, Y_0] \times [-Z_0, Z_0]$ and the thick wall occupies the reference domain $[X_1', X_2] \times [-Y_0, Y_0] \times [-Z_0, Z_0]$, such that $X_1' < X_1$. By calculations similar to those for the mean elastic modulus in Chapter

3, it follows that

$$
\begin{aligned}
&\frac{1}{X_2-X_1}\int_{X_1}^{X_2}\nu_C dX-\frac{1}{X_2-X_1'}\int_{X_1'}^{X_2}\nu_C dX\\
&=\frac{1}{X_2-X_1}\int_{X_1}^{X_2}\nu_C dX-\frac{1}{X_2-X_1'}\int_{X_1}^{X_2}\nu_C dX-\frac{1}{X_2-X_1'}\int_{X_1'}^{X_1}\nu_C dX\\
&=\frac{X_1-X_1'}{(X_2-X_1)(X_2-X_1')}\int_{X_1}^{X_2}\nu_C dX-\frac{1}{X_2-X_1'}\int_{X_1'}^{X_1}\nu_C dX\\
&=\frac{X_1-X_1'}{X_2-X_1'}\left(\frac{1}{X_2-X_1}\int_{X_1}^{X_2}\nu_C dX-\frac{1}{X_1-X_1'}\int_{X_1'}^{X_1}\nu_C dX\right)\\
&<\frac{X_1-X_1'}{X_2-X_1'}\left[\frac{1}{X_2-X_1}\int_{X_1}^{X_2}\nu_C(X_1) dX-\frac{1}{X_1-X_1'}\int_{X_1'}^{X_1}\nu_C(X_1) dX\right]\\
&=0.
\end{aligned}
$$

The above inequality holds since ν_C defined by (5.2.9) is a decreasing function of X, and therefore $\nu_C(X) < \nu_C(X_1)$ for all $X \in (X_1, X_2]$ and $\nu_C(X) > \nu_C(X_1)$ for all $X \in [X_1', X_1)$.

Influence of number of walls when the total material volume is fixed. Under the same generalised shear deformation (5.2.4), we further compare the Poisson's ratio of two thin walls deforming separately with that of a single thick wall, such that the total volume of the two thin walls is equal to that in the thick wall. In this case, we assume that the thin walls are equal in size and that a thin wall occupies the reference domain $[X_1, X_2] \times [-Y_0, Y_0] \times [-Z_0, Z_0]$, while the thick wall occupies the reference domain $[X_1, X_2'] \times [-Y_0, Y_0] \times [-Z_0, Z_0]$, such that $X_2' - X_1 = 2(X_2 - X_1)$. By calculations similar to those for

the mean elastic modulus in Chapter 3, we obtain

$$
\begin{aligned}
&\frac{1}{X_2 - X_1}\int_{X_1}^{X_2} \nu_C dX - \frac{1}{X_2' - X_1}\int_{X_1}^{X_2'} \nu_C dX \\
&= \frac{1}{X_2 - X_1}\int_{X_1}^{X_2} \nu_C dX - \frac{1}{X_2' - X_1}\int_{X_1}^{X_2} \nu_C dX - \frac{1}{X_2' - X_1}\int_{X_2}^{X_2'} \nu_C dX \\
&= \frac{1}{2(X_2 - X_1)}\int_{X_1}^{X_2} 2\nu_C dX - \frac{1}{2(X_2 - X_1)}\int_{X_1}^{X_2} \nu_C dX \\
&- \frac{1}{2(X_2 - X_1)}\int_{X_2}^{X_2'} \nu_C dX \\
&= \frac{1}{2(X_2 - X_1)}\int_{X_1}^{X_2} \left[\nu_C(X) - \nu_C(X + X_2 - X_1)\right] dX \\
&> 0.
\end{aligned}
$$

The above inequality holds since ν_C defined by (5.2.9) is a decreasing function of X, and therefore $\nu_C(X) > \nu_C(X + X_2 - X_1)$.

The analysis extends to the case with $n > 2$ cell walls. For example, we compare the Poisson's ratio of three thin walls with reference domain $[X_1, X_2] \times [-Y_0, Y_0] \times [-Z_0, Z_0]$ with the Poisson's ratio of two thicker walls with reference domain $[X_1, X_2'] \times [-Y_0, Y_0] \times [-Z_0, Z_0]$, such that $2(X_2' - X_1) = 3(X_2 - X_1)$. Then

$$
\begin{aligned}
&\frac{1}{X_2 - X_1}\int_{X_1}^{X_2} \nu_C dX - \frac{1}{X_2' - X_1}\int_{X_1}^{X_2'} \nu_C' dX \\
&= \frac{1}{X_2 - X_1}\int_{X_1}^{X_2} \nu_C dX - \frac{1}{X_2' - X_1}\int_{X_1}^{X_2} \nu_C' dX - \frac{1}{X_2' - X_1}\int_{X_2}^{X_2'} \nu_C' dX \\
&= \frac{1}{3(X_2 - X_1)}\int_{X_1}^{X_2} 3\nu_C dX - \frac{1}{3(X_2 - X_1)}\int_{X_1}^{X_2} 2\nu_C dX \\
&- \frac{1}{3(X_2 - X_1)}\int_{X_2}^{X_2'} 2\nu_C' dX \\
&= \frac{1}{3(X_2 - X_1)}\int_{X_1}^{X_2} \left[\nu_C(X) - \nu_C(X_2 + (X - X_1)/2)\right] dX \\
&> 0.
\end{aligned}
$$

Hence the mean Poisson's ratio increases as the number of thin walls increases if the total material volume remains unchanged.

5.2.1 Optimisation problem

Since the nonlinear Poisson's ratio defined by (5.2.2) increases with the wall thickness and with the number of walls increases while the total volume of elastic material is fixed, we can employ this ratio to find the minimum wall thickness or the minimum number of walls under the generalised shear superposed on axial stretch (5.2.8), where $0 < a < 1 < b$ and $k > 0$. We formulate the following optimisation problem [41]

$$\text{find } X_2 = \inf V, \qquad V = \{X > X_1 \mid \nu_C(X) \leq C\},$$

where $C > 0$ is the given threshold. Since

$$\nu_C(X) = -\frac{\ln\left[a^2\left(1 + 4a^2k^2X^2\right)\right]}{\ln b^2} \leq C,$$

for all X satisfying

$$a^2\left(1 + 4a^2k^2X^2\right) \geq b^{-2C},$$

or equivalently, for all X, such that

$$X^2 \geq \frac{1 - a^2b^{2C}}{4a^4k^2b^{2C}},$$

it follows that V is bounded and non-empty, hence the optimisation problem has a solution.

5.3 Numerical results

The finite element models analysed here are the same honeycomb-like structures with square, diamond-shape, and hexagonal cells described in the previous chapter. Each structure is deformed by imposing the following boundary conditions: the lower external horizontal face is fixed in the second/vertical/Y-direction and free to slide in the first/horizontal/X-direction and in the third/out-of-plane/Z-direction; the upper external horizontal face is subject to a prescribed vertical displacement and is free to slide horizontally and out-of-plane; and the remaining external and internal cell faces deform freely. The numerical simulations represented in figures 4.3.2 and 4.4.2 show that, for every structure, the deformation is always symmetric with respect to the vertical axis, and that the initially horizontal walls of the staggered cells bend and the inclined walls of the diamond and hexagon cells are sheared. While the approximation of individual walls deforming within such structures is not unique, it is appropriate to examine theoretically the sheared walls by a generalised shear deformation as discussed in the previous section. For the model structures, the nonlinear Poisson's ratio was computed as the negative quotient of the average value of the horizontal to the vertical component of the logarithmic strain $\ln \mathbf{C}^{1/2}$, where $\mathbf{C}$ is the right Cauchy-Green tensor and the logarithmic function is applied component-wise. The average value was calculated as the sum of the values on all the finite elements divided by the number of elements. Again we remark that, in the finite element simulations, the resulting nonlinear elastic deformations of the cell walls are generally more complex than the exact deformations studied analytically.

5.3.1 Influence of cell wall thickness

For the structures of NH or MR material shown in the undeformed state in figure 4.3.1 and subject to uniaxial extension as illustrated in figure 4.3.2, the mean values of the nonlinear Poisson's ratio are represented in figures 5.3.1, 5.3.2, 5.3.3, and 5.3.4, respectively. The numerical results indicate that the Poisson's ratio decreases as the deformation increases and increases as the thickness of cell walls increases. In particular, for the structures with diamond and hexagon cells, we can approximate theoretically the shearing of thin and thick walls by the generalised shear deformation analysed in the previous section. Analytically, we assumed that thin wall occupied initially a reference domain $[X_1, X_2] \times [-Y_0, Y_0] \times [-Z_0, Z_0]$ and the thick wall occupied the reference domain $[X_1', X_2] \times [-Y_0, Y_0] \times [-Z_0, Z_0]$, such that $X_1' < X_1$. Applying the same general shear deformation to both walls, we found that the mean Poisson's ratio was greater for the thick wall than for the thin wall. This is in agreement with the numerical results plotted in figures 5.3.3 and 5.3.4, respectively.

5.3.2 Influence of cell density

For the structures of NH or MR material with an increasing number of cells shown in the undeformed state in figure 4.4.1 and subject to uniaxial extension as indicated in figure 4.4.2, the corresponding values of the mean Poisson's ratio are plotted in figures 5.3.5, 5.3.6, 5.3.7, and 5.3.8. In this case, the computed results suggest that the Poisson's ratio decreases as the deformation increases and increases as the number of cells increases. In particular, for the model structures with diamond and hexagon cells, we can approximate theoretically the

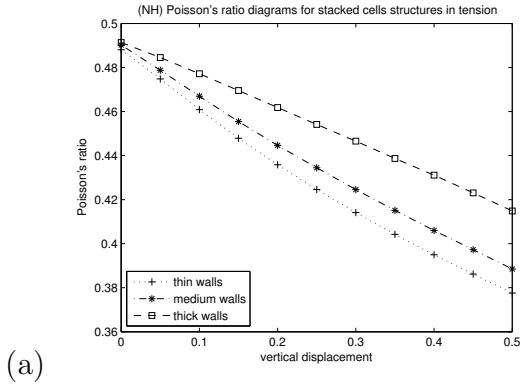

(a)

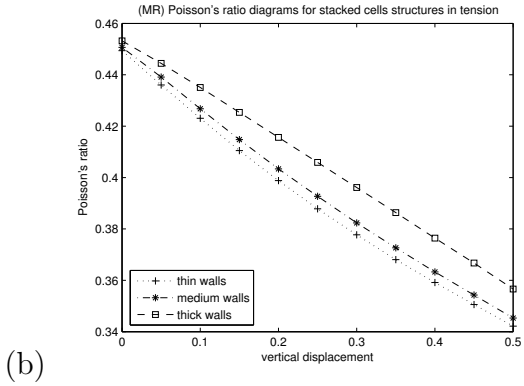

(b)

Figure 5.3.1: Nonlinear Poisson's ratio *vs.* vertical displacement for stacked cells structures of (a) NH and (b) MR material with different cell wall thickness.

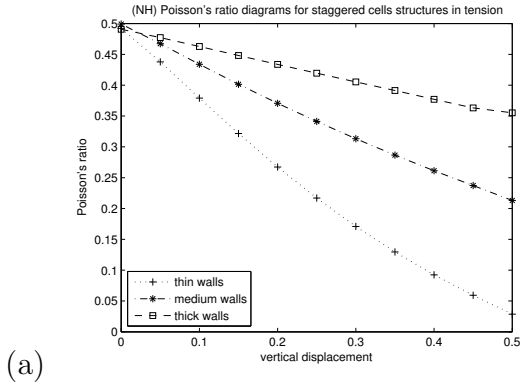

(a)

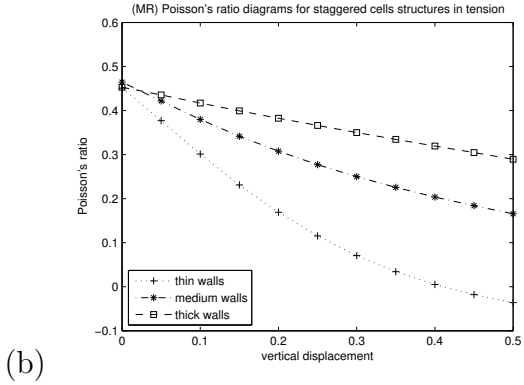

(b)

Figure 5.3.2: Nonlinear Poisson's ratio *vs.* vertical displacement for staggered cells structures of (a) NH and (b) MR material with different cell wall thickness.

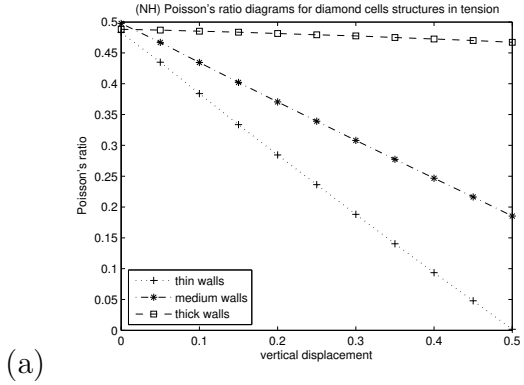

(a)

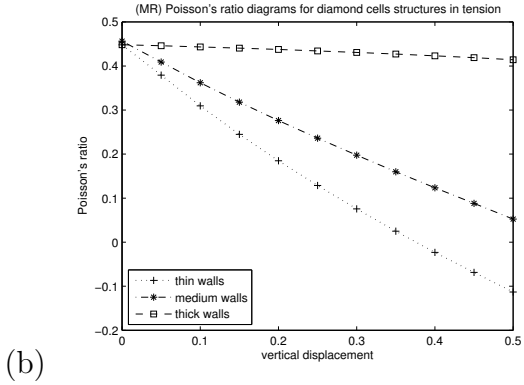

(b)

Figure 5.3.3: Nonlinear Poisson's ratio *vs.* vertical displacement for diamond cells structures of (a) NH and (b) MR material with different cell wall thickness.

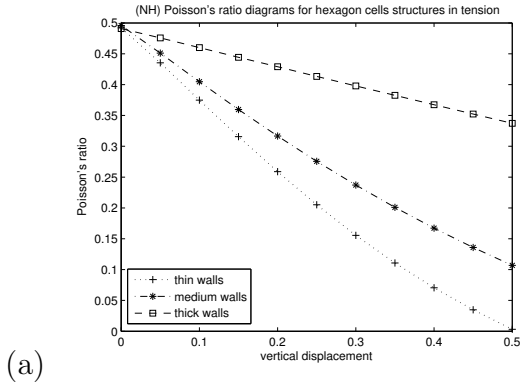

(a)

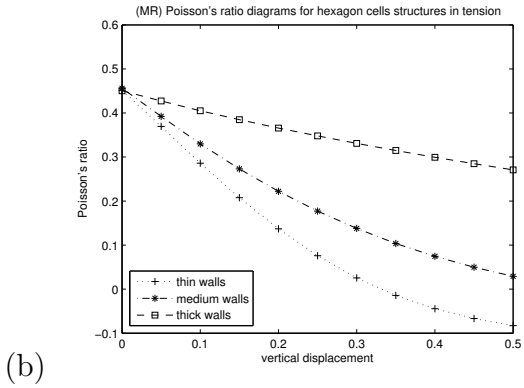

(b)

Figure 5.3.4: Nonlinear Poisson's ratio *vs.* vertical displacement for hexagon cells structures of (a) NH and (b) MR material with different cell wall thickness.

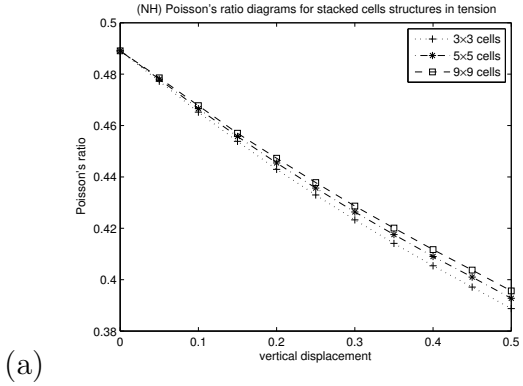

(a)

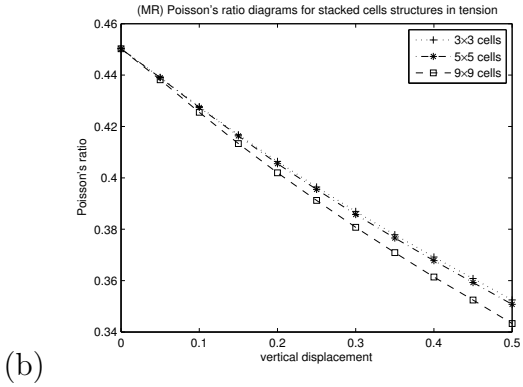

(b)

Figure 5.3.5: Nonlinear Poisson's ratio *vs.* vertical displacement for stacked cells structures of (a) NH and (b) MR material with different number of cells and fixed material volume.

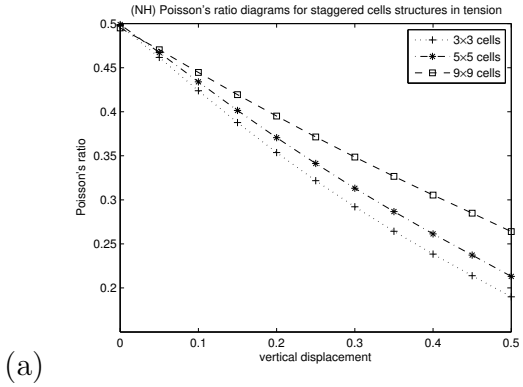

(a)

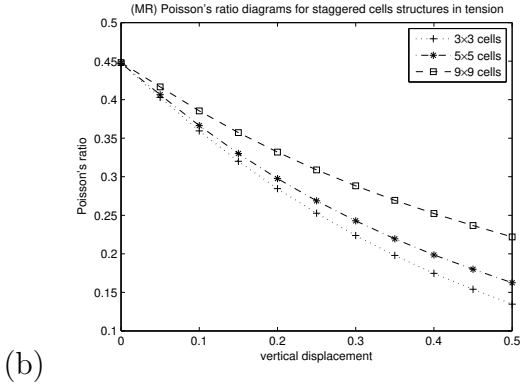

(b)

Figure 5.3.6: Nonlinear Poisson's ratio *vs.* vertical displacement for staggered cells structures of (a) NH and (b) MR material with different number of cells and fixed material volume.

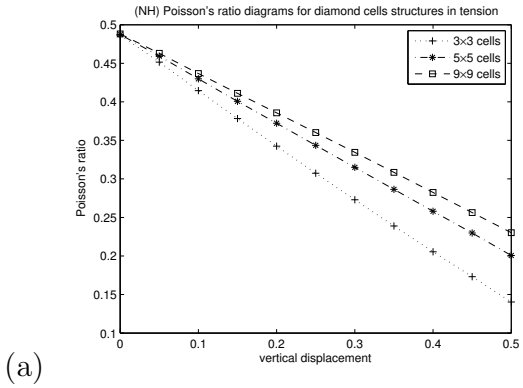

(a)

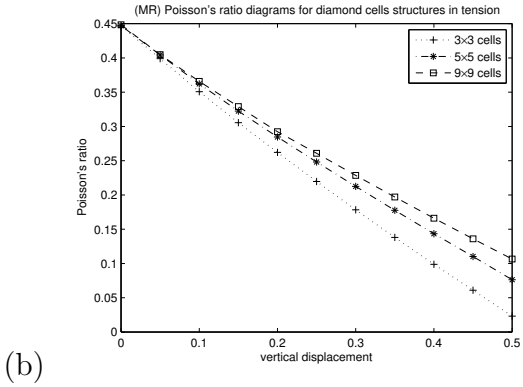

(b)

Figure 5.3.7: Nonlinear Poisson's ratio *vs.* vertical displacement for diamond cells structures of (a) NH and (b) MR material with different number of cells and fixed material volume.

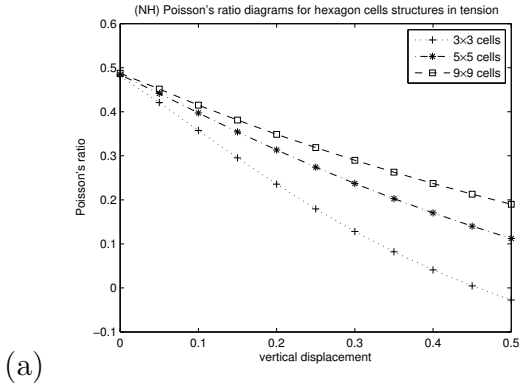

(a)

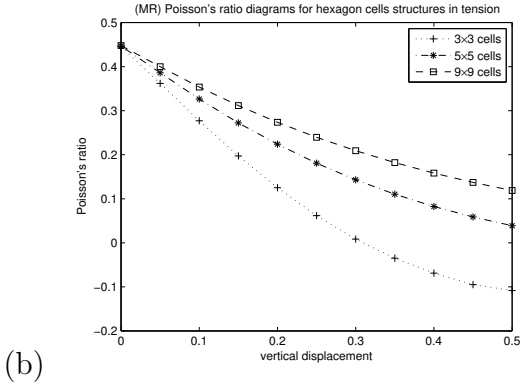

(b)

Figure 5.3.8: Nonlinear Poisson's ratio *vs.* vertical displacement for hexagon cells structures of (a) NH and (b) MR material with different number of cells and fixed material volume.

shearing of small and large walls by the generalised shear deformation analysed in the previous section. Analytically, we assumed that the small wall occupied initially a reference domain $[X_1, X_2] \times [-Y_0, Y_0] \times [-Z_0, Z_0]$ and the large wall occupied the reference domain $[X_1, X_2'] \times [-Y_0, Y_0] \times [-Z_0, Z_0]$, such that $X_2' - X_1 = 2(X_2 - X_1)$. Applying the same general shear deformation to both walls, we found that the mean Poisson's ratio was greater for the small walls than for the large wall. This is in agreement with the numerical results plotted in figures 5.3.7 and 5.3.8, respectively.

5.4 Summary

In this chapter, we investigated the Poisson effects in cellular structures of nonlinear hyperelastic material subject to large strain deformations, and analysed the physical properties generating them. Theoretically, we approximated the deformation of single cell walls which are sheared in the direction in which the structures are stretched with a simple or a generalised shear deformation, and obtained that the negative quotient of the logarithmic strain in the direction orthogonal to the shear direction to the logarithmic strain in the shear direction decreases as shearing increases: (i) decreases as the deformation decreases; (ii) is smaller for a single thick wall than for multiple thin walls made from the same volume of material; and (iii) increases as the number of thin walls increases while the volume of material remains unchanged. For finite element models of periodic cellular structures with rectangular, diamond, and hexagonal cell geometry, we found that, when a structure is subject to vertical extension, by computing the nonlinear Poisson's ratio as the negative quotient of the horizontal

to the vertical components of the logarithmic strain generated in the elastic walls, this ratio increases: (i) decreases as the deformation increases, and increases with (ii) the cell wall thickness and (iii) with the number of cells when the material volume is fixed. These results imply that, for cellular structures with similar cell geometries, if the number of cells increases while the wall thickness is fixed, then the apparet Poisson's ratio in the walls increases with the number of cells. Due to this monotonic behaviour, the nonlinear Poisson's ratio analysed here can be employed to find the optimum wall thickness or number of cells in similar structures.

Chapter 6

Conclusion and perspectives

6.1 Overview

Cellular bodies are strong, flexible structures made from seemingly fragile materials. Among the best known mechanical qualities of cellular structures are their high strength-to-weight ratio and energy absorption capacity, which arise from the inextricable relation between the geometric architecture and the nonlinear elastic responses of their constituents. In many cellular structures, during functional deformations, plastic damage or fracture rarely occurs, and the material recovers completely after large deformations. Such deformations can be reasonably treated within the theoretical framework of large strain elasticity, which provides a complete description of the elastic responses of a solid material under loading.

In this thesis, we showed how, for hyperelastic cellular bodies, several main factors determine the magnitude of the stress level in the cellular material, including the cell geometry, the cell wall thickness, and the presence of cell inclusions, and addressed the important question whether the same volume of material has the same effect when arranged as many cells or as fewer cells while the material volume

remains fixed. To achieve this, we identified two nonlinear constitutive parameters, namely a nonlinear elastic modulus and a nonlinear Poisson's ratio defined in terms of the large stresses and strains in the elastic cell walls, and investigated their utility in estimating how different competing factors contribute to the complex mechanical behaviour of these structures. For the numerical investigation of these nonlinear parameters, finite element models of representative structures with a small number of square, diamond, or hexagonal cells made from a nonlinear hyperelastic material were constructed.

Analytically, for a single cell wall of homogeneous, isotropic, incompressible, elastic material, subject to generic finite deformations, such as bending, straightening, or torsion, under certain restrictions, the nonlinear elastic modulus calculated as the ratio between the stress and the strain in the direction associated with the largest change of curvature is determined by: (i) the wall thickness, (ii) the number of cells, and (iii) the internal cell pressure, which when increased will cause the elastic modulus to increase. For a cellular structure which is extended in the vertical direction and contains walls that are inclined with respect to that direction, experimental and computational tests showed that the nonlinear Poisson's ratio defined as the negative quotient of the horizontal to the vertical strain decreases as the vertical extension increases. Theoretically, we further identified the inclination of the cell walls which are sheared while the cellular structure is stretched as contributing to the observed Poisson effect.

Numerically, we investigated periodic cellular structures with a small number of cells and different cell geometries, implemented within the Finite Elements for Biomechanics (FEBio) software (see supple-

mentary material for original source files). For the finite element models with neo-Hookean or Mooney-Rivlin cell wall material, we found that both the nonlinear elastic modulus calculated as the ratio between the mean effective stress and the mean effective logarithmic strain, and the nonlinear Poisson's ratio defined as the negative quotient of the mean value of the logarithmic horizontal strain to that of the logarithmic vertical strain in the solid walls while the structure is stretched vertically increase: (i) with the cell wall thickness and (ii) with the number of cells if the material volume in the structure is fixed. In addition, (iii) the nonlinear elastic modulus also increases as the modulus of the cell core increases. In all cases, the increase in the nonlinear elastic modulus is due to the enhancement of the elastic behaviour of the deforming cell walls when more material is added or if the same solid material is distributed more uniformly throughout the structure, and also when the cells are filled. Therefore the nonlinear elastic modulus and Poisson's ratio provide viable criteria for finding the optimum cell wall thickness, number of cells, and cell pressure in similar structures.

In the finite element simulations, the size of the cell and the size of the structure are comparable, and the nonlinear elastic effects are visible at the cell level and at the structural level simultaneously. We note that, at this scale, the resulting nonlinear elastic deformations of the cell walls in the model structures are generally more complex that the idealised deformations studied analytically for individual walls. Nevertheless, for the periodic structures with standard cell geometry and subject to uniaxial tension treated here, the deformation of the cell walls may be reasonably approximated as triaxial stretching (e.g., the

initially vertical walls of square or hexagonal cells), or bending (e.g., the initially horizontal walls of square cells in staggered distribution), or shearing (e.g., the inclined walls of diamond or hexagonal cells). In this case, our numerical results may be regarded as an extension of the analytical results.

In practice, the large deformations of many elastic solids are typically more complex, but the structures analysed here have the advantage that they can be studied systematically under large strains. In particular, our study offers important insight into the fundamental behaviour of cellular structures of nonlinear elastic material under large strains, and contributes to illuminate key mechanical effects that are not visible under small strains.

6.2 Future directions

The cell walls of plants and other biogenic cellular bodies represent a dynamic matrix whose composition, structure and function is required for all aspects of growth and development and for a variety of biotic and abiotic interactions through which they respond to their environment [17, 20, 26, 33, 46, 70, 71, 129, 145]. While new physical criteria associated with different stages of development or healing in natural structures are still to be identified, there is also a need for appropriate theoretical approaches to be developed that take into account the large stress and strain fields during physiological or pathological changes.

From the mathematical modelling perspective, cellular materials are hierarchical structures for which multi-scale models could capture the relation between the mechanical behaviour at the micro-scale, cell level, and the responses to loading at the macro-scale, structural level

[88, 89]. This could then be employed to show how the elasticity of the entire cellular structures is modified when the cells are filled with a compliant liquid or solid core, or when the cell walls become thicker or the number of cells increases.

Mathematical models that account for the attachment between cells, which in some structures are sufficiently weak so that cells separate (e.g., apples, pears) [18, 39, 55, 56, 63, 143], are also required for improved predictions of large distortions and failure in cellular structures [87].

Cellular materials are the subject of intensive research efforts in tissue engineering and regenerative applications, and the advent of 3D printing has led to increased interest in the optimal design of tissue scaffolds with well-defined, reproducible geometry. Engineered tissue scaffolds provide an environment for biological cells to grow and regenerate tissue, and their composition, micro-structure and mechanical properties play a critical role in the response of biological cells that migrate within them. In highly oriented tissues, such as nerve, ligament, muscle, and tendon, where tensile strength and stiffness are controlled by collagen fibers, geometrically controlled, honeycomb-like scaffolds also provide guidance cues for fiber orientation [16, 34, 35, 66, 104, 113, 126]. For these type of structures, the cell density and wall stiffness are key factors with implications for cell mechanotransduction [32, 36, 118, 140, 142, 144], which can be independently optimized to improve biological response [14, 45, 138].

Appendix A

Recent experimental evidence

This appendix contains some experimental evidence of nonlinear elastic responses for cellular structures with hyperelastic cell walls, courtesy of Dr Hayley Wyatt and Professor Sam Evans, who recently carried out physical tests at the School of Engineering, Cardiff University, inspired by the theoretical results of this thesis. Since the material and geometric properties of the tested structures are different from those in our finite element simulations, no attempt has been made to compare quantitatively the experimental results presented here with the computational results of this thesis. For meaningful comparisons, further computational modelling will be carried out, where the material and geometric parameters of the tested structures will be taken into account by the finite element simulations.

The physical structures tested experimentally were made from silicone rubber moulded with moulds manufactured by 3D printing at Cardiff School of Engineering. The silicone used was a neo-Hookean material with defined properties of 0.74 MPa for Youngs modulus and 0.48 for Poissons ratio, also manufactured at Cardiff School of Engineering. A combination of finite element modelling (FEM) and experimental work was conducted to investigate the effect of the number

of cells for a fixed volume of nonlinear hyperelastic material subject to large uniaxial tension (figure A1). Experimentally, digital image correlation (DIC) [38] was employed to investigate the behaviour of silicone structures of neo-Hookean material under tensile loading (see figure A2). The results from the DIC data showed similar displacement and strain maps when compared to the FEM data, as shown in figures A3, A4, A5. The nonlinear stiffening exhibited by the deformed structures are indicated in figure A6. The apparent Poisson's ratios exhibited by the deformed structures were also captured experimentally and indicated in figure A7.

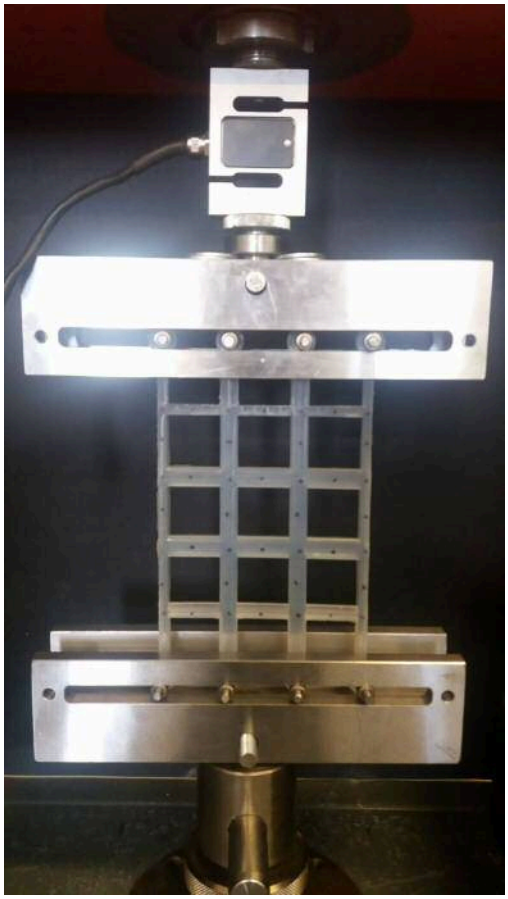

Figure A1: Sample cellular structure of neo-Hookean material in tensile testing.

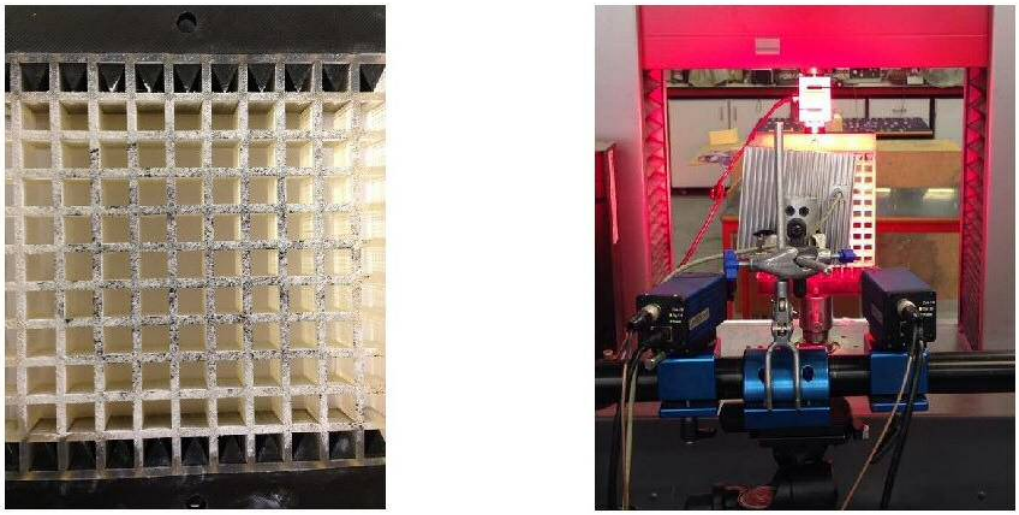

Figure A2: Sample cellular structure of neo-Hookean material used for tensile testing (left). The DIC set-up, with a two camera system used to capture 3D images and a light source providing homogeneous light to the specimen (right).

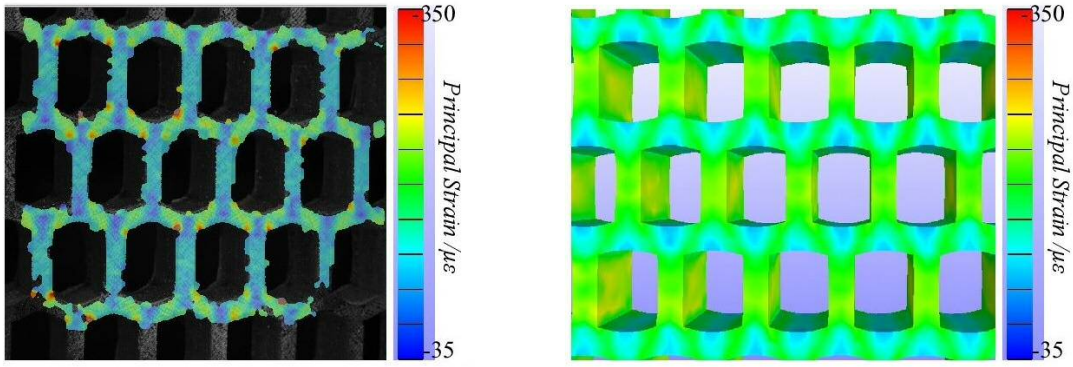

Figure A3: Example of DIC (left) and FEM data (right) for sample structure with staggered cells, with images showing results at 18% elongation in the vertical direction.

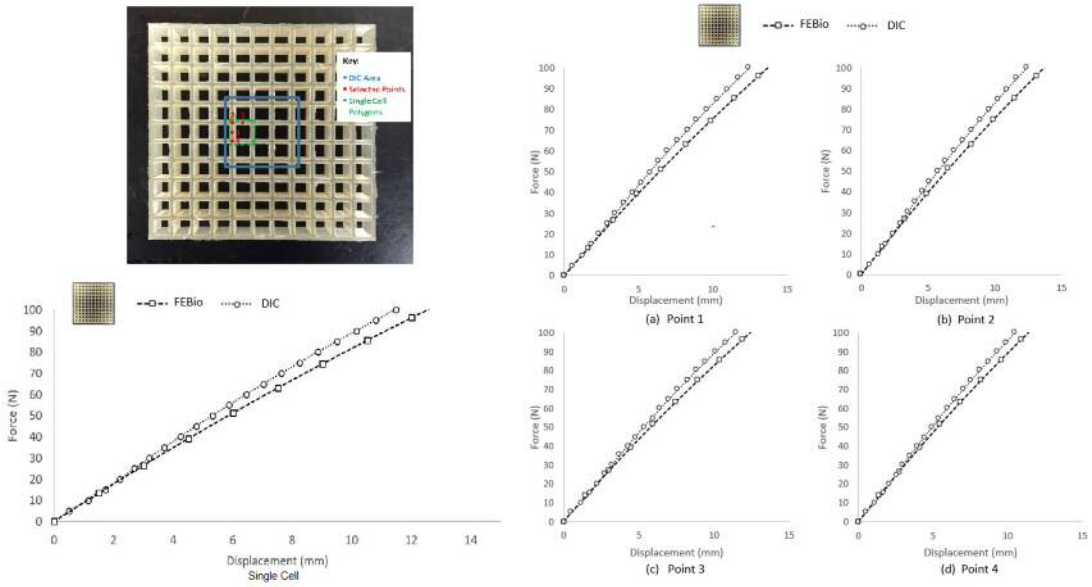

Figure A4: Comparison between DIC and FEM results for sample structure with stacked cells subject to vertical tensile force at the top horizontal boundary, showing the local displacements at cell and point levels.

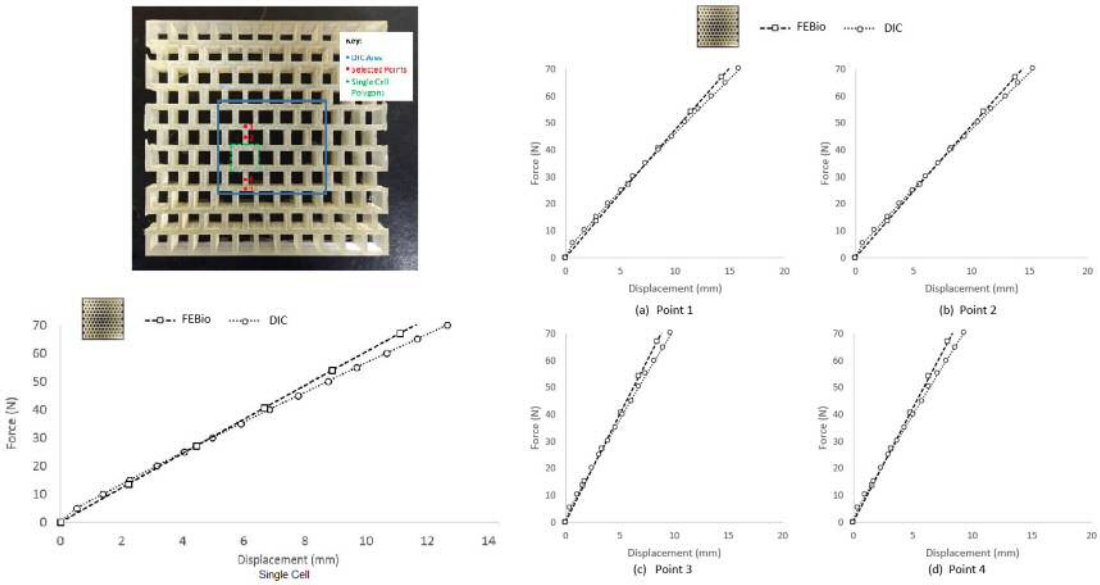

Figure A5: Comparison between DIC and FEM results for sample structure with staggered cells subject to vertical tensile force at the top horizontal boundary, showing the local displacements at cell and point levels.

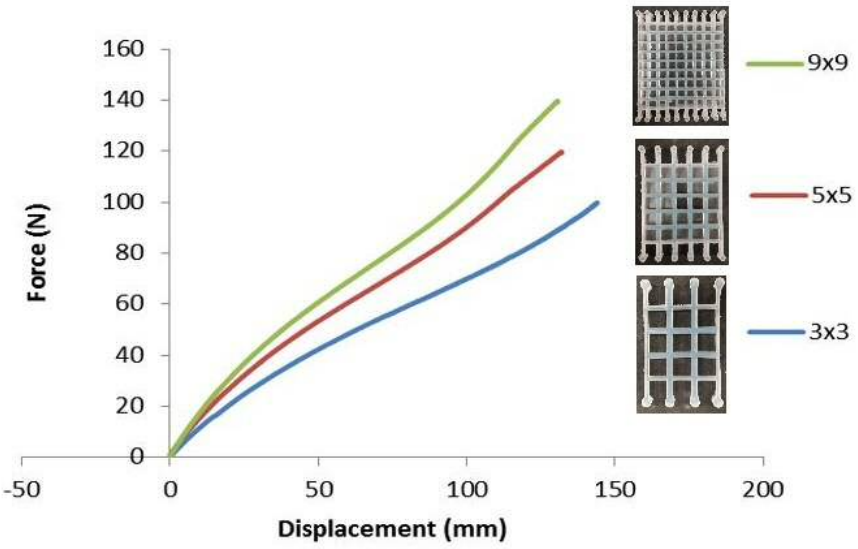

Figure A6: Experimental results for model structures with stacked cells under axial tension showing increase in nonlinear stiffening when the material volume and the ratio between the width and the length of the cell walls are fixed and the number of cells increases.

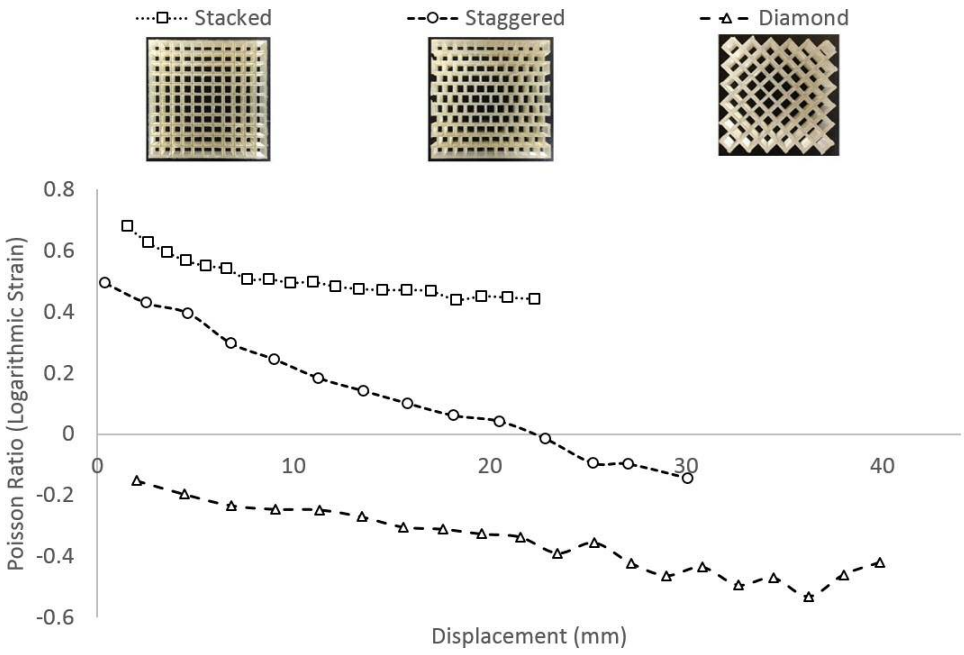

Figure A7: Experimental results for model structures under axial tension showing the decreases in the nonlinear Poisson's ratios for model structures with stacked, staggered, and diamond cells.

Bibliography

[1] Alexander RMcN, Bennett MB, Ker RF. 1986. Mechanical properties and function of the paw pads of some mammals, Journal of Zoology London A 209, 405-419.

[2] Allaire G. 2002. Shape Optimization by the Homogenization Method, Springer, Berlin.

[3] Ashby M. 2013. Designing architectured materials, Scripta Materialia 68, 4-7.

[4] Babuska I. 1974. Solution of problem with interface and singularities, in Mathematical Aspects of Finite Elements in Partial Differential Equations (de Boor C ed.), Academic Press, New York, 213-277.

[5] Baker M, Ericksen JL. 1954. Inequalities restricting the form of stress-deformation relations for isotropic elastic solids and Reiner-Rivlin fluids, Journal of the Washington Academy of Sciences 44, 24-27.

[6] Ball JM. 1977. Convexity conditions and existence theorems in non-linear elasticity, Archive for Rational Mechanics and Analysis 63, 337-403.

[7] Barett AH, Cardello AV, Lesher LL, Taub IA. 1994. Cellularity, mechanical failure, and textural perception of corn meal extrudates, Journal of Texture Studies 25, 77-95.

[8] Baskin TI, Jensen OE. 2013. On the role of stress anisotropy in the growth of stems, Journal of Experimental Botany, doi: 10.1093/jxb/ert176.

[9] Beatty MF. 2001. Seven lectures in finite elasticity, in Topics in Finite Elasticity (Hayes M, Saccomandi G eds.), Springer, Wien, 31-93.

[10] Beatty MF, Stalnaker DO. 1986. The Poisson function of finite elasticity, Journal of Applied Mathematics 53.

[11] Belytschko T, Liu W, Moran B. 2001. Nonlinear Finite Elements for Continua and Structures, Wiley, New York.

[12] Bennett MB, Ker RF. 1990. The mechanical properties of the human subcalcaneal fat pad in compression, Journal of Anatomy 171, 131-138.

[13] Bhaskar, A. 2009. The effective Poisson ratio of random cellular matter having bending dominated architecture, Europhysics Letters 87, 18004.

[14] Boccaccio A, Uva AE, Fiorentino M, Lamberti L, Monno G. 2016. A mechanobiology-based algorithm to optimize the microstructure geometry of bone tissue scaffolds, International Journal of Biological Sciences 12, 1-17.

[15] Bonet J, RD Wood RD. 2008. Nonlinear Continuum Mechanics for Finite Element Analysis, 2nd ed, Cambridge University Press, Cambridge, UK.

[16] Broedersz CP, MacKintosh FC. 2014. Modeling semiflexible polymer networks, Review of Modern Physics 86, 995-1036.

[17] Bruce DM. 2003. Mathematical modelling of the cellular mechanics of plants, Philosophical Transactions of the Royal Society of London B 358, 1437-1444.

[18] Brummell DA. 2006. Cell wall disassembly in ripening fruit, Functional Plant Biology 33, 103-119.

[19] Butler DL, Goldstein SA, Guilak F. 2000. Functional tissue engineering: the role of biomechanics, Journal of Biomechanical Engineering 122, 570-575.

[20] Chaplain MAJ. 1993. The strain energy function of an ideal plant cell wall, Journal of Theoretical Biology 163, 77-97.

[21] Chen P-O, McKittrick J, Meyers MA. 2012. Biological materials: functional adaptations and bioinspired designs, Progress in Materials Science 57, 1492-1704.

[22] Cioranescu D, Donato P. 1999. An Introduction to Homogenization, Oxford University Press, Oxford, UK.

[23] Clercq DD, Aerts P, Kunnen M. 1994. The mechanical characteristics of the human heel pad during foot strike in running: An in vivo cineradiographic study, Journal of Biomechanics 27, 1213-1222.

[24] Colby RH, Mattacks CA, Pond CM. 1993. The gross anatomy, cellular structure and fatty acid composition of adipose tissue in captive polar bears (*Ursus maritimus*), Zoo Biology 12, 267-275.

[25] Comley KSC, Fleck NA. 2012. The compressive response of porcine adipose tissue from low to high strain rate, International Journal of Impact Engineering 46, 1-10.

[26] De Belie N, Hallett IC, Harker FR,De Baerdemaeker J. 2000. Influence of ripening and turgor on the tensile properties of pears: a microscopic study of cellular and tissue changes, Journal of the American Society for Horticultural Science 125, 350-356.

[27] Deshpande VS, Ashby MF, Fleck NA. 2001. Foam topology bending versus stretching dominated architectures, Acta Materialia 49, 1035-1040.

[28] Deshpande VS, Fleck NA, Ashby MF. 2001. Effective properties of the octet-truss lattice material, Journal of the Mechanics and Physics of Solids 49, 1747-1769.

[29] Destrade M, Saccomandi G. 2010. On the rectilinear shear of compressible and incompressible elastic slabs, International Journal of Engineering Science 48, 1202-1211.

[30] De Pascalis R, Destrade M, Goriely A. 2010. Nonlinear correction to the Euler buckling formula for compressed cylinders with guided-guided end conditions, Journal of Elasticity 102, 191-200.

[31] Dinwoodie JM. 1981. Timber, its Nature and Behaviour, Van Nostrand Reinhold, New York.

[32] Discher DE, Janmey P, Wang Y. 2005. Tissue cells feel and respond to the stiffness of their substrate, Science 310, 1139-1143.

[33] Dunlop JWC, Fratzl P. 2013. Multilevel architectures in natural materials, Scripta Materialia 68, 8-12.

[34] Egan P, Ferguson S, Shea K. 2017. Design of hierarchical 3D printed scaffolds considering mechanical and biological factors for bone tissue engineering, Journal of Mechanical Design 139, 061401.

[35] Engelmayr Jr. GC, Papworth GD, Watkins SC, Mayer Jr. JE, Sacks MS. 2006. Guidance of engineered tissue collagen orientation by large-scale scaffold microstructures, Journal of Biomechanics 39, 1819-1831.

[36] Engler AJ, Sen S, Lee Sweeney H, Discher DE. 2006. Matrix elasticity directs stem cell lineage specification, Cell 126, 677-689.

[37] Ericksen JL. 1955. Deformation possible in every compressible isotropic perfectly elastic materials, Journal of Mathematics and Physics 34, 126-128.

[38] Evans SL, Holt CA. 2009. Measuring the mechanical properties of human skin in vivo using digital image correlation and finite element modelling, The Journal of Strain Analysis for Engineering Design 44, 337-345.

[39] Fisher DV. 1943. Mealiness and quality of Delicious apples as affected by growing conditions, maturity and storage techniques, Scientia Agricola 23, 569-588.

[40] Fleck NA, Deshpande VS, Ashby MF. 2010. Micro-architectured materials: past, present and future, Proceedings of the Royal Soci-

ety of London A: Mathematical, Physical and Engineering Sciences 466, 2495-2516.

[41] Fletcher R. 1991. Practical methods of optimization, 2nd ed, John Wiley & Sons, New York.

[42] Fosdick RA, Shield RT. 1963. Small bending of a circular bar superposed on finite extension or compression, Archive for Rational Mechanics and Analysis 12, 223-248.

[43] Fortes MA, Nogueira MT. 1989. The Poisson effect in cork, Materials Science and Engineering A 122, 227-232.

[44] Fournier M, Dlouhá J, Jaouen G, Almeras T. 2013. Integrative biomechanics for tree ecology: beyond wood density and strength, Journal of Experimental Botany, doi: 10.1093/jxb/ert279.

[45] Gariboldi MI, Best SM. 2015. Effect of ceramic scaffold architectural parameters on biological response, Frontiers in Bioengineering and Biotechnology, doi: 10.3389/fbioe.2015.00151.

[46] Gao Q, Pitt RE, Ruina A. 1990. A mechanics model of the compression of cells with finite contact area, Biorheology 27, 225-240.

[47] Geymonat G, Müller S, Triantafyllidis N. 1993. Homogenization of nonlinearly elastic materials, microscopic bifurcation and macroscopic loss of rank-one convexity, Archive for Rational Mechanics and Analysis 122, 231-290.

[48] Gibson LJ, Ashby MF. 1997. Cellular Solids: Structure and Properties, 2nd ed, Cambridge University Press, Cambridge, UK.

[49] Gibson LJ, Ashby MF, Harley BA. 2010. Cellular Materials in Nature and Medicine, Cambridge University Press, Cambridge, UK.

[50] Goriely A. 2017. The Mathematics and Mechanics of Biological Growth, Springer, New York.

[51] Green AE, Adkins JE. 1970. Large Elastic Deformations (and Non-linear Continuum Mechanics), 2nd ed, Oxford University Press, Oxford, UK.

[52] Green AE, Rivlin RS, Shield RT. 1952. General theory of small elastic deformations superposed on finite elastic deformations, Proceedings of the Royal Society A 211, 128-154.

[53] Green AE, Zerna W. 1968. Theoretical Elasticity, 2nd ed, Oxford Clarendon Press, Oxford, UK.

[54] Guilak F, Butler DL, Goldstein SA, Baaijens FPT. 2014. Biomechanics and mechanobiology in functional tissue scaffold, Journal of Biomechanics 47, 1933-1940.

[55] Harker FR, Hallett IC. 1992. Physiological changes associated with development of mealiness of apple fruit during cool storage, HortScience 27, 1291-1294.

[56] Harker FR, Redgwell RJ, Hallett IC, Murray SH. 1997. Texture of fresh fruit, Horticultural Reviews 20, 121-224.

[57] Holzapfel GA. 2000. Nonlinear Solid Mechanics: A Continuum Approach for Engineering, John Wiley & Sons, New York.

[58] Humphrey JD. 2003. Continuum biomechanics of soft biological tissues, Review Paper, Proceedings of the Royal Society A 459, 3-46.

[59] Hutchinson JW, Neale KW. 1981. Finite strain J_2 deformation theory, Proceeding of the IUTAM Symposium on Finite Elasticity, Martinus Nijhoff Publishers, Netherlands.

[60] Jahss MH, Kummer F, Michelson JD. 1992. Investigations into the fat pads of the sole of the foot: heel pressure studies, Foot Ankle 131, 227-232.

[61] Janmey PA, McCormick ME, Rammensee S, Leight JL, Georges PC, MacKintosh FC. 2006. Negative normal stress in semiflexible biopolymer gels, Nature Materials 6, 48-51.

[62] Jikov VV, Kozlov SM, Oleinik OA. 1994. Homogenization of Differential Operators and Integral Functionals, Springer, Berlin.

[63] Johnston JW, Hewett EW, Hertog MLATM. 2002. Postharvest softening of apple (*Malus domestica*) fruit: a review, New Zealand Journal of Crop and Horticultural Science 30, 145-160.

[64] Jung D, Gea HC. 2004. Topology optimization of nonlinear structures, Finite Elements in Analysis and Design 40, 1417-1427.

[65] Ker RF. 1999. The design of soft collageneous load-bearing tissues, The Journal of Experimental Biology 202, 3315-3324.

[66] Knychala J, Bouropoulos N, Catt CJ, Katsamenis OL, Please CP, Sengers BG. 2013. Pore geometry regulates early stage human bone marrow cell tissue formation and organisation, Annals of Biomedical Engineering 41, 917-930.

[67] Ledoux WR, Blevins JJ. 2007. The compressive material properties of the plantar soft tissue, Journal of Biomechanics 40, 2975-2981.

[68] Le Tallec P. 1994. Numerical methods for three-dimensional elasticity, in Handbook of Numerical Analysis, v. III (Ciarlet PG, Lions JL eds.), North-Holland, 465-624.

[69] Levin VA, Zubov LM, Zingerman KM. 2014. The torsion of a composite, nonlinear-elastic cylinder with an inclusion having initial large strains, International Journal of Solids and Structures 51, 1403-1409.

[70] Lewis R, Yoxall A, Marshall MB, Canty LA. 2008. Characterising pressure and bruising in apple fruit, Wear 264, 37-46.

[71] Liu Z, Chuah CSL, Scanlon MG. 2003. Compressive elastic modulus and its relationship to the structure of a hydrated starch foam, Acta Materialia 51, 365-371.

[72] Lopez-Pamies O, Castañeda PP. 2004. Second-order estimates for the macroscopic response and loss of ellipticity in porous rubbers at large deformations, Journal of Elasticity 76, 247-287.

[73] Maas SA, Ellis BJ, Ateshian GA, Weiss JA. 2012. FEBio: Finite Elements for Biomechanics, Journal of Biomechanical Engineering 134.

[74] Marzano S. 1983. An interpretation of Baker-Ericksen inequalities in uniaxial deformation and stress, Meccanica 18, 233-235.

[75] Maxwell JC. 1881. A Treatise on Electricity and Magnetism, 3rd ed, Clarendon Press, Oxford, UK.

[76] Meza LR, Das S, Greer JR. 2014. Strong, lightweight, and recoverable three-dimensional ceramic nanolattices, Science 345, 1322-1326.

[77] Meyers MA, Chen P-Y, Lin AY-M, Seki Y. 2008. Biological materials: structure and mechanical properties, Progress in Material Science 53, 1-206.

[78] Michailides PA, Triantafyllidis N, Shaw JA, Grummon DS. 2009. Superelasticity and stability of a shape memory alloy hexagonal honeycomb under in-plane compression, International Journal of Solids and Structures 46, 2724-2738.

[79] Mihai LA, Alayyash K, Goriely A. 2015. Paws, pads, and plants: the enhanced elasticity of cell-filled load-bearing structures, Proceedings of the Royal Society A 471, 20150107.

[80] Mihai LA, Alayyash K, Wyatt H. 2016. The optimal density of cellular solids in axial tension, Computer Methods in Biomechanics & Biomedical Engineering 20, 701-713.

[81] Mihai LA, Chin L, Janmey PA, Goriely A. 2015. A comparison of hyperelastic constitutive models applicable to brain and fat tissues, Journal of the Royal Society Interface 12, 20150486.

[82] Mihai LA, Goriely A. 2011. Positive or negative Poynting effect? The role of adscititious inequalities in hyperelastic materials, Proceedings of the Royal Society A 467, 3633-3646.

[83] Mihai LA, Goriely A. 2013. Numerical simulation of shear and the Poynting effects by the finite element method: an application

of the generalised empirical inequalities in non-linear elasticity, International Journal of Non-Linear Mechanics 49, 1-14.

[84] Mihai LA, Goriely A. 2014. Nonlinear Poisson effects in soft honeycombs, Proceedings of the Royal Society A 470, 20140363.

[85] Mihai LA, Goriely A. 2015. Finite deformation effects in cellular structures with hyperelastic cell walls, International Journal of Solids and Structures 53, 107-128.

[86] Mihai LA, Goriely A. 2017. How to characterize a nonlinear elastic material? A review on nonlinear constitutive parameters in isotropic finite elasticity, Proceedings of the Royal Society A 473, 20170607.

[87] Mihai LA, Safar A, Wyatt H. 2017. Debonding of cellular structures with fibre-reinforced cell walls under shear deformation, Journal of Engineering Mathematics, doi: 10.1007/s10665-016-9894-2.

[88] Mihai LA, Wyatt H, Goriely A. 2017. A microstructure-based hyperelastic model for open-cell solids, SIAM Journal on Applied Mathematics 77, 1397-1416.

[89] Mihai LA, Wyatt H, Goriely A. 2017. Microstructure-based hyperelastic models for closed-cell solids, Proceedings of the Royal Society A 473, 20170036.

[90] Miller-Young JE, Duncan NA, Baroud G. 2002. Material properties of the human calcaneal fat pad in compression: experiment and theory, Journal of Biomechanics 35, 1523-1531.

[91] Moon H, Truesdell C. 1974. Interpretation of adscititious inequalities through the effects pure shear stress produces upon an isotropic elastic solid, Archive for Rational Mechanics and Analysis 55, 1-17.

[92] Mooney M. 1940. A theory of large elastic deformation, Journal of Applied Physics 11, 582-592.

[93] Napier J. 1993. Hands, revised ed, Princeton University Press.

[94] Natali AN, Fontanella CG, Carniel EL. 2012. A numerical model for investigating the mechanics of calcaneal fat pad region, Journal of the Mechanical Behavior of Biomedical Materials 5, 216-223.

[95] Niklas KJ. 1992. Plant Biomechanics: An Engineering Approach to Plant Form and Function, University of Chicago Press, Chicago, IL.

[96] Oden JT. 2006. Finite Elements of Nonlinear Continua, 2nd ed, Dover, New York.

[97] Ogden RW. 1972. Large deformation isotropic elasticity e correlation of theory and experiment for incompressible Rubberlike solids, Proceedings of the Royal Society A 326, 565-584.

[98] Ogden RW. 1997. Non-Linear Elastic Deformations, 2nd ed, Dover, New York.

[99] Papanicolau G. Bensoussan A, Lions J-L. 1978. Asymptotic Analysis for Periodic Structures, North-Holland, Amsterdam.

[100] Papka SD, Kyriakides S. 1994. In-plane compressive response and crushing of honeycombs, Journal of Mechanics and Physics of Solids 42, 1499-1532.

[101] Papka SD, Kyriakides S. 1999. Biaxial crushing of honeycombs - Part I: experiments, International Journal of Solids and Structures 36, 4367-4396.

[102] Papka SD, Kyriakides S. 1999. In-plane biaxial crushing of honeycombs - Part II: analysis, International Journal of Solids and Structures 36, 4397-4423.

[103] Pauwels F. 1980. Biomechanics of the locomotor apparatus: contributions on the functional anatomy of the locomotor apparatus, Springer, Berlin.

[104] Peyton SR, Ghajar CM, Khatiwala CB, Putnam AJ. 2007. The emergence of ECM mechanics and cytoskeletal tension as important regulators of cell function, Cell Biochemistry and Biophysics 47, 300-320.

[105] Poisson S. 1822. Mémoire sur la Théorie du Magnétisme, Mémoires de l'Académie de Sciences de l'Institute de France 5.

[106] Pond CM, Mattacks CA, Colby RH. 1992. The anatomy, chemical composition, and metabolism of adipose tissue in wild polar bears (*Ursus maritimus*), Canadian Journal of Zoology 70, 326-341.

[107] Poynting JH. 1909. On pressure perpendicular to the shear-planes in finite pure shears, and on the lengthening of loaded wires when twisted, Proceedings of the Royal Society A 82, 546-559.

[108] Rajagopal KR, Wineman AS. 1987. New universal relations for nonlinear isotropic elastic materials, Journal of Elasticity 17, 75-83.

[109] Rich PM. 1986. Mechanical architecture of arborescent rain forest palms, Principes 30, 117-131.

[110] Rivlin RS. 1948. Large elastic deformations of isotropic materials. IV. Further developments of the general theory, Philosophical Transactions of the Royal Society of London. Series A, Mathematical and Physical Sciences 241, 379-397.

[111] Rivlin RS. 1953. The solution of problems in second order elasticity theory, Journal of Rational Mechanics and Analysis 2, 53-81.

[112] Rome K. 1998. Mechanical properties of the heel pad: current theory and review of the literature, The Foot 8, 179-185.

[113] Rumpler M, Woesz A, Dunlop JW, van Dongen JT, Fratzl P. 2008. The effect of geometry on three-dimensional tissue growth, Journal of thr Royal Society Interface 5, 1173-1180.

[114] Sakes A, Dodou D, Breedveld P. 2016. Buckling prevention strategies in nature as inspiration for improving percutaneous instruments: a review, Bioinspiration & Biomimetics 11, 021001.

[115] Scanlon MG. 2005. Biogenic cellular solids, in Soft Materials: Structure and Dynamics (Dutcher JR, Marangoni AG eds.), New York: Marcel Dekker, 321-349.

[116] Shan S, Kang SH, Wang P, Qu C, Shian S, Chen ER, Bertoldi K. 2014. Harnessing multiple folding mechanisms in soft periodic structures for tunable control of elastic waves, Advanced Functional Materials 24, 4935-4942.

[117] Shield RT. 1971. Deformations possible in every compressible, isotropic, perfectly elastic material, Journal of Elasticity 1, 91-92.

[118] Shih YRV, Tseng KF, Lai HY, Lin CH, Lee, OK. 2011. Matrix stiffness regulation of integrin-mediated mechanotransduction during osteogenic differentiation of human mesenchymal stem cells, Journal of Bone and Mineral Research 26, 730-738.

[119] Siboni MC, Castañeda PP. 2014. Fiber-constrained, dielectric-elastomer composites: finite-strain response and stability analysis, Journal of the Mechanics and Physics of Solids 68, 211-238.

[120] Silva MJ, Hayes WC, Gibson LJ. 1995. The effects of non-periodic microstructure on the elastic properties of two-dimensional cellular solids, International Journal of Mechanical Sciences 37, 1161-1177.

[121] Silva MJ, Hayes WC, Gibson LJ. 1995. The effects of non-periodic microstructure and defects on the compressive strength of two-dimensional cellular solids, International Journal of Mechanical Sciences 39, 549-563.

[122] Spencer AJM. 1971. Theory of invariants, in Continuum physics (Erigen AC ed.), vol 1. Academic Press, New York, 239-353.

[123] Stroh AN. 1962. Steady state problems in anisotropic elasticity, Journal of Mathematics and Physics 41, 77-103.

[124] Taylor MP, Wedel MJ. 2013. Why sauropods had long necks; and why giraffes have short necks, PeerJ 1, 1-41.

[125] Timoshenko SP. 1983. History of strength of materials, Dover, New York.

[126] Tsang, VL, Chen AA, Cho LM, Jadin KD, Sah RL, DeLong S, West JL, Bhatia SN. 2007. Fabrication of 3D hepatic tissues by

additive photopatterning of cellular hydrogels, The FASEB Journal 21, 790-801.

[127] Triantafyllidis N, Maker, BN. 1985. On the comparison between microscopic and macroscopic instability mechanisms in a class of fiber-reinforced composites, Journal of Applied Mechanics 52, 794800.

[128] Truesdell C, Noll W. 2004. The Non-Linear Field Theories of Mechanics, 3rd ed, Springer, New York.

[129] van der Sman RGM. 2015. Hyperelastic models for hydration of cellular tissue, Soft Matter 11, 7579-7591.

[130] van Schalkwyk OL, Skinner JD, Mitchell G. 2004. A comparison of the bone density and morphology of giraffe (*Giraffa camelopardalis*) and buffalo (*Syncerus caffer*) skeletons, Journal of Zoology: Proceedings of the Zoological Society of London 264, 307-315.

[131] Vogel S. 1998. Cat's Paws and Catapults, W.W. Norton and Company, New York, London.

[132] Wang P, Casadei F, Shan S, Weaver JC, Bertoldi K. 2014. Harnessing buckling to design tunable locally resonant acoustic metamaterials, Physical Review Letters 113, 014301.

[133] Wang D, Wu MS. 2014. Generalized shear of a soft rectangular block, Journal of the Mechanics and Physics of Solids 70, 297-313.

[134] Warner M, Thiel BL, Donald AM. 2000. The elasticity and failure of fluid-filled cellular solids: theory and experiment, Proceedings of the National Academy of Sciences USA 97, 1370-1375.

[135] Weaire D, Fortes MA. 1994. Stress and strain in liquid and solid foams, Advances in Physics 43, 685-738.

[136] Weissengruber GE, Egger GF, Hutchinson JR, Groenewald HB, Elsässer L, Famini D, Forstenpointner G. 2006. The structure of the cushions in the feet of African elephants (*Loxodonta africana*), Journal of Anatomy 206, 781-792.

[137] Wells PNT, Liang H-D. 2011. Medical ultrasound: imaging of soft tissue strain and elasticity, Journal of the Royal Society Interface, 20110054.

[138] Wieding J, Wolf A, Bader R. 2014. Numerical optimization of open-porous bone scaffold structures to match the elastic properties of human cortical bone, Journal of the Mechanical Behavior of Biomedical Materials 37, 56-68.

[139] Wilkes EW. 1955. On the stability of a circular tube under end trust, The Quarterly Journal of Mechanics and Applied Mathematics 9, 88-100.

[140] Winer JP, Oake S, Janmey PA. 2009. Non-linear elasticity of extracellular matrices enables contractile cells to communicate local position and orientation, PloS ONE 4, e6382.

[141] Woo TC, Shield RT. 1962. Fundamental solutions for small deformations superposed on finite biaxial extension of an elastic body, Archive for Rational Mechanics and Analysis 9, 196-224.

[142] Yeung T, Georges PC, Flanagan LA, Marg B, Ortiz M, Funaki M, Zahir N, Ming W, Weaver V, Janmey PA. 2005. Effects of

substrate stiffness on cell morphology, cytoskeletal structure, and adhesion, Cell Motility and the Cytoskeleton 60, 2434.

[143] Zdunek A, Koziol A, Cybulska J, Lekka M, Pieczywek PM. 2016. The stiffening of the cell walls observed during physiological softening of pears, Planta 243, 519-529.

[144] Zhang H, Landmann F, Zahreddine H, Rodriguez D, Koch M, Labouesse M. 2011. A tension-induced mechanotransduction pathway promotes epithelial morphogenesis, Nature 471, 99-103.

[145] Zhu HX, Melrose JR. 2003. A mechanics model for the compression of plant and vegetative tissues, Journal of Theoretical Biology 221, 89-101.